UCLA
UCLA Electronic Theses and Dissertations

Title

Improved Accuracy of Dynamic Susceptibility Contrast Magnetic Resonance Imaging Estimates of Relative Cerebral Blood Volume in Human Gliomas by Accounting for Bidirectional Contrast Agent Exchange

Permalink

https://escholarship.org/uc/item/43z64715

Author

Leu, Kevin

Publication Date

2017

Peer reviewed|Thesis/dissertation

eScholarship.org Powered by the California Digital Library
University of California

UNIVERSITY OF CALIFORNIA

Los Angeles

Improved Accuracy of Dynamic Susceptibility Contrast Magnetic Resonance Imaging Estimates of Relative Cerebral Blood Volume in Human Gliomas by Accounting for Bidirectional Contrast Agent Exchange

A dissertation submitted in partial fulfillment

of the requirements for the degree Doctor of Philosophy

in Bioengineering

by

Kevin Leu

2017

© Copyright by

Kevin Leu

2017

ABSTRACT OF THE DISSERTATION

Improved Accuracy of Dynamic Susceptibility Contrast Magnetic Resonance Imaging Estimates of Relative Cerebral Blood Volume in Human Gliomas by Accounting for Bidirectional Contrast Agent Exchange

by

Kevin Leu

Doctor of Philosophy in Bioengineering

University of California, Los Angeles, 2017

Professor Benjamin M. Ellingson, Co-Chair

Professor Daniel B. Ennis, Co-Chair

Magnetic resonance imaging (MRI) plays an integral role in the diagnosis and monitoring of gliomas. One means by which MRI has been used to assess treatment efficacy has been measuring the volumes of contrast-enhancing lesions on post-contrast T_1-weighted images. Clinically, an increase of the lesion volume by a certain percentage compared to a previous baseline scan warrants a change in treatment. However, this type of imaging has its limitations, as exemplified by false positive radiographic determination of tumor progression ("pseudoprogression") and false positive radiographic determination of treatment response ("pseudoresponse").

Given the vascular nature of gliomas, perfusion-weighted dynamic susceptibility contrast (DSC)-MRI has been studied in efforts to improve the detection, characterization, and monitoring of gliomas after treatment. However, applying DSC-MRI biomarkers is not necessarily straightforward. One of the biggest problems with the calculation of relative cerebral blood volume (rCBV) is that it is compromised by artifacts created by the extravasation of contrast agent from the vasculature. This can be a particular challenge in the neuro-oncology field since blood brain barrier disruption is a common feature of gliomas.

This work attempts to improve estimates of rCBV in gliomas by incorporating a two-compartment pharmacokinetic model into the indicator dilution theory, which we term the "bidirectional" leakage correction. In Chapter II, we use simulation methods to demonstrate improved accuracy gained by the bidirectional leakage correction, as compared to a current, popular leakage correction ("unidirectional" leakage correction). In Chapter III, we demonstrate that the bidirectional model-generated permeability curves have better correlation with DCE-MRI permeability curves than those generated by the unidirectional model. We also demonstrate that the rCBV is more similar for the bidirectional model between two separate pre-treatment scans from the same patient. In Chapter IV, we demonstrate that the change in bidirectional rCBV can stratify glioblastoma patients treated with bevacizumab according to long- or short-term survival. In all, the above works demonstrate that the new technique better combats leakage effects, thereby improving the clinical utility of rCBV for human gliomas.

The dissertation of Kevin Leu is approved.

Alex A. Bui

Timothy F. Cloughesy

Nader Pouratian

Harry V. Vinters

Benjamin M. Ellingson, Committee Co-Chair

Daniel B. Ennis, Committee Co-Chair

University of California, Los Angeles

2017

DEDICATION

In loving memory of my mother, Inwon Leu, whose life has inspired me to follow my heart with a pioneering spirit.

TABLE OF CONTENTS

ACKNOWLEDGMENTS

This dissertation could not have been completed without the incredible support of numerous individuals over the years. First, I would like to thank my parents, Inwon Leu and Dr. Yowyuh Leu, for encouraging and supporting my academic interests through this long journey. I also would like to thank the current and former members of the UCLA Brain Tumor Imaging Laboratory, Davis Woodworth, Dr. Robert Harris, Catalina Raymond Guzman, and Anh Tran, for their assistance and helpful discussion. I am also grateful to Dr. Jerrold Boxerman at Brown University for his guidance and advice on numerous projects and the MD/PhD career path.

Polly Kay and Saima Chaabane deserve special mention for managing the clinical aspects of our projects. I would also like to thank Sergio Godinez, Glen Nyborg, Francine Cobla, Kelly O'Connor, Nick Haid, and Karen Hernandez for their help in collecting patient data as well as Lauren Mutascio, Earline Clausell, Andrea Osuna, and Oscar Perez for their help with scheduling and administrative support.

I also owe my gratitude to the UCLA Medical Scientist Training Program for welcoming me into the program. I would especially like to thank Dr. Kelsey Martin and Dr. Carlos Portera-Cailliau for their mentorship as I navigate the physician-scientist route. I would also like to thank the members of the entering class of 2011 for their support in this challenging journey.

I would like to thank my committee members for their guidance and for challenging me to think like a physician-scientist. Finally, I would like to thank my advisor, Dr. Benjamin Ellingson, for his mentorship and commitment to my development as a scientist.

BIOGRAPHICAL SKETCH

2011 A.B. in Chemistry, Harvard College, Cambridge, MA

FELLOWSHIPS

2016-2017 UCLA Dissertation Year Fellowship

2016 John J. Pick Fellowship

2011- 2019 UCLA Medical Scientist Training Program

PUBLICATIONS

1. **Leu K**, Boxerman JL, and Ellingson BM. Effects of MRI Protocol Parameters, Preload Injection Dose, Fractionation Strategies, and Leakage Correction Algorithms on the Fidelity of Dynamic Susceptibility Contrast MRI Estimates of Relative Cerebral Blood Volume in Gliomas. *AJNR. Am J Neuroradiol.* 2016; In Press.
2. **Leu K**, Boxerman JL, Lai A, Nghiemphu PL, Pope WB, Cloughesy TF, and Ellingson BM. Bidirectional Contrast Agent Leakage Correction of DSC-MRI Improves Cerebral Blood Volume Estimation and Survival Prediction in Recurrent Glioblastoma Treated with Bevacizumab. *J Magn Reson Imaging*. 2016; 44:1229-1237.
3. **Leu K**, Boxerman JL, Cloughesy TF, Lai A, Nghiemphu PL, Liau LM, Pope WB, and Ellingson BM. Improved Leakage Correction for Single-Echo Dynamic Susceptibility Contrast (DSC) Perfusion MRI Estimates of Relative Cerebral Blood Volume (rCBV) in High-grade Gliomas by Accounting for Bidirectional Contrast Agent Exchange. *AJNR. Am J Neuroradiol.* 2016; 37: 1440-6.
4. **Leu K**, Enzmann DR, Woodworth DC, Harris RJ, Tran AN, Lai A, Nghiemphu PL, Pope WB, Cloughesy TF, Ellingson BM. Hypervascular Tumor Volume Estimated by Comparison to a Large-scale Cerebral Blood Volume Radiographic Atlas Predicts Survival in Recurrent Glioblastoma Treated with Bevacizumab. *Cancer Imaging.* 2014; 14:31.
5. **Leu K**, Pope WB, Cloughesy TF, Lai A, Nghiemphu PL, Chen W, Liau LM, and Ellingson BM. Imaging Biomarkers for Anti-Angiogenic Therapy in Malignant Gliomas. *CNS Oncology*. 2013; 2: 33-47.
6. Laiwalla AN, Kurth F, **Leu K**, Liou R, Pamplona J, Ooi YC, Salamon N, Ellingson BM. Evaluation of Encephaloduroarteriosynangiosis Efficacy Using Probabilistic Independent Component Analysis Applied to Dynamic Susceptibility Contrast Perfusion MRI. *AJNR. Am J Neuroradiol.* 2017; In Press.
7. Ellingson BM, Harris RJ, Woodworth DC, **Leu K**, Zaw O, Mason WP, Sahebjam S, Abrey LE, Aftab DT, Schwab GM, Hessel C, Lai A, Nghiemphu, PL, Pope WB,

Wen PY, and Cloughesy TF. Baseline Pretreatment Contrast Enhancing Tumor Volume Including Central Necrosis is a Prognostic Factor in Recurrent Glioblastoma: Evidence from Single- and Multicenter Trials. *Neuro Oncol*. 2017; 19: 89-98.

8. Chang W, Pope WB, Harris RJ, Hardy AJ, **Leu K**, Mody RR, Nghiemphu PL, Lai A, Cloughesy TF, and Ellingson BM. Diffusion MR Characteristics Following Concurrent Radiochemotherapy Predicts Progression and Overall Survival in Newly Diagnosed Glioblastoma. *Tomography*. 2015; 1:37-43.
9. Banerjee P, **Leu K**, Harris RJ, Cloughesy TF, Lai A, Nghiemphu PL, Pope WB, Bookheimer SY, and Ellingson BM. Association Between Lesion Location and Language Function in Adult Glioma Using Voxel-based Lesion-symptom Mapping. *Neuroimage Clin.* 2015; 9:617-24.
10. Ellingson BM, Hirata Y, Yogi A, Karavaeva E, **Leu K**, Woodworth DC, Harris RJ, Enzmann DR, Wu JY, Mathern GW, and Salamon N. Topographical Distribution of Epileptogenic Tubers in Patients with Tuberous Sclerosis Complex. *J Child Neurol.* 2016; 31:636-45.

ORAL PRESENTATIONS

1. **Leu K**, Boxerman JL, and Ellingson BM. Optimized Image Acquisition and Leakage Correction Post-Processing of Dynamic Susceptibility Contrast (DSC) MRI for Highest Accuracy of Relative Cerebral Blood Volume (rCBV) Quantification in Human Brain Tumors. 2016; *Radiological Sciences of North America (RSNA)*, Chicago, IL.
2. **Leu K**, Pope WB, Cloughesy TF, and Ellingson BM. Perfusion Spectrum Imaging (PSI) in Human Brain Tumors. 2016; *American Society of Neuroradiology (ASNR)*, Washington DC.
3. **Leu K**, Boxerman JL, Cloughesy TF, Lai A, Ngiemphu PL, Pope WB, and Ellingson BM. Tofts Model-Corrected Leakage Correction of Relative Cerebral Blood Volume (rCBV) Maps for Single-Echo Gradient Echo Dynamic Susceptibility Contrast (DSC)-MRI Acquisitions. 2015; *American Society of Neuroradiology (ASNR)*, Chicago, IL.
4. **Leu K**, Chen W, Czernin J, Cloughesy TF, Nghiemphu PL, Lai A, Pope WB, Phelps ME, and Ellingson BM. Spatial Correlation between ADC and ^{18}F-FDOPA PET in Diffuse Gliomas. 2013; *American Society of Neuroradiology (ASNR)*, San Diego, CA.

PATENTS

1. Ellingson BM, **Leu K**. Leakage Correction for DSC-Perfusion MRI by Accounting for Contrast Agent Exchange. Provisional U.S. Patent #61/824,864. August 30, 2015.
2. Ellingson BM, **Leu K**. Multi-Echo Spin-, Asymmetric Spin-, and Gradient-Echo Echo-Planar Imaging. Provisional U.S. Patent #62/211,852. August 30, 2015

Chapter I. Introduction

i. Gliomas and MRI

Of the more than 26,000 malignant brain tumors diagnosed in the United States each year, gliomas comprise approximately 80%[1]. The most common type of gliomas is glioblastomas, which are a devastating, biologically aggressive class of tumors that present several unique treatment challenges. Due to their heterogeneous and topographically diffuse nature, both within and across tumors, glioblastomas carry a poor prognosis of 14 months with the standard of care – maximal safe tumor resection, followed by radiotherapy with concurrent and adjuvant temozolomide[2-4].

One of the pathologic hallmarks of gliomas is angiogenesis, the formation of new blood vessels from existing ones[5]. Because glioma cells require that oxygen and nutrients continually be delivered, new vessels must be formed in order for the tumors to grow. One of the mechanisms by which angiogenesis occurs is the hypoxia inducible factor-1 (HIF-1) and the vascular endothelial growth factor (VEGF) pathways, which lead to the recruitment and proliferation of endothelial cells[6]. The end result of this aberrant pro-angiogenic signaling is a dense network of vessels that are immature, tortuous, and permeable[7]. Overall, increased VEGF expression predicts glioma aggressiveness and denotes poorer outcomes[8].

Currently, magnetic resonance imaging (MRI) is the mainstay for the diagnosis and therapeutic monitoring of gliomas. Conventionally, T_1-weighted anatomical MRI scans are used for the evaluation of gliomas, and an exogenous gadolinium-based contrast agent is used to better visualize the tumors on T_1-weighted images. If the

vasculature is permeable due to blood-brain barrier disruption, the contrast agent will leak into the extravascular space, causing a shortening of the T_1 of the tissue, which will appear bright on T_1-weighted images (**Fig 1.1**). It is the volume of this pathological contrast enhancement on T_1-weighted images, which has been used for decades as a surrogate for overall survival[9]. For example, with the Response Assessment of Neuro-oncology (RANO) critiera[9] established in 2010, a 25% or greater increase in the contrast-enhancing two-dimensional measurements from a baseline scan would indicate progression of the disease and therefore would warrant a change in therapy.

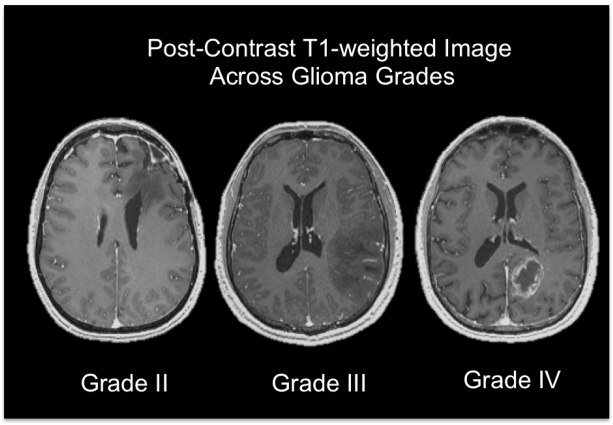

Fig. 1.1. Low grade gliomas (grade II) generally demonstrate hypo-intense T_1 lesions. The glioblastoma (grade IV) T_1-weighted image demonstrates a necrotic core with rim-like enhancement. The above example of the grade III is not hyperintense on post-contrast T_1-weighted imaging, though the dark tumor lesion is bigger than the grade II lesion. The volume of contrast enhancement is a conventional biomarker used to monitor tumor burden.

However, using the pathological contrast enhancing measurements on anatomical MRI has its limitations. For example, in "pseudoprogression", high-grade tumors may appear to enlarge on contrast enhancement without any accompanying clinical deterioration after treatment[10]. This phenomenon is attributed to an increase in the permeability of the vasculature, as opposed to actual tumor growth[11, 12]. On the other hand, in "pseudoresponse", the tumor rapidly shrinks on imaging after anti-angiogenic treatment[11]. However, overall survival increases due to these drugs are modest[13]. This phenomenon has been attributed to a decrease in vascular permeability, as opposed to a true tumor response event[14]. Both pseudoprogression and pseudoresponse demonstrate that contrast enhancement alone cannot be a sufficient biomarker for measuring therapeutic response. Furthermore, anatomical MRI gives limited information about the vascular characteristics of the tumor tissue. Therefore, other MRI modalities should be examined to determine if other imaging biomarkers can serve as surrogates for survival in determining treatment response for both present and future therapies. In particular, given that malignant gliomas are highly vascular, perfusion-weighted MRI is one advanced MRI modality that may prove particularly useful in assessing gliomas.

ii. Perfusion and the Indicator Dilution Theory

Perfusion is the passage of fluid through a circulatory system, e.g. the delivery of blood to tissue through a vascular network. A system with unknown volume, such as the blood vasculature, can be assessed by adding a known quantity of indicator, such as gadolinium[15], assuming certain fundamental properties. Namely, the system must have only one inlet and outlet for the fluid, flow and volume must be constant for every

measurement, the intravenous contrast agent must mix thoroughly in the fluid, and the contrast agent must leave the system only through the outlet. By monitoring the behavior of the indicator, we can compute blood volume, blood flow, and mean transit time[16, 17].

In order to describe the characteristics governing the unknown fluid system, we first begin by describing the behavior of the contrast agent. After an instantaneous injection of bolus, the incremental amount of contrast agent, Δm, leaving the system between times t and $t+\Delta t$ is the concentration of contrast agent, $C(t)$, multiplied by constant flow, F.

(Eq. 1.1) $$\Delta m = C(t) \cdot F \cdot \Delta t$$

As it is assumed that all contrast agent must eventually leave the vascular network, the total amount of contrast agent leaving the system is the sum of Δm over time:

(Eq. 1.2) $$m = F \int_0^\infty C(t) dt$$

Here, we define a function that describes the fraction of contrast agent leaving the system per unit time:

(Eq. 1.3) $$h(t) = \frac{F \cdot C(t)}{m}$$

Note that integrating the distribution function over all time would be a re-arrangement of the terms in Eq. 1.2 and is thus equal to unity.

To relate the contrast agent behavior to the volume of fluid in the system, we first consider all of the particles in the fluid to have a distribution of transit times. Transit times are the time that it takes to for a particle to travel from the beginning to the end of the system. The rate at which fluid particles leave the system is F, and the rate at which particles are leaving the system between t and $t+\Delta t$ is given by $F \cdot h(t) \cdot \Delta t$. At time t, the indicator particles that we can visualize have transit times between t and $t+\Delta t$. However,

the volume element of the fluid particles at time *t* is comprised of those particles that have transit times between *t* and *t+Δt* and entered the vascular network between *t* units before *0* and time *0*. That is, any fluid particle that entered between *t* units before *0* and time *0* will be in the system at the time that the indicator particles are detected. Thus, the volume element of fluid at time *t* is *t* units of fluid multiplied by $F \cdot h(t) \cdot \Delta t$:

(Eq. 1.4) $$\Delta V = t \cdot F \cdot h(t) \cdot \Delta t$$

Summing over all of the small volumes, ΔV, yields

(Eq. 1.5) $$V = F \int_0^\infty t \cdot h(t) dt$$

We can further define the mean circulation time as

(Eq. 1.6) $$\bar{t} = \int_0^\infty t \cdot h(t) dt$$

Thus, blood volume is equal to flow times mean circulation time, the fundamental equation of the indicator dilution theory:

(Eq. 1.7) $$V = F \cdot \bar{t}$$

In practice, a tissue voxel is comprised of not just the plasma (P), but also the intracellular (I) and extravascular, extracellular (E) space

(Eq. 1.8) $$f = \frac{v_p}{v_p + v_I + v_E}$$

The average concentration of contrast material is smaller than the intravascular concentration by that fraction f[18]:

(Eq. 1.9) $$c_t = f \cdot c_v$$

Per the assumptions of the indicator dilution theory, the total amount of contrast entering the system must be equal to the amount leaving; thus,

(Eq. 1.10) $$m = \int_0^\infty F \cdot C_\alpha(t) = \frac{1}{f} \int_0^\infty F \cdot C_t(t)$$

Rearranging the terms in Eq. 1.10, we obtain

(Eq. 1.11) $$f = \frac{\int_0^\infty C_t(t)dt}{\int_0^\infty C_\alpha(t)dt}$$

which is equivalent to the fractional vascular volume in that voxel. In perfusion imaging, the fractional vascular volume is referred to as the blood volume (BV):

(Eq. 1.12) $$BV = \frac{\int_0^\infty C_t(t)dt}{\int_0^\infty C_\alpha(t)dt}$$

iii. DSC-MRI and the Indicator Dilution Theory

In MRI, the behavior of an indicator like exogenous gadolinium contrast can be monitored over time to study the vascular network. This modality is called the dynamic susceptibility contrast (DSC)-MRI. In this technique, the first pass of the bolus of contrast agent is monitored through a series of T_2*-weighted (or T_2-weighted) MR images. In DSC-MRI, gadolinium acts as a "negative enhancing agent" in that it causes signal loss, as opposed to an increase in signal. This signal loss is modeled as being proportional to the concentration of contrast agent and can be used to calculate blood volume with the indicator dilution theory after a few post-processing steps from the raw DSC-MRI data.

The DSC-MRI signal intensity data is originally given in arbitrary units and must be converted into units that reflect the effects of the passage of contrast agent through the vasculature. The MRI signal information can be converted into a time curve that reflects the susceptibility difference caused by the passage of the contrast agent bolus at each voxel using the gradient echo signal equation. This susceptibility difference is assumed to be proportional to the contrast agent concentration:

(Eq. 1.13) $$\Delta R_2^*(t) = -\frac{1}{TE} \cdot \ln \frac{S(t)}{S_0} = r_2^* \cdot C(t),$$

where *TE* refers to the echo time, *S(t)* is the signal intensity from the DSC-MRI, S_0 represents the baseline signal intensity before the bolus of contrast agent, r_2* is the T_2* relaxivity of gadolinium, and *C(t)* is the concentration of contrast agent in the vasculature over time.

If the arterial input function (AIF) is known or estimated, the integration of contrast agent concentration in a voxel divided by the area under the curve for the AIF would then allow for the derivation of parametric maps of blood volume by plugging into Eq. 1.12:

(Eq. 1.14) $$BV_{DSC-MRI} = \frac{\int_0^\infty \Delta R_{2,t}^*(t)dt}{\int_0^\infty \Delta R_{2,AIF}^*(t)dt},$$

where the numerator represents the area under the curve of the relaxation-time curve in the voxel and the denominator represents the area under the curve for the AIF. In practice, however, AIF is difficult to estimate. Several manual and automatic approaches have been taken, usually to calculate a global AIF from the large arteries[19-22]. That is, an input function that is assumed to be the same throughout the tumor. However, the brain, in reality, has multiple, more local inputs from many smaller arteries[23]. Differences between the global AIF and the local input in reality would cause errors in blood volume calculations, and currently, no standards exist as to how to calculate either the global or local AIFs. One way to avoid the problems with AIF estimation has been computing the relative cerebral blood volume (rCBV)[24]. The term "relative" refers to the fact that the AIF is not being measured, as described in the following equation:

(Eq. 1.15) $$rCBV = \int_0^\infty \Delta R_{2,t}^*(t)dt$$

Often in neuro-oncology, the rCBV is computed relative to the contralateral normal appearing white matter. An example of an rCBV map is shown in **Fig 1.3**.

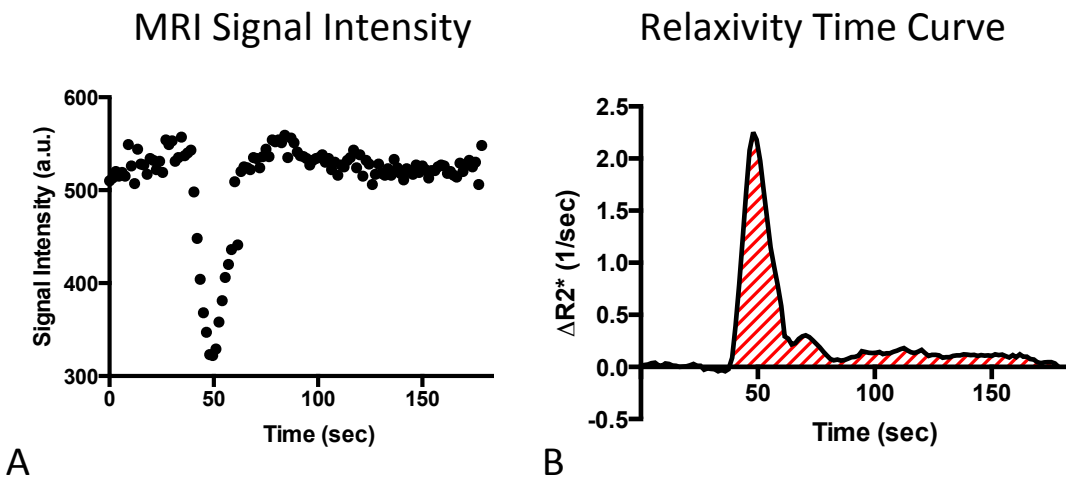

Fig. 1.2. (A) Arbitrary units of MRI signal intensity are first converted to (B) a relaxivity-time curve. The integration of the relaxivity-time curve yields relative cerebral blood volume.

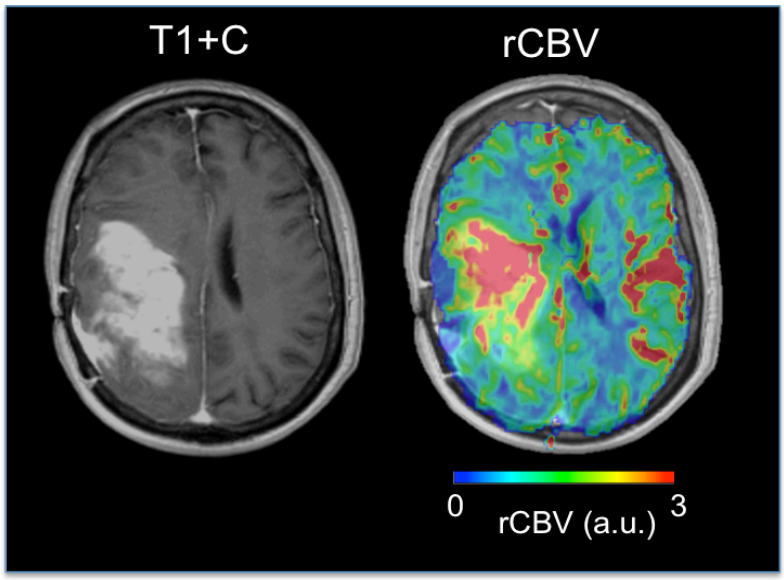

Fig. 1.3. Resultant rCBV map normalized to white matter. (Left) Anatomical T1-weighted post-contrast image demonstrating large glioma in the right hemisphere. (Right) The tumor has a much higher blood volume than the rest of the brain, with only the vasculature demonstrating similar levels of blood volume.

iv. Modeling DSC-MRI in the Presence of Contrast Agent Extravasation

However, an extra complication exists in gliomas in that the gadolinium-based contrast agents used will leak into the extravascular space. This is a violation of the assumption in the indicator dilution theory that the contrast agent must only leave the system through the outlet. By integrating the area under the curve in the presence of leakage, we would arrive at an inaccurate rCBV estimate. To model how the DSC-MRI signal arises in the event of gadolinium extravasation, we start with the gradient echo signal equation:

(Eq. 1.16) $$S(t) = \frac{S_0 \cdot (1 - e^{-\frac{TR}{T_1}}) \cdot e^{-\frac{TE}{T_2^*}}}{1 - e^{-\frac{TR}{T_1}} \cdot \cos(\alpha)} \cdot \sin(\alpha),$$

where S_0 is the proton density, TR is repetition time, TE is the echo time, α is the flip angle, T_1 is the tissue's longitudinal relaxation rate time constant, and T_2* is the tissue's transverse relaxation time constant in the presence of magnetic field inhomogeneities. In the presence of contrast agent, the tissue T_1 is shortened in the following manner:

(Eq. 1.17) $$R_1(t) = r_1 \cdot C_T(t) + R_{10}$$

where $R_1(t)$ is the reciprocal of the T_1 time constant over time, r_1 is the relaxivity of the contrast agent, C_T is the concentration of contrast agent in the tissue, and R_{10} is the reciprocal of the intrinsic tissue T_1. The T_2* effects are a result of the combination of T_2 shortening in the vasculature plus the differences in the concentration of gadolinium between compartments[25]:

(Eq. 1.18) $$R_2^*(t) = r_2(C_E(t) + C_P(t)) + a \cdot |C_E(t) - C_P(t)| + b \cdot |C_I(t) - C_P(t)| + c \cdot |C_I(t) - C_E(t)| + R_{20}^*,$$

where r_2 is the contrast agent's T_2 relaxivity, C is the concentration of contrast agent, E is the extravascular, extracellular compartment, P is the blood plasma compartment, I is the intracellular compartment, $a/b/c$ are the multipliers for the gradients induced between compartments, which are dependent on the size of the respective compartments as well as the vascular geometry, and R_{20}^* is the reciprocal of the intrinsic tissue T_2*. Substituting Eqs. 1.17 and 1.18 into Eq. 1.16 results in the following form for the gradient echo DSC-MRI signal intensity:

(Eq. 1.19) $$S(t) = \frac{S_0\left(1-e^{-TR\cdot(r_1\cdot C_T(t)+R_{10})}\right)}{1-e^{-TR\cdot(r_1\cdot C_T(t)+R_{10})\cdot\cos(\alpha)}}\cdot e^{-TE\cdot R_2^*(t)}\cdot\sin(\alpha),$$

In gliomas, the resulting relaxivity-time curve will be affected by either T_1-weighted or T_2*-weighted leakage effects, as exemplified by **Fig 1.4**. Integration of either the red or blue curves would lead to an inaccurate result compared to the ground truth in black.

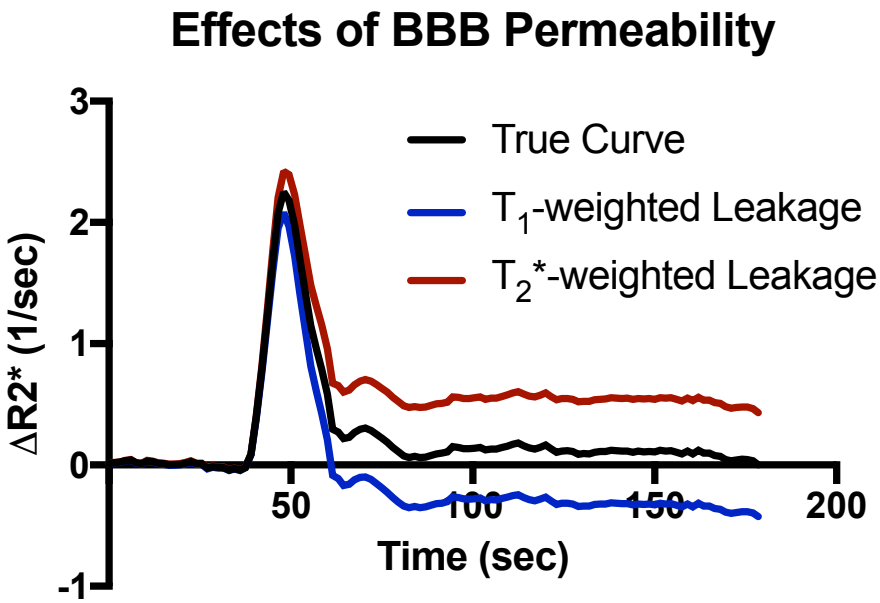

Fig. 1.4. Example of the effects of the contrast agent extravasation on the DSC-MRI curve. The ground truth is in black, which has a tail that returns approximately to zero. The blue line represents a DSC-MRI curve with T_1-weighted artifact due to leakage. Integration of this curve would lead to an underestimation of rCBV and can even lead to a negative rCBV in real tumor cases. The red line represents a DSC-MRI curve with T_2*-weighted artifact from leakage and would lead to an overestimation of rCBV.

v. Previous Efforts to Minimize the Effects of Contrast Agent Leakage

The biggest potential confound of relative cerebral blood volume calculation is the leakage of contrast agent, and a few strategies have been proposed to combat this. One commonly used method to mitigate those effects is preload, where an injection of contrast agent dosage is used prior to the one used for the DSC-MRI experiment. This shortens the tissue T_1, thereby decreasing the T_1 effects of leakage[26]. Another technique to mitigate T_1 effects has been to use flip angles of 35 degrees or lower[27, 28]. Nevertheless, with both of the aforementioned methods, there may still be T_2 and/or T_2* leakage effects, which can result in overestimations of the rCBV.

One popular method that can correct either T_1 or T_2/T_2*-weighted leakage effects is using a post-hoc model-based DSC-MRI leakage correction method proposed by Weisskoff and Boxerman[29-31]. This method uses the whole brain average (WBA) to correct rCBV for each voxel. The WBA not only serves as a reference function, but also an input function that allows for the computation of contrast agent extravasation into the tissue. The latter calculation makes the WBA similar in nature to the arterial input function (AIF). Using different combinations of the aforementioned techniques rCBV[32] has been used for grading gliomas[29, 33], predicting low-grade to high-grade transformation[34, 35], distinguishing recurrent tumor from pseudoprogression[36, 37], differentiating tumor regression from pseudoresponse[38], and assessing overall treatment response[39, 40].

vi. Proposed Bidirectional Leakage Correction Theory

As mentioned in previous sections, the exchange of contrast agent between the intravascular and the extravascular, extracellular space contaminates the desired DSC-

MRI signal, depending on pulse sequence parameters and underlying tumor biology.[25] A potentially limiting assumption of the previously mentioned post-hoc leakage correction approach is that contrast agent reflux from the interstitial space back to blood plasma is negligible within the time frame of DSC-MRI signal acquisition (~2 minutes). However, standard models quantifying contrast agent exchange between blood plasma and interstitium, such as that observed in the T_1-weighted perfusion-weighted sequence dynamic contrast enhanced (DCE)-MRI, use two-compartment pharmacokinetics to account for bidirectional transport of contrast agent. The reason that two compartments are used is because the contrast agent is assumed to only be present in the vasculature and the extravascular space. None is assumed to be present inside the cells, nor is any assumed to be metabolized or created by the system.

Here, we derive the equation for the bidirectional leakage correction. Following Eq. A6 of Boxerman *et al.*[31], the leakage-contaminated DSC-MRI relaxation rate-time curve, $\Delta\widehat{R}_2^*(t)$, equals intravascular contrast-driven transverse relaxation rate change, $\Delta R_2^*(t)$, plus $\Delta R_{2,E}^*(t)$, a tissue leakage term describing the simultaneous T_1 and T_2* relaxation effects resulting from gadolinium extravasation:

$$\text{(Eq. 1.20)} \quad \Delta\widehat{R}_2^*(t) = \Delta R_2^*(t) + \Delta R_{2,E}^*(t) = \Delta R_2^*(t) + \left[r_{2,E}^* - \frac{TR}{TE} \cdot \left(\frac{E_1}{1-E_1}\right) \cdot r_1\right] \cdot C_E(t)$$

where $E_1 = e^{-TR/T_{1o}}$, T_{10} is the pre-contrast tissue T_1, r_1 is the T_1 relaxivity of gadolinium, $C_E(t)$ is the concentration of gadolinium in the extravascular, extracellular space, and $r_{2,E}^*$ represents the T_2* relaxation effects of gadolinium extravasation, as described by Quarles[25] and Schmiedeskamp.[41] From the original Tofts model describing bidirectional contrast agent flux between the intravascular and extravascular compartments,[42]

(Eq. 1.21) $$C_E(t) = K^{trans} \cdot \left(C_p(t) * e^{-k_{ep}t}\right)$$

where K^{trans} and k_{ep} are the transfer coefficients for intra- to extravascular and extra- to intravascular contrast flux, respectively, and $C_p(t)$ is the plasma contrast concentration. $C_p(t)$ and $\Delta R_2^*(t)$ can be defined as scaled versions of the whole-brain average relaxation rate in non-enhancing voxels, $\Delta\bar{R}_2^*(t)$:[31]

(Eq. 1.22) $$C_p(t) = k \cdot \Delta\bar{R}_2^*(t)$$

(Eq 1.23) $$\Delta R_2^*(t) = K_1 \cdot \Delta\bar{R}_2^*(t)$$

Combining Eqs. 1.20–1.23 yields:

(Eq. 1.24) $$\Delta\hat{R}_2^*(t) = K_1 \cdot \Delta\bar{R}_2^*(t) - K_2 \int_0^t \Delta\bar{R}_2^*(\tau) \cdot e^{-k_{ep}(t-\tau)} d\tau$$

where

(Eq. 1.25) $$K_2 = \left[r_{2,E}^* - \frac{TR}{TE} \cdot \left(\frac{E_1}{1-E_1}\right) \cdot r_1\right] \cdot K^{trans} \cdot k.$$

K_1, K_2, and k_{ep} (units of sec^{-1}) are the free parameters of Eq. 1.25. In general, K_1 depends on CBV, vessel size, and other physiologic factors, while K_2/k_{ep} are related to vascular permeability. Substituting $k_{ep} = 0$, which occurs with no backflow of extravasated contrast agent, yields the original Weisskoff-Boxerman leakage correction algorithm, where K_1 and K_2 are solved by linear least squares fit to $\Delta\hat{R}_2^*(t)$.[31] For the *Bidir-model* correction method, a linear least squares fit to K_1, K_2, and k_{ep} can be employed using the methodology of Murase[43], as described by the following equation:

(Eq. 1.26) $$\Delta\hat{R}_2^*(t) = (K_2 + k_{ep} \cdot K_1) \int_0^{t_k} \Delta\bar{R}_2^*(\tau) d\tau - k_{ep} \cdot \int_0^{t_k} \Delta\hat{R}_2^*(\tau)\, d\tau + K_1 \cdot \Delta\bar{R}_2^*(t)$$

Integrating the corrected relaxation rate-time curve yields leakage-corrected rCBV:

(Eq. 1.27) $$rCBV_{Corr} = rCBV + K_2 \int_0^T \int_0^t \Delta\bar{R}_2^*(\tau) \cdot e^{-k_{ep}(t-\tau)} d\tau dt$$

The incorporation of the two-compartment pharmacokinetic model into the DSC-MRI theory results in an equation (Eq. 1.25) of the same form as the extended Tofts model[44], which could potentially unify the two perfusion-weighted modalities. The main difference in its application to the two perfusion-weighted MRI modalities is that in DCE-MRI, the extended Tofts model is used to calculate the surface area product (K_2), while K_1 is used to correct for the small T_2* contribution. Meanwhile for DSC-MRI, the main calculation involves K_1 while K_2 and k_{ep} are used as correction factors.

For Chapters II to IV of this work, we hypothesized that incorporating bidirectional contrast agent transport into the original DSC-MRI signal model improves rCBV estimates in brain tumors. We begin with a simulation, examine how the model fares in acquired data, and finally transition to clinical applications, testing the bidirectional model against the unidirectional model.

Chapter II. Estimating the Improvements in CBV Accuracy with the Bidirectional Leakage Correction through an MR Physics Simulation

Preface

Section ii of this chapter, "Estimation of CBV Accuracy at 3.0 Tesla", is based on the following publication:

Leu K, Boxerman JL, Ellingson BM. Effects of MRI Protocol Parameters, Preload Injection Dose, Fractionation Strategies, and Leakage Correction Algorithms on the Fidelity of Dynamic-Susceptibility Contrast MRI Estimates of Relative Cerebral Blood Volume in Gliomas. *AJNR. Am J Neuroradiol.* 2016; In Press.

i. Introduction

The leakage effects due to a disrupted blood brain barrier highly depend upon the protocol used for DSC-MRI signal acquisition[45]. To address these problems, certain strategies have been proposed for reducing the influence of contrast agent leakage, many of which focus on T_1-weighted artifact reduction. These include the use of low flip angles[32], dual-echo acquisitions[46-48], preload administration[49], and/or post-processing leakage-correction algorithms[31, 50-52]. These studies have employed a combination of these strategies to reduce extravasation-induced error of CBV estimates; however, these approaches have primarily been evaluated empirically.

In this section, we present a simulation that tests a wide range of feasible combinations of flip angles, echo times, repetition times, preload administrations, and leakage correction schemes, and the second that specifically compares the performances of the uncorrected CBV, unidirectional model, and bidirectional model. One reason for a

simulation is that the wide range of possible scan acquisition parameters would make testing in humans infeasible on a laboratory time scale. Furthermore, the lack of an FDA-approved contrast agent that will not leak into the extravascular, extracellular space makes calculating the ground truth in human gliomas difficult. On the other hand, the ability to generate a theoretical "ground truth" in simulation by setting the permeability parameter equal to zero allows us to examine the influence of scan acquisition protocols and leakage correction algorithms on CBV error.

ii. Estimation of CBV Accuracy at 3.0 Tesla

The goal of this first study is to systematically evaluate the effects of various leakage correction strategies on CBV estimation at 3.0 Tesla, the most powerful magnetic field that can be used in the clinical setting today. Here, we utilize simulated DSC-MRI data derived from convolution theory[17] and recent developments by Quarles *et al.*[25]. We hypothesized this approach could provide insights into the interaction of pulse sequence parameters, preload dosing, and leakage correction algorithms that are not readily determined experimentally.

Simulation Procedure

The following common DSC-MRI protocol variables were evaluated using simulations: pulse sequence parameters including flip angle, TE, and TR; preload dose and incubation time; truncation of the DSC-MRI dataset after first-pass to limit post-bolus leakage contamination; and post-processing leakage correction algorithms. Simulated DSC-MRI signal curves for brain tumors were generated via: 1) selection of pulse sequence parameters; 2) construction of the DSC-MRI relaxivity-time series

without leakage for "ground truth rCBV"; 3) construction of the leakage-affected intravascular and extravascular, extracellular space (EES) contrast agent concentration-time series based upon tumor characteristics; and 4) estimation of CBV using no leakage correction, unidirectional leakage correction (*Unidir*) as described by Boxerman *et al*.[31], or bidirectional leakage correction (*Bidir*) accounting for bidirectional contrast agent flux between the vasculature and EES[50, 51].

Simulated DSC-MRI Relaxation Rate-Time Curve

The simulated DSC-MRI relaxation rate-time curve is derived from the gradient echo signal equation, which has signal contributions from both T_1 and T_2. When the MRI signal intensities, which have arbitrary units, are converted to $\Delta R_2^*(t)$, in units of 1/s, these contributions are modeled for a single-shot gradient echo EPI acquisition as[25]:

(Eq. 2.1)

$$\Delta R_2^*(t) = r_{2,P}^* v_P C_p(t) + r_{2,E}^* v_E C_E(t) + K_P v_P v_E |C_P - C_E| - \frac{1}{TE} \cdot \left(\ln \frac{1-E_1 \cdot e^{-TR \cdot r_1 \cdot C_T(t)}}{1-E_1} - \ln \frac{1-\cos\alpha \cdot E_1 \cdot e^{-TR \cdot r_1 \cdot C_T(t)}}{1-\cos\alpha \cdot E_1} \right)$$

where α is the flip angle, $E_1 = e^{-TR/T_{10}}$, $E_2^* = e^{-TR/T_{20}^*}$, subscripts *E*, *I*, and *P* represent the extravascular, intracellular, and plasma compartments, respectively; *v* represents volume fraction; *K* represents "calibration susceptibility factors"; *C* represents contrast agent concentration; and r_1 and r_2 are the T_1 and T_2 gadolinium relaxivities, respectively. The first term, $r_{2,P}^* C_p(t)$, represents the T_2* contribution of the plasma concentration of contrast agent, the second term, $r_{2,E}^* C_E(t)$, represents the extravascular, extracellular contrast agent contribution to T_2*, $K_P v_P v_E |C_P - C_E|$, represents the T_2*-weighted

contribution owing to the difference in concentration of contrast agent between the vasculature and the EES, and $-\frac{1}{TE}\cdot\left(\ln\frac{1-E_1\cdot e^{-TR\cdot r_1\cdot C_T(t)}}{1-E_1}-\ln\frac{1-\cos\alpha\cdot E_1\cdot e^{-TR\cdot r_1\cdot C_T(t)}}{1-\cos\alpha\cdot E_1}\right)$, represents the T_1 contribution of contrast agent in both the plasma and EES.

Pulse Sequence Parameters

All combinations of the following DSC-MRI parameters were tested: Flip angle=35°, 60°, and 90°; TE=15, 25, 35, 45, and 55 ms; TR=1.0, 1.5, and 2.0 s; fractional preload + bolus dosage=¼ + ¾ (6 mM total, single dose), ½ + ½ (6 mM total, single dose), and 1 + 1 (12 mM total, double dose), where a different value of peak AIF concentration would simply scale all relaxivity-time curves proportionally.

Construction of Blood Plasma and EES Concentration

A generic AIF, which models the input of contrast agent into the tissue vasculature, was generated using the following gamma-variate-like approximation:

(Eq. 2.2) $$C_\alpha(t) = A\left(t/t_p^2\right)e^{-t/t_p} + B(-e^{-t/t_p}),$$

where A=200 mM·s, B=1.75 mM, and t_p=2 s (from[53]) and the peak concentration was 6.0 mM for the full dose and scaled appropriately for the preload dosages and post-preload bolus injections. For preload simulations, the *composite* AIF was constructed as the superposition of the preload injection AIF and the bolus AIF delayed by the specified incubation time.

The blood plasma contrast agent concentration was computed by convolving the AIF with an exponential residue function, where the residue function describes the tracer retention, the convolution is used to describe the AIF as a series of narrow, instantaneous

boluses of contrast agent, and the CBF factor accounts for the proportionality of the concentration in the vasculature to the delivered blood[17]:

(Eq. 2.3) $$C_p(t) = \frac{\rho}{k_H} \cdot CBF \cdot \int_0^t C_\alpha(\tau) \cdot e^{-\frac{t-\tau}{MTT}} d\tau,$$

where ρ is the density of brain tissue (1.04 g/mL), k_H is the hematocrit difference between capillaries and large vessels (0.73)[41], and MTT is the mean transit time.

The EES contrast agent concentration was computed using a two-compartment pharmacokinetic model as follows:

(Eq. 2.4) $$C_E(t) = K^{trans} \cdot \int_0^t C_\alpha(\tau) \cdot e^{-\left(\frac{K^{trans}}{v_e}\right)\cdot(t-\tau)} d\tau,$$

where K^{trans} describes the efflux rate of contrast agent from the vaculature, often equated with permeability, and K^{trans}/v_e describes the rate of contrast agent influx back into the vasculature.

The relaxivity-time curves were obtained from Eq. 2.1. For each relaxivity-time curve, *S(0)* was computed as the median of the first 30 s "baseline" signal.

Tissue, Contrast Agent, and Noise Characteristics

Specific tumor characteristics were estimated based on previous data from Schmiedeskamp *et al.*[41] including *CBV*=5 mL/100g, *CBF*=60 mL/100 g/min, and T_{20}*=0.05 s. The blood volume fraction, v_p, was set equal to $\rho/k_H \cdot CBV$. Relaxivity values for gadolinium (Gadavist®; Bayer AG, Leverkusen, Germany) were assumed to be r_1=3.6 $mM^{-1}s^{-1}$ [54], $r_{2,P}$*=87 $mM^{-1}s^{-1}$ [55], and $r_{2,E}$*=30 $mM^{-1}s^{-1}$ [47]. Monte Carlo simulations were performed using the following values: K^{trans}=0.214 ± 0.04 min^{-1} (range: 0.114 – 0.318), v_e=0.722 ± 0.17 (range: 0.259 - 0.985), T_{10}=1.59 ± 0.40 s (range: 0.84 – 2.87), $r_{2,P}$*=87.0 ± 17.4 $mM^{-1}s^{-1}$ (range: 42.4 – 132), and $r_{2,E}$*=30 ± 6 $mM^{-1}s^{-1}$ (range: 14.4 –

45.5). v_e was limited to a maximum of 1 and T_{10} was limited to a minimum of white matter (832 ms)[56].

K^{trans} and v_e were chosen by using the average values and standard deviations from Zhang *et al.*[57]. T_{10} was estimated from variable flip angle mapping from 25 glioblastomas (five pre-contrast T_1 flip angle maps were acquired for each patient (2°, 5°, 10°, 15°, 30°) and fitted using a Levenberg-Marquardt non-linear approach to the gradient-echo signal equation. The variance for $r_{2,P}$* and $r_{2,E}$* are, to the best of our knowledge, not well-defined in the literature and were chosen to be 20% to approximately match the standard deviations of the other parameters. K_p, the susceptibility calibration factor, was chosen to generate a 40% peak signal drop in gray matter, for which *CBF*=60 mL/100 g/min and *CBV*=4 mL/100g were chosen[58]. The whole brain average was selected as the average of 1,000 white matter voxels (including noise), with *CBF*=25 mL/100 g/min and *CBV*=2 mL/100 g.

CNR was first measured in a sample of 25 human glioblastomas (flip angle of 35°, TE=32 ms, and TR=1.8 s), which had a CNR of 40.5. To model noise added by TE and TR used, the CNR was scaled by $C \cdot \frac{\sin(\alpha)\cdot e^{-T\square/T_2^*}\left(1-e^{-TR/T_1}\right)}{\sin(35°)\cdot e^{-0.032/T_2^*}\left(1-e^{-1.8/T_1}\right)}$, where the numerator incorporates the new protocol's dose (C), TE, TR, and flip angle and the denominator scales the CNR according to the parameters used in acquiring the human data.

The CNR, which is defined with the following equation, was used to calculate standard deviation[22, 59]:

(Eq. 2.5) $$CNR = \frac{\Delta R_{2,max}^*}{\sigma},$$

where $\Delta R_{2,max}^{*}$ is the maximum value of ΔR_2^* and σ is the standard deviation of the Gaussian noise added to each time point. Gaussian noise was added with mean 0 and standard deviation σ.

Leakage Correction Algorithms

Uncorrected CBV was computed by integrating $\Delta R_2^*(t)$, while leakage-corrected CBV was obtained using either *Unidir*[31] or *Bidir*[50, 51] leakage correction algorithms. The "ground truth" ($\Delta R_2^*(t)_{gt}$) estimate of CBV was calculated under conditions of no noise with K^{trans}=0. Percentage error from ground truth was calculated for uncorrected and leakage corrected CBV estimates with added noise.

Effects of Preload Incubation Time and Truncation of the DSC Time Series

To estimate the effects of preload incubation time, we compared estimates of CBV with delays of 5-10 minutes between preload and bolus injection. To estimate the effects of truncating $\Delta R_2^*(t)$ on CBV estimates, we compared CBV estimates using the first 0.5, 1.0, 1.5, or 2.0 minutes of the post-baseline $\Delta R_2^*(t)$ as well as the entire 2.5 minute data.

Monte-Carlo Simulations to Estimate CBV Confidence Intervals

For each set of pulse sequence parameters, Gaussian noise was added to each time point with normal distribution (zero mean, standard deviation equal to maximum signal scaled by CNR), and tumor characteristics were generated according to the normal distributions described previously. A Monte Carlo simulation was conducted using 250 randomly chosen tumors, with random noise, for each set of pulse sequence parameters.

Percentage error was calculated using the computed CBV and the "ground truth" CBV. The 95% confidence intervals of percentage error were subsequently generated for the uncorrected CBV and each of the leakage correction algorithms and are shown in each of the figures. For **Fig. 2.1-2.6**, one particular protocol (60° flip angle, TE=35 ms, TR=1.0s, ¼ preload dose + ¾ DSC-MRI, waiting time=5 min) was chosen as the template based on ASFNR recommendations[60], with variations to only one of the parameters shown for each sub-figure. For **Fig. 2.7-2.8**, all combinations of flip angle, TR, TE, and preload dosage were evaluated. For all figures, integration of the relaxivity-time curve was performed from the injection time point to the end (2.5 min), unless otherwise noted.

DSC-MRI Scan Acquisition Protocol and Leakage Correction Simulation Results

Without preload, there is reduced T_1-weighting and increased T_2*-weighting with smaller flip angles as manifested by higher ΔR_2*(t), best seen in the "tail" (**Fig 2.1A**). Preload administration increases T_2*-weighting of the signal (**Fig 2.1B**). In this case, without preload, the 35° relaxivity-time curve is closest to "ground truth" (ΔR_2*$(t)_{gt}$), while the 60° and 35° curves are equally close to the truth curve after preload (¼ dose + ¾ dose DSC-MRI). Based on the formula used for CNR, the 35° flip angle also yields the most noise, as exemplified in the preload DSC-MRI curve. For both non-preload and preload administration, *Unidir*-corrected ΔR_2*(t) varied greater from ΔR_2*$(t)_{gt}$ across all tested flip angles as compared to *Bidir*-corrected ΔR_2*(t), particularly right after the first pass of the bolus (**Fig 2.1C-F**). **Fig 2.2A-B** illustrates the percentage errors for uncorrected, *Unidir*, and *Bidir* CBV estimates, as compared to ΔR_2*$(t)_{gt}$, for different flip angles. With this particular combination of TR/TE/preload dosage, the 35° flip angle has

the lowest error. Furthermore, error after both *Unidir* and *Bidir* leakage corrections tracked with error in the uncorrected CBV, i.e., the lower error in uncorrected CBV corresponded with lower error after leakage correction. For all tested flip angles, uncorrected CBV estimates have the highest error, followed by the *Unidir* and then the *Bidir* estimates.

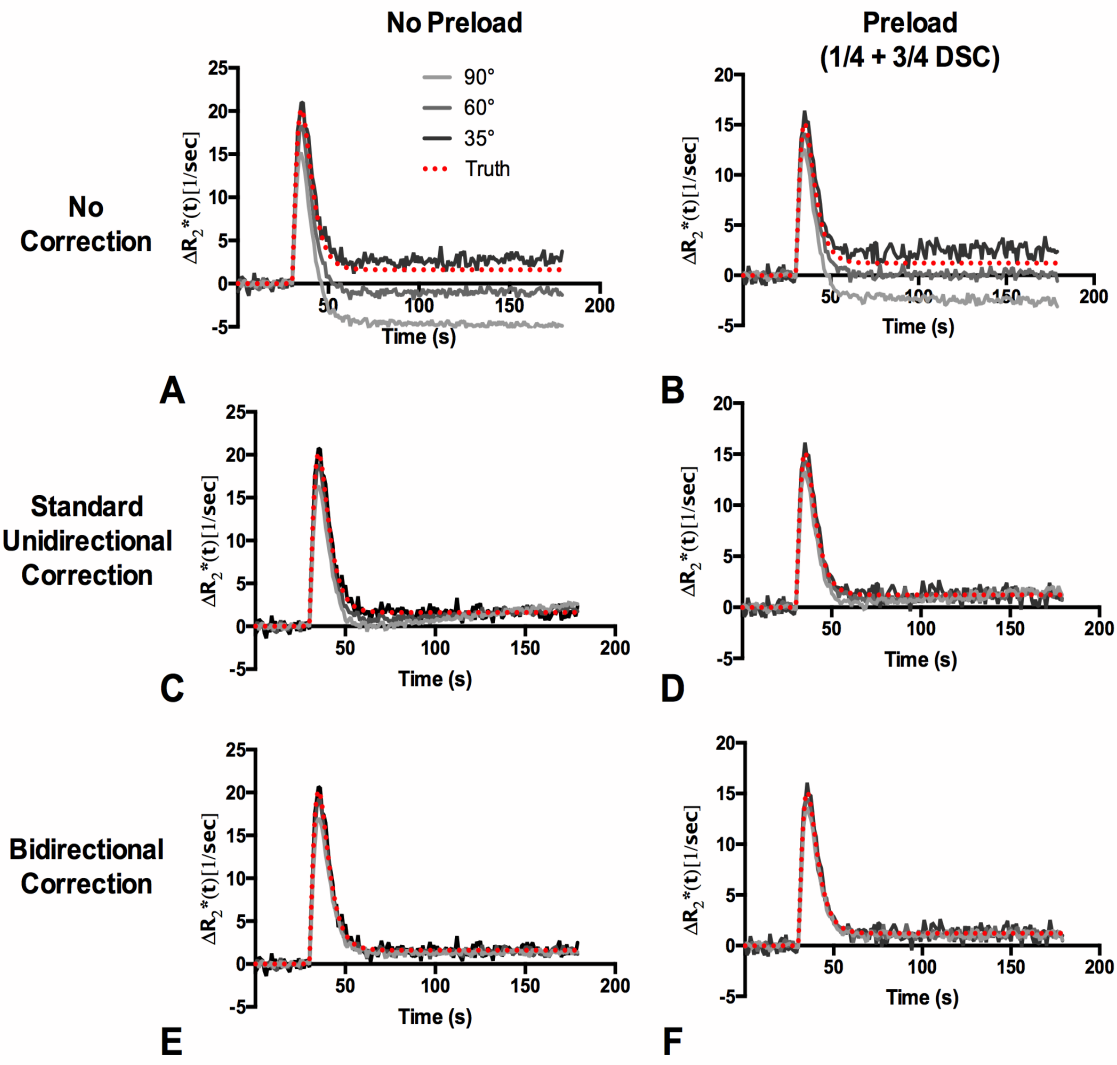

Fig. 2.1. Effect of flip angle on $\Delta R_2^*(t)$ (TE=35 ms/TR=1.0 s). A) $\Delta R_2^*(t)$ generated using different flip angles with noise along with $\Delta R_2^*(t)_{gt}$. B) $\Delta R_2^*(t)$ using ¼ dose of preload and ¾ dose for DSC-MRI bolus, which increases T_2^*-weighting for all flip angles. C) Corrected $\Delta R_2^*(t)$ using *Unidir* without preload. D) Corrected $\Delta R_2^*(t)$ using *Unidir* after preload. E) Corrected $\Delta R_2^*(t)$ using *Bidir* without preload. F) Corrected $\Delta R_2^*(t)$ using *Bidir* after preload. *Unidir*=unidirectional leakage correction algorithm. *Bidir*=bidirectional leakage correction algorithm.

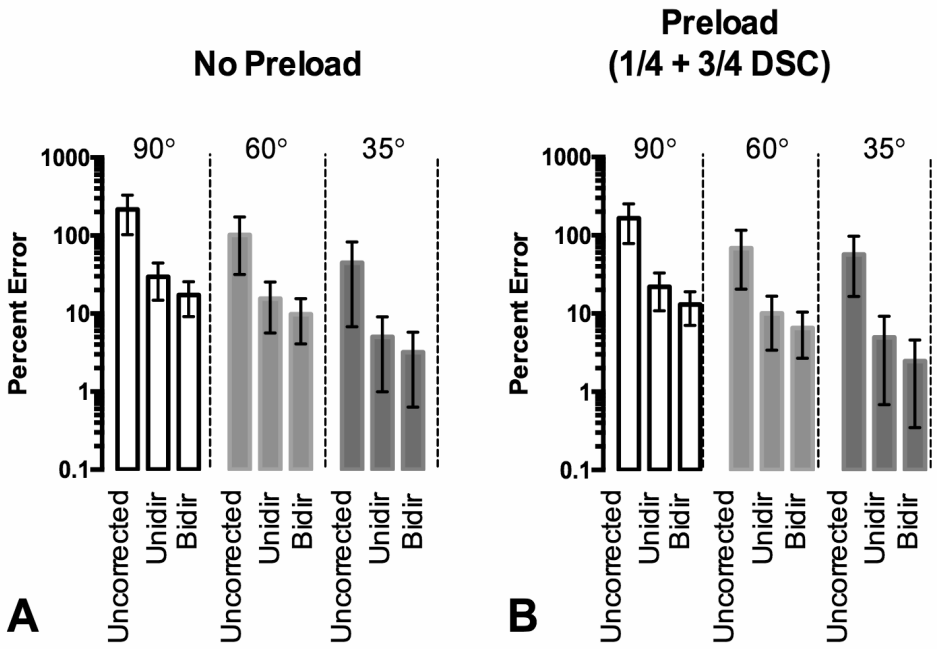

Fig. 2.2. Effect of flip angle on recovery of CBV (TE=35 ms/TR=1.0 s). A) Percentage error (with 95% CI) of the estimated CBV for different flip angles and leakage correction strategies, without use of preload, compared to "ground truth" CBV. B) Percentage error (with 95% CI) of the estimated CBV for different flip angles and leakage correction strategies, with use of ¼ dose preload, compared to "ground truth" CBV. *Unidir*=unidirectional leakage correction algorithm. *Bidir*=bidirectional leakage correction algorithm.

Results indicate longer TEs increase the T_2*-weighting of ΔR_2*(t) (**2.3A-B; 2.4A-B** 60° flip angle, TR=1.0 s). Without preload (**Fig 2.4A**), TE=55 ms yielded the most accurate ΔR2*(t) for all three correction strategies using all leakage correction strategies. With ¼ dose preload (**Fig 2.4B**), TE=45-55 ms performed more similarly, though the 55 ms performed slightly better. Post-hoc leakage correction error tracked with uncorrected error in these examples. Results also suggest increased T_2*-weighting (or decreased T_1-weighting) with longer TR (**Fig 2.3C-D**). Independent of preload, TR ≥ 1.5 s yielded ΔR_2*(t) with less error compared with ΔR_2*$(t)_{gt}$ for 60° flip (**Fig 2.4C-D**) for the chosen flip angle, TE, and preload dosage. In general, CBV errors using the three methods were linearly correlated.

Preload primarily increases T_2*-weighting and reduces T_1-weighting in ΔR2*(t) (**Fig 2.5A**; 60° flip angle, TE=35 ms, TR=1.5 s). For these parameters, 1 preload + 1 bolus dosing yielded higher ΔR_2*(t) fidelity compared to "ground truth" ΔR_2*(t) than the ¼ + ¾ and ½ + ½ dosing schemes (**Fig 2.6A**). Even though the ½ + ½ and 1 + 1 dosing schemes had approximately the same uncorrected CBV percent error, the post-hoc leakage correction algorithms benefited from the higher CNR that the full DSC-MRI dose provides. Results also suggest that preload does not act by decreasing the concentration-dependent rate of contrast agent efflux, but rather by decreasing baseline tissue T_1 prior to bolus injection, as well as increasing T_2*-weighting, as evidenced by identical wash-in rates and concentration-dependent reductions in baseline T_1 (**Fig 2.5B,C**).

Using incubation times of 5–10 minutes, the change in CBV error is virtually similar, with a slight, gradual decrease in error from 5 min to 10 min (**Fig 2.6B)**. Next, because CBV is computed from the integration of ΔR_2*(t), one strategy for mitigating leakage

effects is truncating ΔR_2*(t) after the first pass. As expected, the fewer data points used for computing CBV, the lower the percent error for uncorrected CBV. For *Unidir* CBV, mean percent error is lowest when 30 s is used and gradually increases over time. For *Bidir* CBV, percentage error was approximately the same for all cutoff times (**Fig. 2.6C**).

Overall, the protocol with the lowest overall mean percentage error utilized a 60° flip angle, TE/TR=35/1000 ms with 1 dose preload, using the bidirectional correction; however, there were multiple protocols whose 95% CIs overlapped (**Table 2.1**), suggesting there are several strategies that could be used to get similar CBV estimates. In general, the best performing strategies (dark red areas in **Fig 2.7**) were those that balanced both T_1- and T_2*-weighting secondary to contrast agent extravasation, with mean uncorrected CBV error < 70% for all of the "optimal" strategies with 1 total dose of contrast and < 80% for those with 2 total doses of contrast agent, as opposed to much larger error for other protocols. Standard deviation of the percent errors are included in **Fig. 2.8.** Preload did not necessarily depress percent error, as evidenced by the 35° flip angle, in which higher preload dosages could "overshoot" the "ground truth". The acquisition strategies with lowest mean error in this simulation (flip angle/TE/TR) for each preload dosing were the following: 1) with no preload and full dose for DSC-MRI: 35°/35 ms/1.5 s, 2) with ¼ dose preload and ¾ dose bolus: 35°/25 ms/1.5 s, 3) with ½ dose preload and ½ dose bolus: 60°/35 ms/2.0 s, and 4) with 1 dose preload and 1 dose bolus: 60°/35 ms/1.0 s. The 90° flip angle only appeared as an optimal strategy with 1 dose preload and 1 dose bolus.

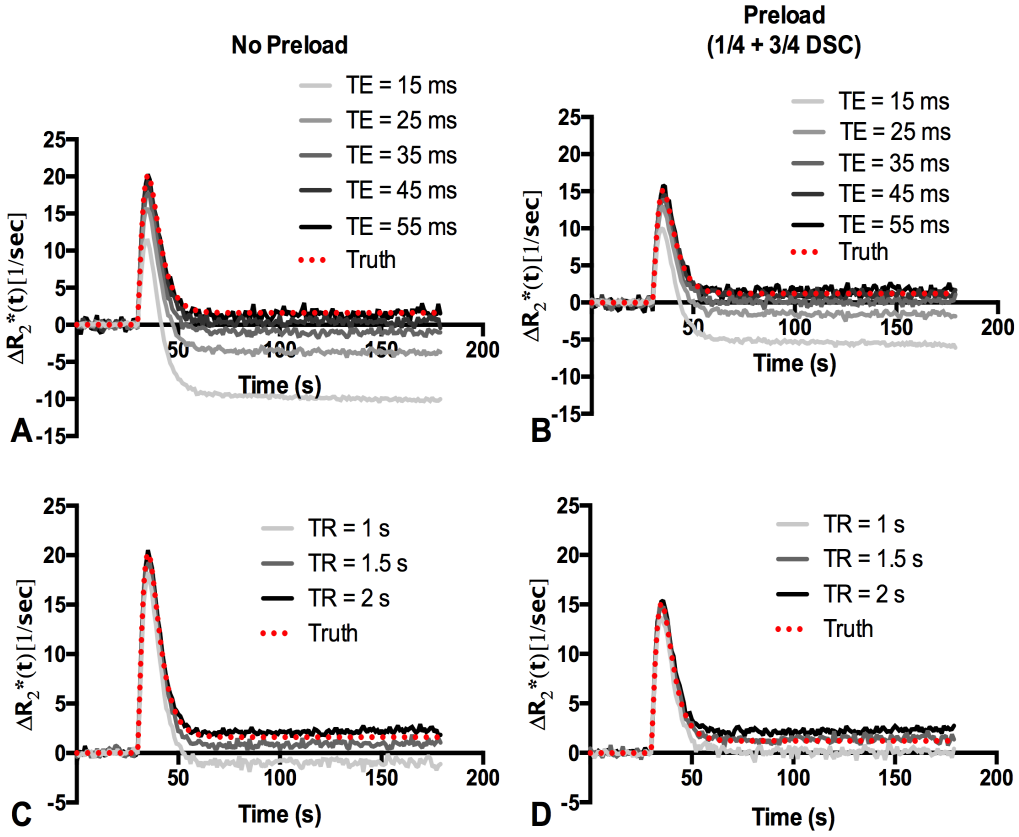

Fig. 2.3. Effect of TE and TR on DSC relaxation rate-time curves with flip angle=60°. A) $\Delta R_2^*(t)$ for various TEs using TR=1.0 s without preload and B) with ¼ dose preload, as compared to $\Delta R_2^*(t)_{gt}$. C) $\Delta R_2^*(t)$ for various TRs with a 60° flip angle and TE=35 ms with no preload and D) with ¼ dose preload.

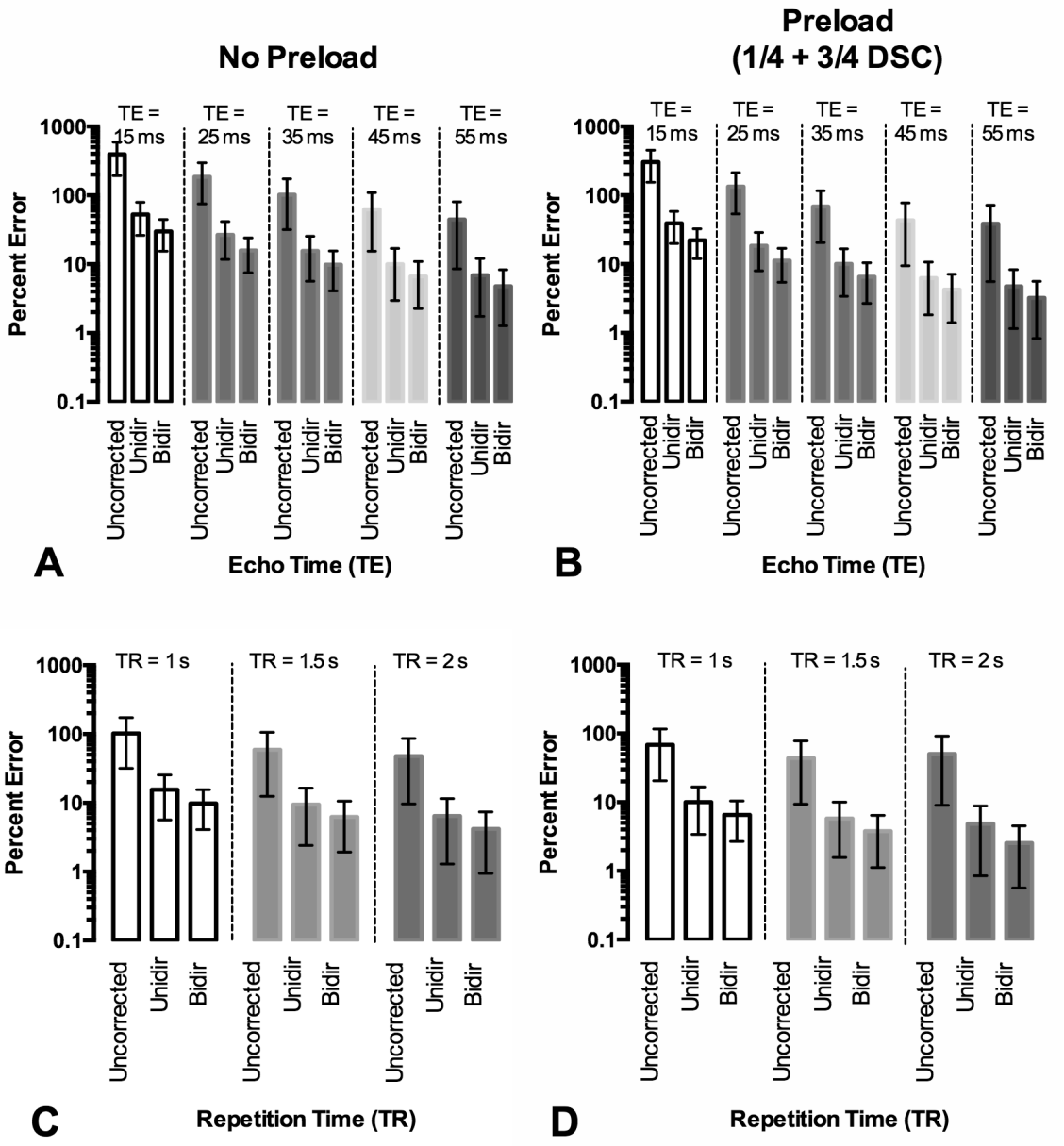

Fig. 2.4. Effect of TE and TR on CBV accuracy with flip angle=60°. A) Percentage error in CBV estimation for different TEs using TR=1.0 s without preload. B) Percentage error in CBV estimation for different TEs using TR=1.0 s with ¼ dose preload. C) Percentage error in CBV estimation for different TRs with a 60° flip angle and TE=35 ms with no preload. D) Percentage error in CBV estimation for different TRs with a 60° flip angle and TE=35 ms with ¼ dose preload.

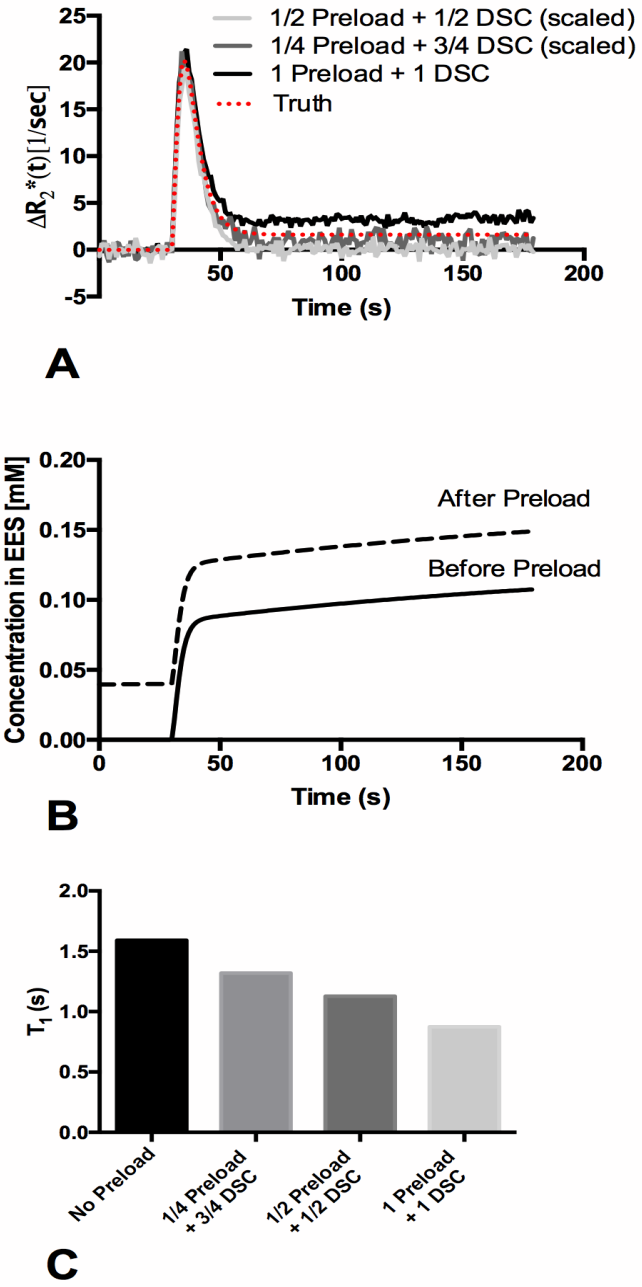

Fig. 2.5. Effects of preload dosage, incubation time, and truncation of corrected $\Delta R_2^*(t)$ on CBV fidelity. A) $\Delta R_2^*(t)$ with three different preload strategies. B) Concentration of contrast agent in the EES before and after preload. C) Change in T_1 of the tumor tissue following administration of various doses of preload.

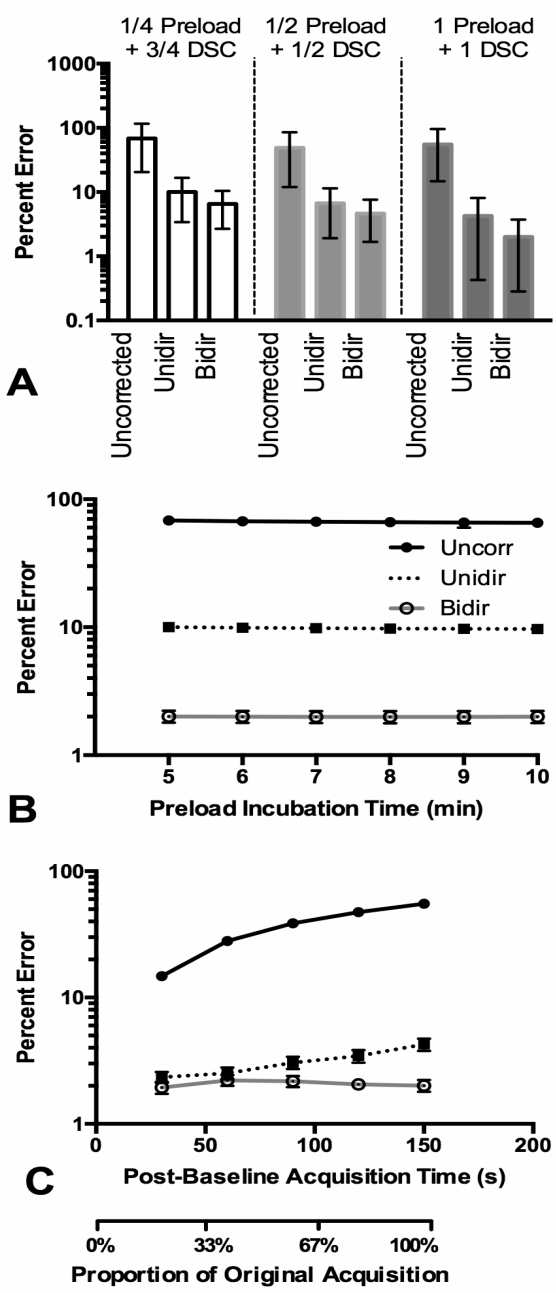

Fig. 2.6. Effects of preload dosage, incubation time, and truncation of corrected $\Delta R_2^*(t)$ on CBV fidelity. A) Percent errors in CBV for each preload dosage with 95% CI. B) Effects of preload incubation time on CBV estimation when using preload. C) Effects of truncation of the $\Delta R_2^*(t)$ curves and leakage correction strategies on CBV estimation when using a 1 dose preload.

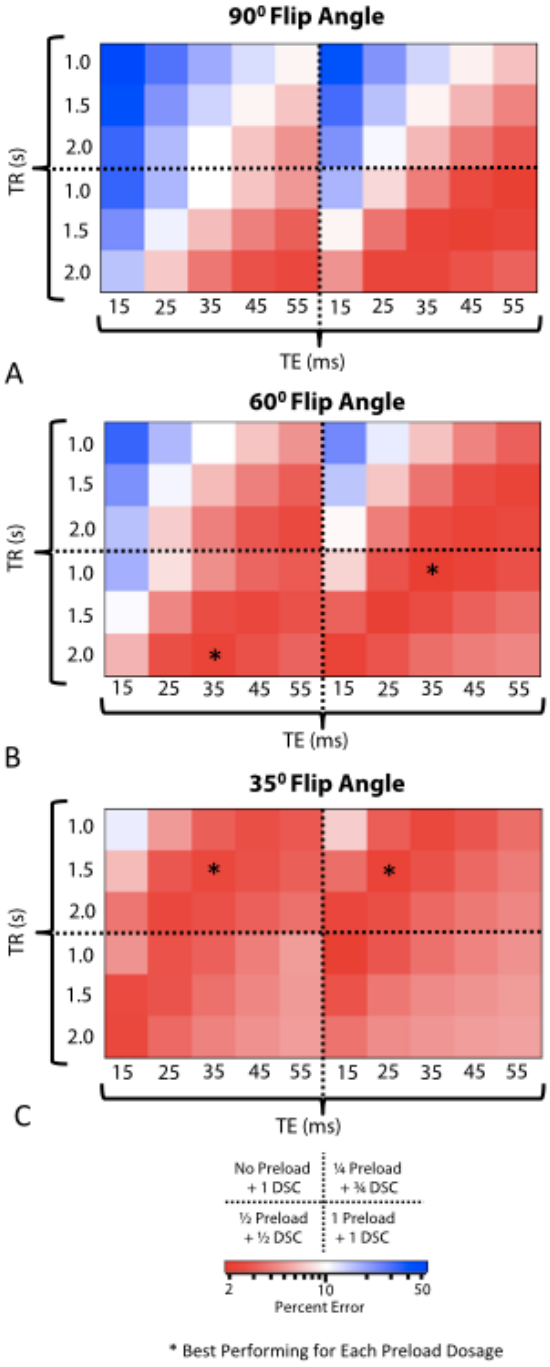

Fig. 2.7. Heat map diagrams depicting percent error in CBV estimation for combinations of acquisition protocols when using *Bidir* at 3.0T. Each quadrant within each subfigure represents a different preload dose. Each subfigure represents a different flip angle: A) 90°, B) 60°, and C) 35°. Optimal areas are in the dark red regions.

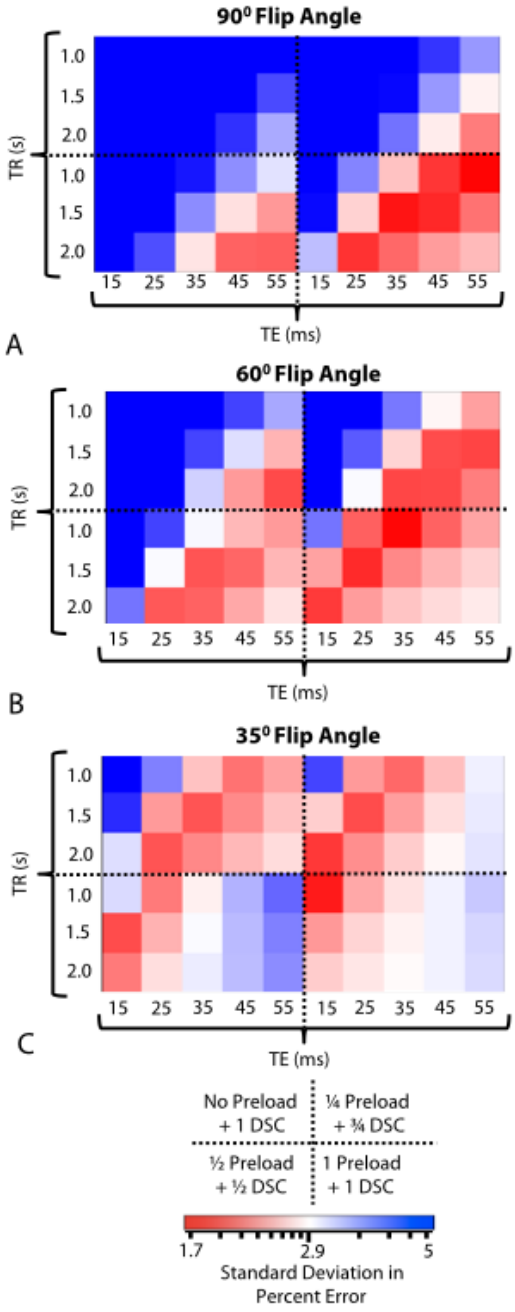

Fig. 2.8. Heat map diagrams depicting standard deviation of percent error in CBV estimation for combinations of acquisition protocols when using *Bidir*. Each quadrant within each subfigure represents a different preload dose. Each subfigure represents a different flip angle: A) 90°, B) 60°, and C) 35°.

Table 2.1. Best performing protocols with overlapping 95% confidence intervals with the overall best performing protocol (n = 250 tumors) using the bidirectional leakage correction. Protocols that fall within ASFNR recommendations[60] (TE = 25-35 ms, TR = 1.0-1.5 s) are underlined and italicized. The shaded box represents the protocols that use a total of two doses of gadolinium, whereas the un-shaded areas represent the use of only one dose of gadolinium.

Flip Angle (degrees)	**TE (ms)**	**TR (s)**	**Preload Dosage**	**Mean Uncorr. Error (%)**	**Mean Bidir. Error (%)**
35	35	1.5	None	67.4	2.47
35	25	1.5	¼	63.3	2.25
60	45	2.0	¼	49.7	2.25
60	55	1.5	¼	44.4	2.32
35	15	2.0	¼	56.3	2.45
35	35	1.0	¼	56.9	2.46
60	35	2.0	½	64.6	2.32
60	45	1.5	½	56.7	2.44
35	15	2.0	½	56.3	2.45
60	*35*	*1.0*	*1*	*55.2*	*2.01*
35	15	1.0	1	60.1	2.06
90	55	1.0	1	47.8	2.08
90	45	1.5	1	64.5	2.08
60	*25*	*1.5*	*1*	*66.9*	*2.12*
60	15	2	1	67.5	2.26
60	45	1	1	71.3	2.29
90	*35*	*1.5*	*1*	*49.7*	*2.30*
90	*25*	*2*	*1*	*59.3*	*2.37*
90	*35*	*2*	*1*	*77.7*	*2.38*
90	55	1.5	1	76.6	2.38

iii. Estimation of CBV Accuracy at 1.5 Tesla

While it is more ideal to use a 3.0 Tesla scanner for DSC-MRI due to the increased signal-to-noise ratio (SNR), the 1.5 Tesla scanners are still commonly used today. Tumor and gadolinium properties change at 1.5 Tesla; therefore, we examine the effects of scan-acquisition protocol and leakage correction at this magnetic field strength. The methodology in this section is similar to the one presented in the last section. However, there were a few modifications that were made in order to simulate the effects of scan-acquisition protocol and leakage correction algorithm on CBV estimation accuracy.

Modifications for 1.5 Tesla Simulation

A slightly different set of TEs and TRs were tested: TE = 15, 20, 25, 30, 35, 40, 45, 50, and 55 ms and TR = 500, 1,000, 1,500, and 2,000 ms. Tumor tissue T_{10} values are lower at 1.5 T and were simulated with the following distribution and range: T_{10} = 0.919 ± 0.096 s (range: 0.74 – 1.23) [61]. The T_1 relaxivity (r_1) of gadolinium is higher at 1.5T, while the T_2* relaxivity (r_2*) is lower. Because the r_2* values are difficult to estimate from the literature, the standard deviation was set at 20% of the mean: r_1 = 4.7 $mM^{-1}s^{-1}$ [54], $r_{2,P}$* = 44 ± 8.7 $mM^{-1}s^{-1}$ [55] (range: 21.2 – 66.0), and $r_{2,E}$* = 18 $mM^{-1}s^{-1}$ ± 3.6 (range: 8.7 – 27.3) [47] at 1.5T. Contrast-to-noise ratio (CNR) was halved for the 1.5T simulations as compared to the 3T simulations.

Results

At 1.5T, we again see that the bidirectional leakage correction outperforms the unidirectional (**Fig. 2.8**). In **Fig 2.9**, we display the rCBV error across the wide range of

scan-acquisition parameters. Owing to the diminished CNR and lower tissue T_{10}, few of the protocols at the low flip angle (35°) performed well. Instead, many of the optimal protocols are observed at 60° with varying preload dosages and 90° with full preload dose. Overall, the "best" protocol with the lowest overall mean percentage error utilized a 60° flip angle, TE/TR = 25/1500 ms with 1 dose preload at 1.5T, though the protocols with overlapping 95% CIs are shown in **Table 2.2**.

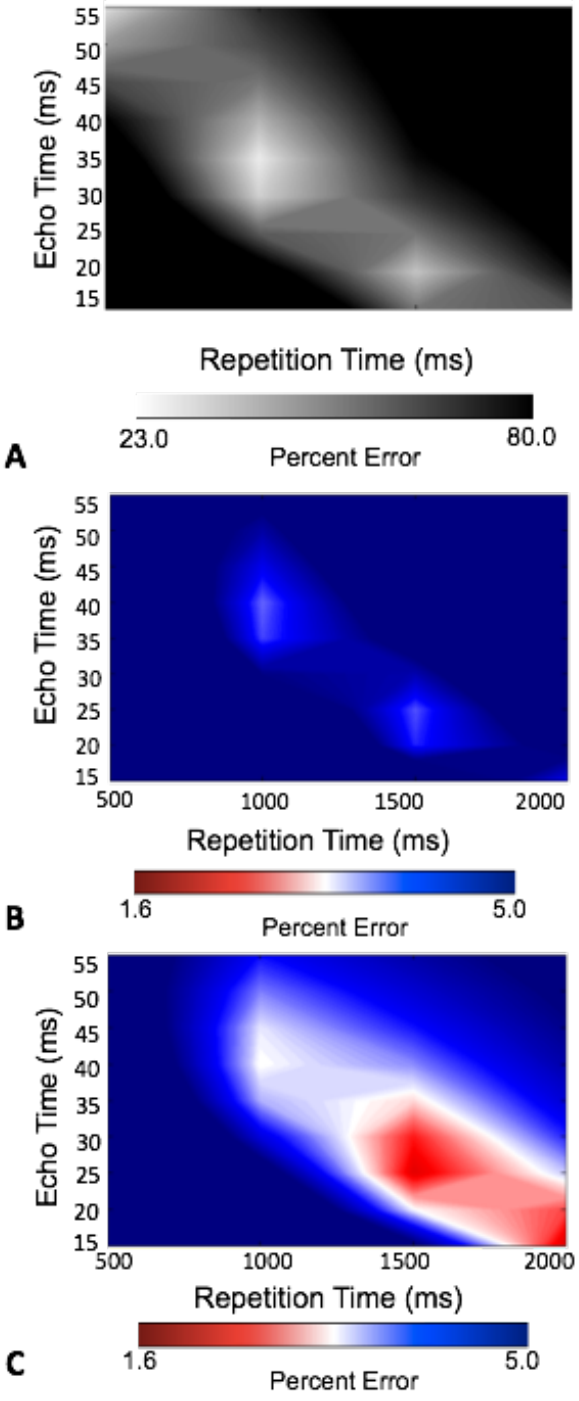

Fig. 2.8. Percentage errors in rCBV after A) no leakage correction, B) unidirectional leakage correction, and C) bidirectional leakage correction. The lowest errors (dark red regions) are observed using the bidirectional leakage correction.

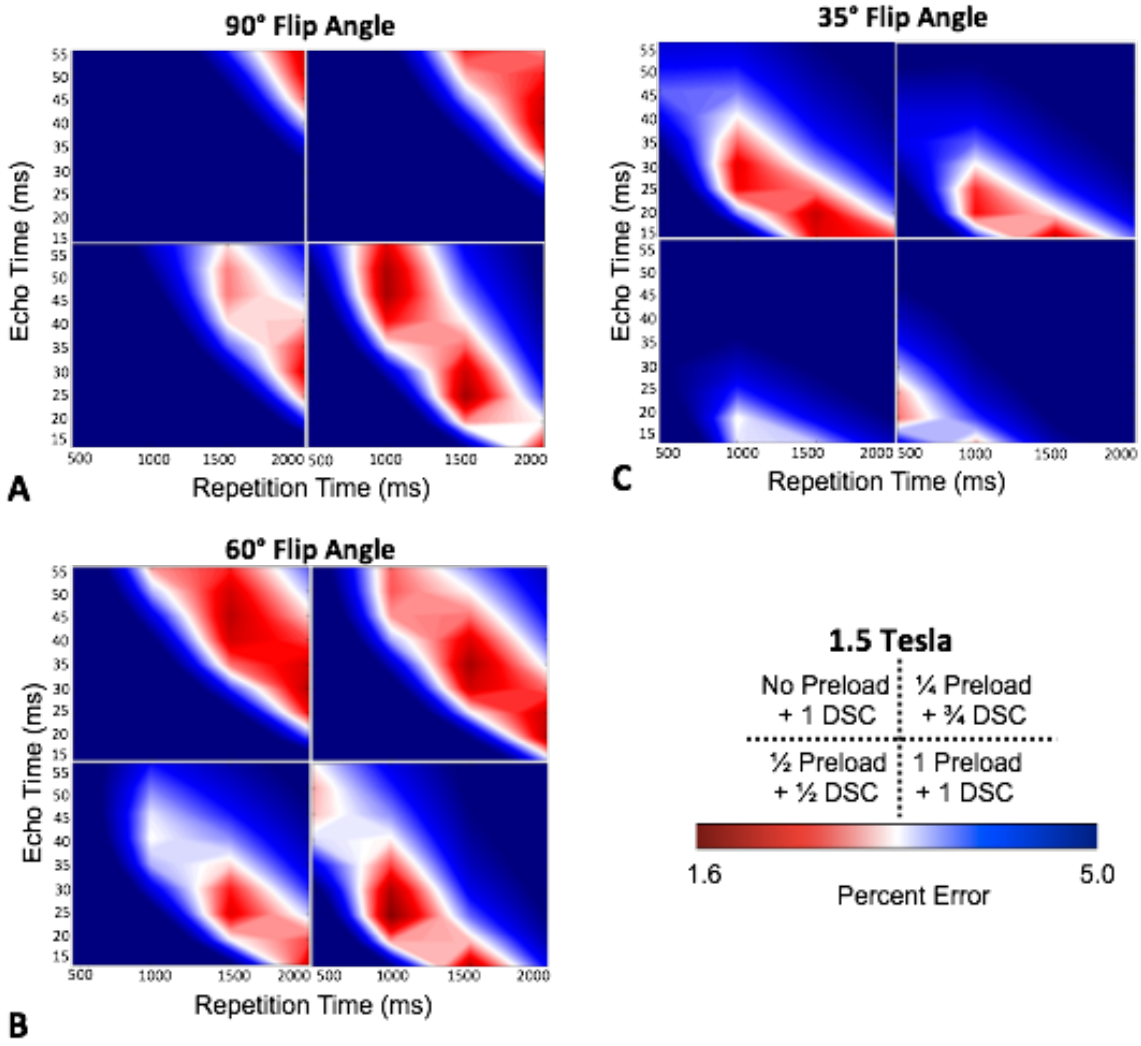

Fig. 2.9. Heat map diagrams depicting percent error in CBV estimation for combinations of acquisition protocols when using *Bidir* at 1.5T. Each quadrant within each subfigure represents a different preload dose. Each subfigure represents a different flip angle: A) 90°, B) 60°, and C) 35°. Optimal areas are in the dark red regions.

Table 2.2. Best performing DSC-MRI protocols at 1.5T with overlapping 95% confidence intervals with the overall best performing protocol (n = 250 tumors) using the bidirectional leakage correction. Protocols that fall within ASFNR recommendations[60] (TE = 40-45 ms, TR = 1.0-1.5 s) are underlined and italicized.

Flip Angle (degrees)	TE (ms)	TR (ms)	Preload Dosage
90	55	2,000	None
90	40	2,000	¼
90	45	2,000	¼
90	30	2,000	½
90	25	1,500	1
90	30	1,500	1
90	*45*	*1,000*	*1*
90	50	1,000	1
60	30	2,000	None
60	35	2,000	None
60	*40*	*1,500*	*None*
60	*45*	*1,500*	*None*
60	50	1,500	None
60	20	2,000	¼
60	25	2,000	¼
60	30	1,500	¼
60	35	1,500	¼
60	15	2,000	½
60	15	1,500	1
60	25	1,000	1
60	30	1,000	1
35	20	1,500	None
35	15	1,500	¼

iv. Discussion

The purpose of this study was to evaluate the influence of various DSC-MRI acquisition strategies and post-hoc leakage correction algorithms on the fidelity of CBV estimation. In general, the performance of both leakage correction algorithms improves as the leakage contaminated $\Delta R_2^*(t)$ curve more closely approximates $\Delta R_2^*(t)_{gt}$. In both simulations, better performances were found at 60 degrees since the flip angle is less T_1-weighted than the 90 degree flip angle with the bidirectional leakage correction. Furthermore, a much more "homogeneous" performance is seen for the double dose contrast, as many more protocols were "optimal" with the double dose. This would seem to imply that this scheme is less sensitive to the physiologic variations that would impact the estimates of $\Delta R_2^*(t)$.

As has been established previously, increased T_2^*-weighted leakage results from lower flip angle, longer TR, longer TE, and higher preload dosage[25, 62]. Given that the errors before and after leakage correction are generally correlated, the optimal strategies minimize errors in uncorrected CBV, which can be accomplished by balancing T_1- and T_2^*-weighted leakage effects. Therefore, the optimal protocols balance these two opposing effects so that the DSC-MRI curves do not deviate too much from the "ground truth". For example, a TR of 1.0 s, which is relatively T_1-weighted, can be offset by using a full dose of preload, which is quite T_2^*-weighted. Some of the optimal protocols, on the other hand, take a middle-of-the-road approach (i.e. 60° flip angle or TE = 35 ms) such that none of the parameters cause the DSC-MRI curves to be overly affected by T_1-weighted or T_2^*-weighted leakage effects.

Our results also suggest that the mechanism by which preload increases CBV fidelity is by increasing T_2* weighting and decreasing T_1 weighting of the ΔR_2*(t) curves rather than by decreasing flux of contrast agent diffusion into the EES. While preload and post-processing leakage correction algorithms have been shown to work synergistically in many cases, including intermediate-to-high flip angle acquisitions[49], it is also possible for preload to over compensate and worsen the deviation of the leakage-contaminated ΔR2*(t) curve compared with the "ground truth," which agrees with the conclusion drawn by Hu *et al*[26]. Furthermore, sufficient preload correction was found between 6-10 minutes, which agrees with Hu *et al*.[26] and Kassner *et al*[63].

The bidirectional leakage correction accounts for backward flux of contrast agent and was shown to reduce CBV error compared to the unidirectional leakage, with the exception of one protocol. Both leakage correction algorithms work by first performing a least squares fit of the model-generated corrected ΔR2*(t) curve plus the leakage term, and then subtracting the original ΔR2*(t) curve by the calculated leakage term. As such, if the computed leakage term does not include the back flux of contrast agent, it can cause the corrected ΔR2*(t) curve to adopt a shape noticeably different than C_p (Eq. 2.3), thereby overestimating and underestimating the "ground truth" curve immediately following the first pass of the bolus. This results in CBV estimates obtained using the unidirectional algorithm having approximately twice the error compared to estimates

These studies have several notable limitations. In the first simulation, we did not account for errors arising from either variations in MTT (including bolus dispersion) or bolus delay, both of which would serve to increase the percent error for the leakage correction algorithms presented in the study due to MTT-sensitivity. Therefore, the

percentage errors are meant to be relative, with many of the optimal protocols providing a balance between T_1 and T_2* leakage effects over the population of tumors. Another limitation is the lack of more sophisticated integration of all of the effects of microvascular and microcellular morphologies on DSC-MRI data, including but not limited to the arbitrary geometry of the underlying vessels [64, 65]. Furthermore, the noise modeled does not take into account potential sources, such as coil quality, slice thickness, and the use of a global AIF. Much of the population data used for these tumors were acquired in small cohorts, and a study in a larger population would be required for more accurate modeling of the tumor population characteristics, particularly r_2*. Finally, the results in the simulation warrant validation in real patients. Testing every combination of MRI protocols is infeasible in real patients. Furthermore, it is currently impossible to ascertain the ground truth rCBV; however, these results could be validated in real brain tumors using an extension of the Paulson *et al.*[45] methodology, in which the top performing protocols are tested against each other for variability between scans.

The current studies demonstrate that the choice of image acquisition and preload dosing and/or fractionation have a tremendous impact on the fidelity of CBV estimation. In particular, the unidirectional method is much more sensitive to the differences in scan-acquisition protocol than the bidirectional method. With the bidirectional model, results suggest a variety of acquisition strategies can be used to obtain similar accuracy of CBV estimation. To compute the most accurate CBV, efforts should be focused on standardizing a DSC-MRI acquisition strategy that minimizes errors in the underlying leakage-contaminated ΔR_2*(t) curve by balancing T_1 and T_2* contamination effects over

the tumor population, which will in turn reduce the residual errors in CBV estimation following leakage correction.

Chapter III. Verifying Improved Accuracy and Technical Performance of Bidirectional rCBV Estimation in Human Gliomas

Preface

Section ii of this chapter, "Verifying Improvement in Bidirectional Leakage-Correction Modeling via the AIC and Correlation with DCE-MRI", is based on the following publication:

Leu K, Boxerman JL, Cloughesy TF, Lai A, Nghiemphu PL, Liau LM, Pope WB, Ellingson BM. Improved Leakage Correction for Single-Echo Dynamic Susceptibility Contrast (DSC) Perfusion MRI Estimates of Relative Cerebral Blood Volume (rCBV) in High-grade Gliomas by Accounting for Bidirectional Contrast Agent Exchange. *AJNR. Am J Neuroradiol.* 2016; 37:1440-6.

i. Introduction

In this chapter, we examine how well the bidirectional model fits acquired data versus the unidirectional. More specifically, we focus on technical aspects of model fitting, beginning with examining whether the bidirectional model, with its extra free parameter, overfits the data. We also compare the permeability curves generated by the leakage correction algorithms to independently acquired dynamic contrast enhanced (DCE)-MRI data. In brief, DCE-MRI[42] is a T_1-weighted perfusion MRI technique in which the leakage of contrast agent is monitored over time. We therefore hypothesize that the leakage curves from the leakage correction algorithms and the DCE-MRI would be similar. Finally, we examine whether the rCBV differences the unidirectional and

bidirectional are potentially meaningful by studying the similarity of rCBV between different scans in the same patient and echoes of the same multi-echo scan.

ii. Verifying Improvement in Bidirectional Leakage-Correction Modeling via the AIC and Correlation with DCE-MRI

This section focuses on model fitting, examining whether the bidirectional leakage correction matches our expectations for a combined indicator dilution theory and leakage model. We begin by showing that the DSC-MRI curve allows for more flexibility from a modeling perspective with the incorporation of backflow. We then compare how the bidirectional leakage correction and the unidirectional leakage correction perform when fitting raw DSC-MRI data using the Akaike Information Criterion (AIC), a measure that rewards models for minimizing the sum of square errors and penalizes for extra parameters. Both the unidirectional and bidirectional leakage correction algorithms can also be broken down into the sum of two parts. The first term in Eq. 1.26, which describes the contribution of signal from the contrast agent within the blood plasma, and the last two terms in Eq. 1.26, which describe the total T_1/T_2* contribution from the leakage of contrast agent. We compare the contribution of leakage of contrast agent with that of DCE-MRI, a T_1-weighted modality that measures the leakage of contrast agent into the extravascular, extracellular space. We hypothesized that incorporating bidirectional contrast agent transport into the original DSC-MRI signal model improves model fitting and thereby rCBV estimates in brain tumors. To test this hypothesis, we compared model-based DSC-MRI leakage correction methods with and

without consideration of bidirectional transport using DSC-MRI and DCE-MRI data in high-grade gliomas.

Patient Population

A total of 24 sequential GBM patients with histologically proven GBM treated with maximal surgical resection followed by radiotherapy and concurrent temozolomide and both DSC-MRI and DCE-MRI performed at initial tumor progression were studied. Of these patients, two patients illustrated no bolus of contrast during DSC acquisition and one DSC dataset was corrupted by significant motion. Thus, a total of 21 patients (15 men; mean age 54 years, range 30-73) were included in the final cohort. Progression was defined prospectively by the treating neuro-oncologists if subsequent scans showed more than 2 sequential months of increasing contrast enhancement and worsening mass effect or evidence of neurologic decline. Specifically, progression was defined as $\geq$ 25% increase in the sum of enhancing lesion volumes, new enhancing lesions > 1 cm maximum dimension, an unequivocal qualitative increase in non-enhancing tumor, or an unequivocal new area of non-contrast enhancing tumor. Additionally, progression must have occurred more than 3 months following completion of radiation therapy. All participants gave informed written consent to have both DSC-MRI and DCE-MRI data collected. All procedures complied with the principles of the Declaration of Helsinki and were approved by the Institutional Review Board at our institution.

DSC-MRI and DCE-MRI

We retrospectively reviewed DSC-MRI and DCE-MRI scans (3T, Siemens Trio or Skyra, Siemens Healthcare, Erlangen, Germany) acquired in the same scan session in all 21 patients. T_1 maps were generated from 5 pre-contrast T_1–weighted images (flip angle=5°, 10°, 15°, 20°, 30°) prior to DCE-MRI (3D spoiled gradient echo sequence, 16 slices, 130 time points, 5 s time resolution, TE/TR=1.87/5ms, 25^0 flip angle, 3 mm slice thickness, 256x192 matrix, 24 cm FOV). The DCE-MRI was acquired for ~10 minutes, which is the waiting time between preload and DSC contrast injections for this study. Contrast agent bolus (0.1 mmol/kg) (Magnevist, Bayer HealthCare) was injected after 10-13 baseline images, serving as pre-load[45] for DSC-MRI (gradient echo EPI, TE/TR=32/1840ms, 35^0 flip angle, 120 time points, bolus injection after 20-25 baseline images, 9-20 slices, 5 mm slice thickness, 128x128 matrix size, 24 cm FOV). The same amount of contrast agent was used for the DSC-MRI studies. Conventional post-contrast T_1-weighted imaging was subsequently performed. Patients were excluded if DCE-MRI or DSC-MRI was corrupted by motion or technical error.

Image Registration and ROI Selection

All conventional and DCE-MRI images for each subject were registered to baseline DSC-MRI images using 12-degree of freedom affine transformation with a mutual information cost function (FSL; http://www.fmrib.ox.ac.uk/fsl). If required, manual alignment was subsequently performed (tkregister2, Freesurfer; surfer.nmr.mgh.harvard.edu). Contrast enhancing tumor regions of interest (ROIs) were defined in three dimensions using custom scripts (AFNI; http://afni.nimh.nih.gov/afni), excluding hemorrhage, large vessels, and central necrosis, followed by manual editing to

exclude non-lesion voxels.[66] Tumor sizes ranged from 2.8 to 106.6 mL, with an average enhancing volume of 40.1 ± 28.4 mL (s.d.). Spherical ROIs of 1.6 mL were also selected in normal-appearing, contralateral white matter for rCBV normalization.

Computation of DSC-MRI rCBV

All simulations and calculations were performed in MATLAB using custom scripts. Uncorrected rCBV was calculated from trapezoidal integration of the original DSC-MRI relaxation rate-time curve, $\Delta\hat{R}_2^*(t)$. The whole-brain average relaxation rate for non-enhancing voxels (Eqs. 1.8–1.9 in "Bidirectional Leakage Correction Theory" section of Chapter I) was used for both the original Boxerman-Weisskoff model[31] (*Unidir-model*) and the new bidirectional exchange model (*Bidir-model*). Linear least squares optimization was used to determine the free parameters for both the *Bidir-model* (via Eq. 1.26) and the *Unidir-model* (Eq. 1.24, with $k_{ep} = 0$) algorithms, and corrected rCBV was computed from Eq. 1.27. The average runtime per patient in MATLAB was 19.5±6.7s for the *Bidir-model* and 18.3±6.2s for the *Unidir-model* (3.2 GHz Intel Core i5, 32 GB RAM). Tumor rCBV for each method was subsequently normalized to median rCBV within the normal appearing white matter ROI.

Simulation of DSC-MRI rCBV

Whole-brain average relaxation rate, $\Delta\bar{R}_2^*(t)$, was chosen from a sample patient and corresponds to the curve with K_1=1, K_2=0, and k_{ep}=0. K_2=0.05 (adding T1-dominant leakage), with k_{ep}=0 was set to simulate the *Unidir-model*. A nonzero k_{ep} (0.002 or

0.005) was used to simulate the *Bidir-model* of $\Delta\hat{R}_2^*(t)$. For k_{ep}=0.1, the simulation is reflective of the correction of relaxation rate curves at "artery-like" voxels.

Goodness of Fit Analysis

For each enhancing tumor voxel for all patients, we computed the Akaike Information Criterion (AIC) between leakage-contaminated relaxation rate $\Delta\hat{R}_2^*(t)$ (Eq. 1.20) and its model fit for the *Unidir-model* and *Bidir-model*:

$$AIC = n \cdot \ln(RSS/n) + 2(p+1),$$

where n is the number of fitted time points (injection to end of DSC-MRI acquisition), RSS is the sum of the squared residuals, and p is the number of free parameters (2 for the *Unidir-model*, 3 for the *Bidir-model*).[67] Differences in the *Unidir-model* and *Bidir-model* AIC were calculated for all voxels where k_{ep}>0.

We also computed Euclidean distance (square root of the sum of the squared differences) between the interstitial leakage relaxation rate curves, $\Delta R_{2,E}^*(t)$, generated by the *Unidir-model* and *Bidir-model* corrections and DCE-MRI signal, where the DCE-MRI signal was up-sampled from a 5-second resolution to a 1.8-second resolution to match that of the DSC-MRI data via linear interpolation using the MATLAB function "resample". Because interstitial leakage relaxation rate curves and DCE-MRI signal have units of 1/sec and mM, respectively, both were standardized to an area under the curve equal to unity and vectorized for computation of Euclidean distance. Higher AIC and ED imply worse fits. Two-sample t-tests were used to compare whether the AIC and ED measurements were significantly different between the two leakage correction methods.

Post-processing of DCE-MRI

DCE-MRI imaging biomarkers – k_{ep} and K^{trans} – were derived via a fit to the Tofts model[42]. As described above, the temporal resolution of the DCE-MRI data was up-sampled to match the DSC-MRI data. For the DCE-MRI analysis, the "whole brain average" served as the arterial input function (AIF) for the DCE model fit. This was done to mirror the DSC *Bidir-model* analysis, in which the "whole brain average" effectively serves as the AIF Voxels with highly fluctuating time courses in either the DSC or DCE images were eliminated from the analysis.

Correlation between DSC- and DCE-derived Imaging Biomarkers

DSC-MRI imaging biomarkers – k_{ep} and rCBV – were derived as described in the "Bidirectional Leakage Correction Theory" section in Chapter I. Voxel-wise Pearson correlation coefficients between the DSC- and DCE-derived parameters were performed in MATLAB within contrast-enhancing tumor only for each patient independently. In this study, we report means and standard deviations of the correlation coefficients from all 21 patients.

Results

Simulation of the Bidir-model

Fig. 3.1 compares simulated total leakage contaminated relaxation rate, $\Delta\hat{R}_2^*(t)$, (**Fig. 3.1A**) and the component from interstitial leakage, $\Delta R_{2,E}^*(t)$, (**Fig. 3.1B**) for various conditions according to the Tofts model[42] assuming T_1-dominant leakage-associated relaxation enhancement. For the *Unidir-model*, $\Delta R_{2,E}^*(t)$ rises over time in the absence of

washout. For nonzero k_{ep}, there is less rise in $\Delta R^*_{2,E}(t)$ and closer approximation of the tail of $\Delta \hat{R}^*_2(t)$ to $\Delta \bar{R}^*_2(t)$, reflecting tumors with different contrast agent pharmacokinetics. For k_{ep}=0.1, the tail of $\Delta R^*_{2,E}(t)$ approaches zero, but because the first-pass of $\Delta \hat{R}^*_2(t)$ differs from that of $\Delta \bar{R}^*_2(t)$, correction of relaxation rate curves at "artery-like" voxels using K_1 and K_2 is still required to achieve accurate rCBV estimates.

Fig. 3.1C plots sample $\Delta \hat{R}^*_2(t)$, with T_2*-dominant leakage-associated relaxation enhancement for a representative patient, with superimposed *Unidir-model* and *Bidir-model* fit relaxation rate curves. In this example, the *Unidir-model* overestimates the first-pass curve, underestimates the second and third passes, and overestimates the tail. The *Bidir-model* better approximates $\Delta \hat{R}^*_2(t)$ over all time points, visually, and has substantially improved AIC, quantitating an improved fit to the total leakage contaminated relaxation rate curve.

Fig. 3.1D plots standardized DCE-MRI signal for the tumor voxel used in **Fig. 3.1C**, with superimposed standardized interstitial leakage relaxation rate curves, $\Delta R^*_{2,E}(t)$, from the *Unidir-model* and *Bidir-model*. The standardized interstitial leakage relaxation rate continually rises over time for the *Unidir-model*, whereas it better tracks standardized DCE-MRI for *Bidir-model* with substantially improved Euclidean distance.

Goodness of Fit Analysis

Fig. 3.2 plots the percentage of voxels where the *Bidir-model* outperformed *Unidir-model* for AIC and Euclidean distance metrics in whole brain and tumor for the 21 GBM patients. The *Bidir-model* had better AIC performance than *Unidir-model* in greater than 50% of whole-brain (mean±standard deviation = 71%±6%, $p<0.0001$) and tumor

(77%±9%, p<0.0001) voxels in all patients, and better Euclidean distance performance in greater than 50% of whole-brain voxels (80%±9%, p<0.0001) for all patients, and tumor voxels (62%±17%, p=0.0041) for 17 of the 21 patients. All were statistically significant for a one-sample t-test with null hypothesis of 50%.

Correlation between DSC-derived and DCE-derived imaging biomarkers

We then performed a voxel-wise correlation between the DSC-derived imaging biomarkers from the bidirectional leakage correction algorithm (k_{ep} and rCBV) with the DCE-derived imaging biomarkers (k_{ep} and K^{trans}). Across the 21 patients, the Pearson correlation coefficient between the two k_{ep} measurements was 0.74±0.13 across the 21 patients, with a weak correlation between the Pearson's correlation coefficient and tumor size (r = 0.11). **Fig. 3.3** demonstrates an example of the correlation between DSC- and DCE-derived k_{ep}. A correlation test was performed between the bidirectional model-derived rCBV and DCE-derived K^{trans}, with a moderate correlation of 0.49±0.22. A moderate correlation was also found between rCBV and vp at 0.54±0.12. Finally, the correlation between the same rCBV and k_{ep} was r = 0.29±0.26. The average K^{trans} value was 0.0015±0.0018 s^{-1} (0.09±0.11 min^{-1}), DCE-k_{ep} was 0.0050±0.0023 s^{-1} (0.30±0.14 min^{-1}), DSC-k_{ep} was 0.0057±0.0042 s^{-1} (0.34±0.25 min^{-1}), v_p was 0.01±0.01, and rCBV was 1.98±1.24.

Difference in rCBV between the Bidir-model and Unidir-model

Fig. 3.4 compares rCBV maps processed without leakage correction, and with the *Unidir-model* or *Bidir-model*, in two different GBM patients, one with T_1-dominant leakage (K_2>0) on average in contrast enhancing tumor voxels and the other with T_2*-

dominant leakage (K_2<0). For all patients, average uncorrected rCBV was 1.98±1.24, average *Unidir-model* corrected rCBV was 1.59 ± 0.89, and average *Bidir-model* corrected rCBV was 1.35±0.80. The average difference between *Unidir-model* corrected and *Bidir-model* corrected rCBV was 16.6±14.0%. A closer inspection of the T_2*-dominant versus T_1-dominant voxels (as defined by a negative or positive K_2, respectively) revealed that the difference between the two correction methods in T_2*-dominant voxels was 37.7±42.6%, while the same metric for T_1-dominant voxels was 5.8±3.4%.

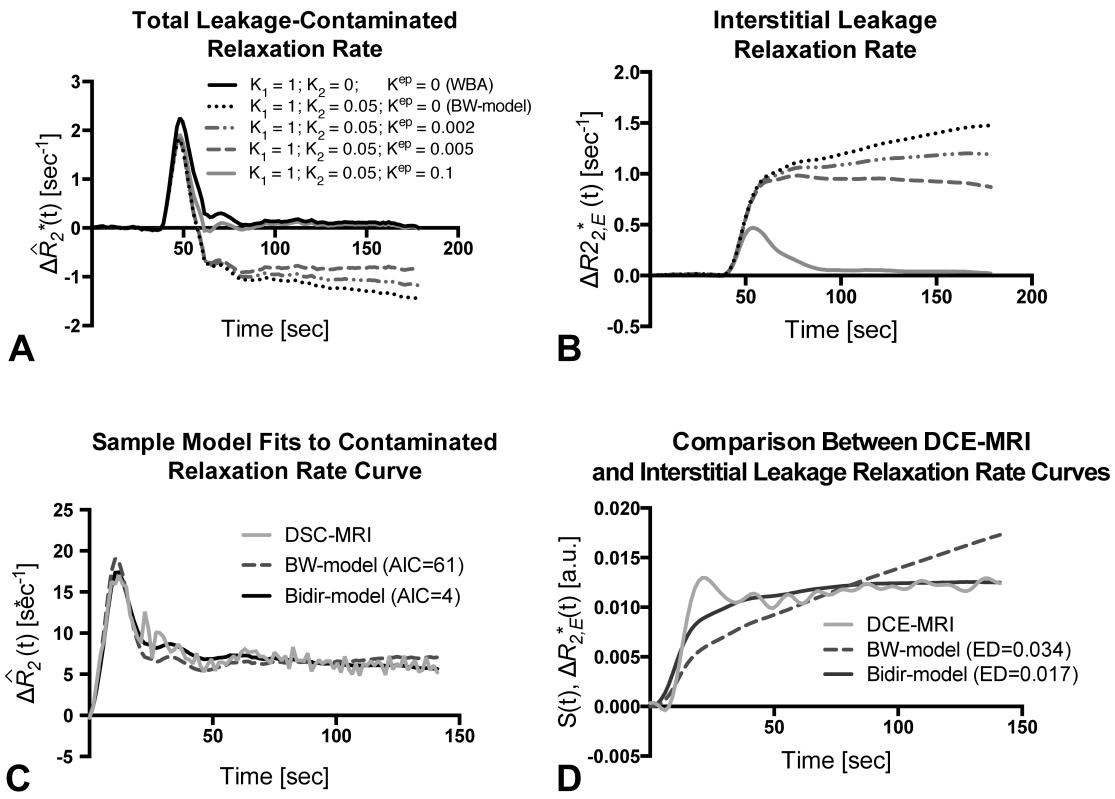

Fig. 3.1. Sample simulated model results for all GBM patients. (A) Total leakage contaminated relaxation rate and the component from interstitial leakage (B) for T_1-dominant leakage-associated relaxation enhancement. Whole-brain average relaxation rate (WBA) is simulated with K_2=0 and k_{ep}=0. K_{ep}=0 with non-zero K_2 simulates the *Unidir-model*. Inclusion of a washout term (non-zero k_{ep}) in the *Bidir-model* yields less rise in $\Delta R^*_{2,E}(t)$ and closer approximation of the tail of $\Delta \hat{R}^*_2(t)$ to the WBA. (C) The *Bidir-model* fit to sample leakage-contaminated relaxation rate curve has substantially improved AIC compared to *Unidir-model* for T_2*-dominant leakage-associated relaxation enhancement in a GBM patient. (D) Standardized interstitial leakage relaxation rate from the *Bidir-model* better tracks standardized DCE-MRI signal than the *Unidir-model* for the tumor voxel used in (C) with substantially improved Euclidean distance.

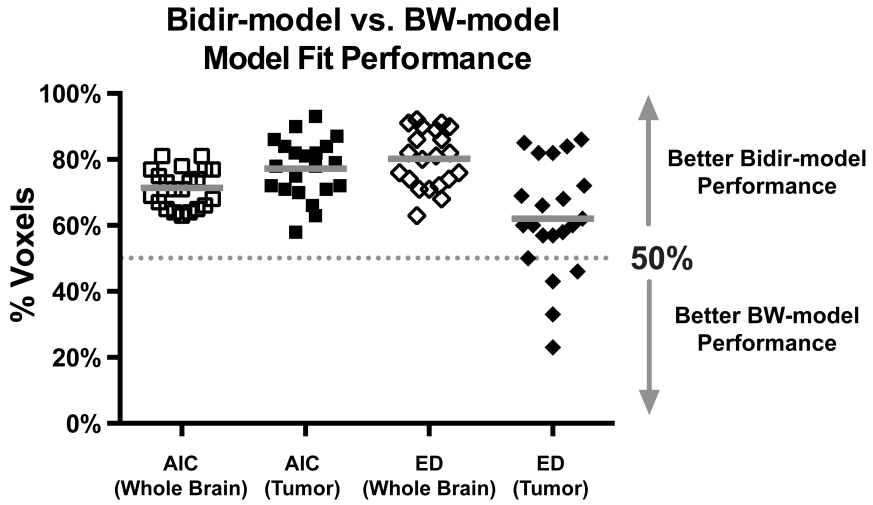

Fig. 3.2. Percentage of voxels (with mean and standard deviation) where the *Bidir-model* outperformed *Unidir-model* on Akaike Information Criterion (AIC) and Euclidean distance (ED) metrics within whole brain and tumor for all 21 GBM patients. The gray line represents the group mean percentage of voxels.

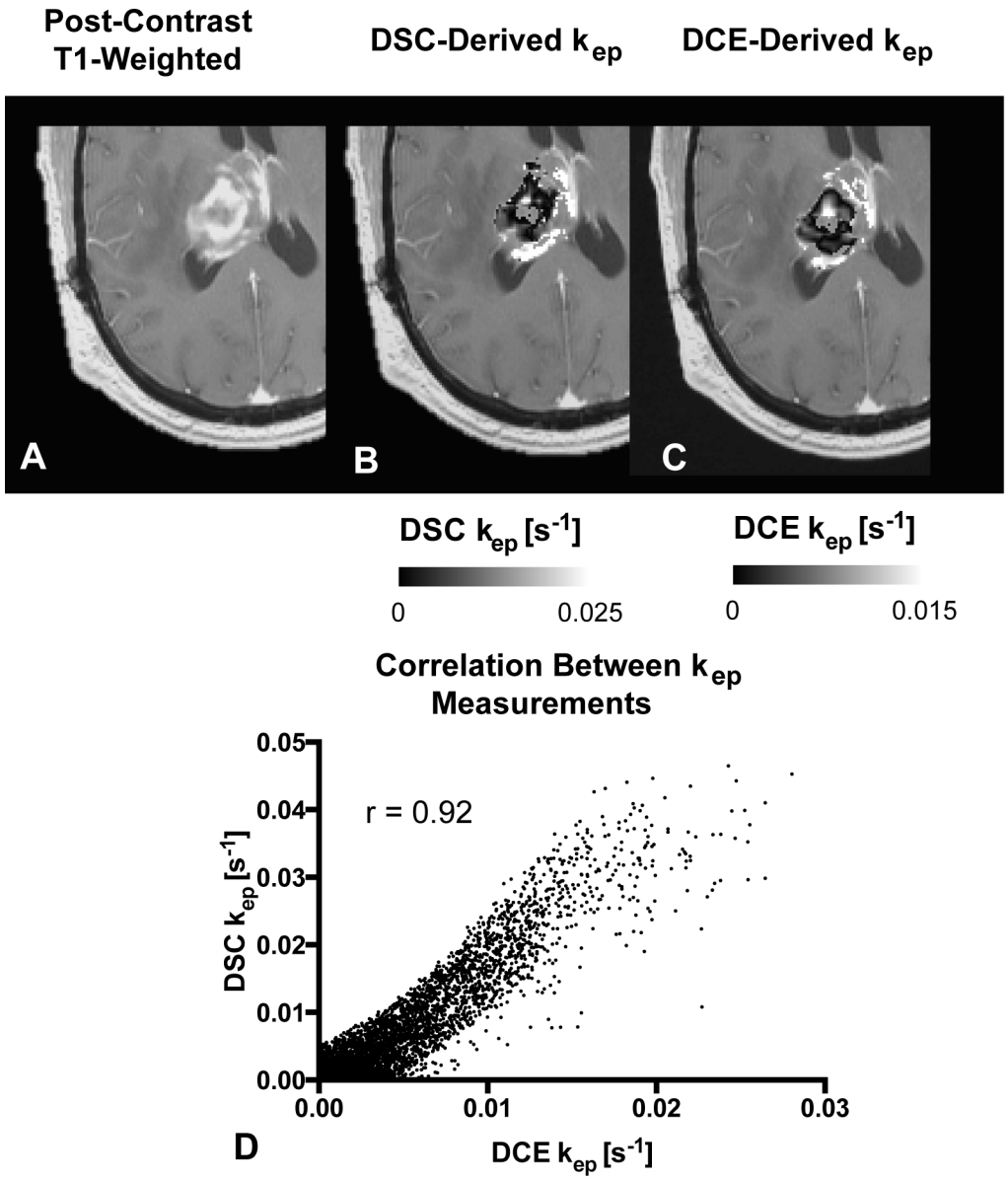

Fig. 3.3. Comparison between DSC- and DCE-derived k_{ep} measurements within tumor. A) Example of anatomical MRI of a patient with recurrent glioblastoma. B) DSC-derived k_{ep} measurements within tumor. C) Corresponding DCE-derived k_{ep} measurements. D) Scatter plot between (B) and (C) demonstrate high correlation (r = 0.92) for this tumor. Note that areas of low k_{ep} are similar in both DSC- and DCE-derived maps.

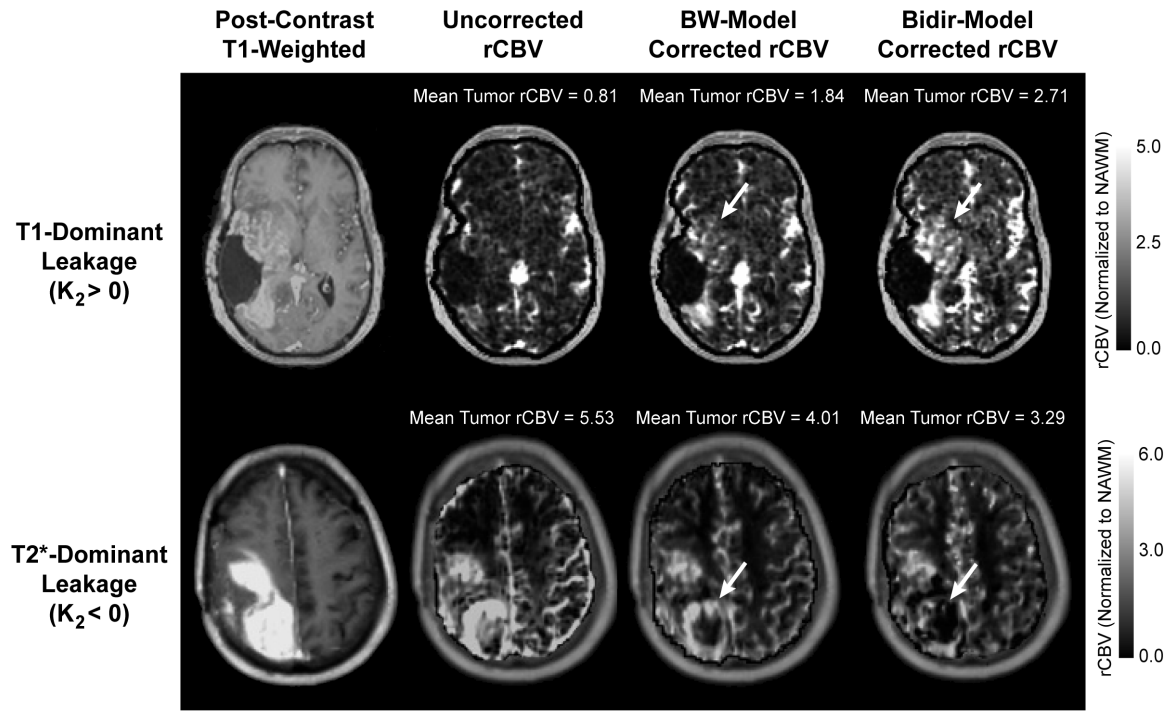

Fig. 3.4. Comparison of uncorrected, *Unidir-model* corrected, and *Bidir-model* corrected rCBV in a GBM with T_1-dominant leakage on average in contrast enhancing voxels (first row) and a GBM with T_2*-dominant leakage (second row). For T_1-dominant leakage, mean tumor rCBV is underestimated using the *Unidir-model* compared with the *Bidir-model*, with the converse true for T_2*-dominant leakage. Arrows depict regions of the tumor with large changes in estimated rCBV between leakage correction models.

iii. Verifying Improvement in Estimated rCBV via Inter-scan Reproducibility

In the last section, we established that the difference in rCBV between the bidirectional and unidirectional leakage correction algorithms is ~16.6%. We thus examine if that difference can be clinically meaningful. More specifically, if an algorithm can more reliably calculate the rCBV, we would expect that the rCBV would be more closely reproduced between two scans of the same patient collected within a few days of each other, provided that no treatment was given in the interim. In this study, we examine the rCBV in patients who had two scans prior to treatment separated by 3-7 days (**Figure 3.5**). More specifically, we use the coefficient of variation between the median rCBV in the two tumors as our metric to determine rCBV reproducibility. We hypothesized that the bidirectional correction method would have more similar rCBV between scans than either the unidirectional or the uncorrected.

All thirty patients (recurrent glioblastoma, WHO grade IV) provided informed consent to be included in this study. Standard and perfusion-weighted imaging data were acquired on 3T MRI systems (Siemens) at three total time points: 1) 3-7 days before first treatment of cediranib (average of 5.7 days), 2) one day before treatment and 3) one day after treatment. Three patients did not have imaging at time point 1, and one patient did not have imaging at time point 2. Data was acquired between January 2006 and February 2007.

Standard anatomic imaging consisted of an axial T_1-weighted fast spin-echo. Perfusion-weighted imaging was obtained via a dual-echo combined spin-and-gradient echo echoplanar sequence. Flip angle was 90°, echo times (TE) were 34/104 ms, repetition time (TR) was 1.33 s, with matrix size 128 x 128, slice thickness 5 mm with

2.5 mm interslice gap, and total voxel size 1.7 x 1.7 x 5 mm. A total of 120 time points were acquired. Prior to the start of DSC-MR imaging, 0.1 mMol/kg of contrast agent (gadopentate dimeglumine) was injected as preload. A second bolus of contrast agent (0.2 mMol/kg) was injected after 85 s of baseline scanning. A post-contrast axial T_1-weighted fast spin echo that was acquired following the DSC-MRI scan.

Tumor regions of interest were defined by subtracting a normalized T_1-weighted image from the normalized post-contrast T_1 image to generate a T_1 subtraction map. A semi-automated thresholding technique for segmenting tumors was used followed by manual adjustment of the contour[68].

Coefficient of variation, standard deviation divided by the mean (σ/μ), was computed between the two pre-treatment time points within the tumor lesion. Tumors whose volumes grew more than 40% were eliminated from this analysis. A non-parametric Friedman test was performed among the three different leakage models using the coefficient of variation values generated per patient.

In **Fig. 3.6**, we compare, the median rCBV between the two pre-treatment time points of recurrent GBMs using the three leakage models. Overall, the non-parametric Friedman test was statistically significant ($p = 0.0064$), with the most significant finding occurring between the uncorrected rCBV and the *Bidir* rCBV ($p = 0.0046$). Comparisons between the other pairings were not found to be statistically significant after multiple comparisons correction.

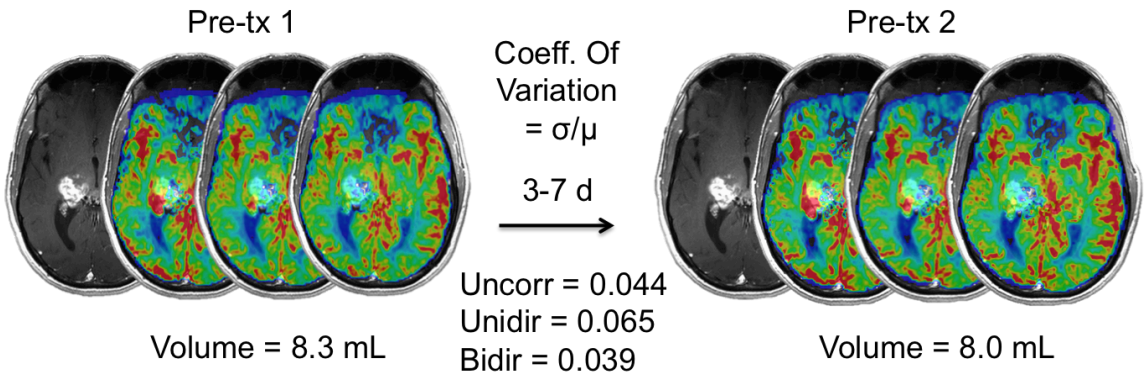

Fig. 3.5. Patients had two pre-treatment scans acquired a few days apart. The coefficient of variation (CV) was taken between the median rCBV within the tumor from the two scans. The lower the CV, the closer the rCBV was between the two scans. From left to right, the rCBV maps correspond to the uncorrected, *Unidir*, and *Bidir* leakage corrections. The *Bidir* had the lowest coefficient of variation, followed by the uncorrected and *Unidir*, respectively.

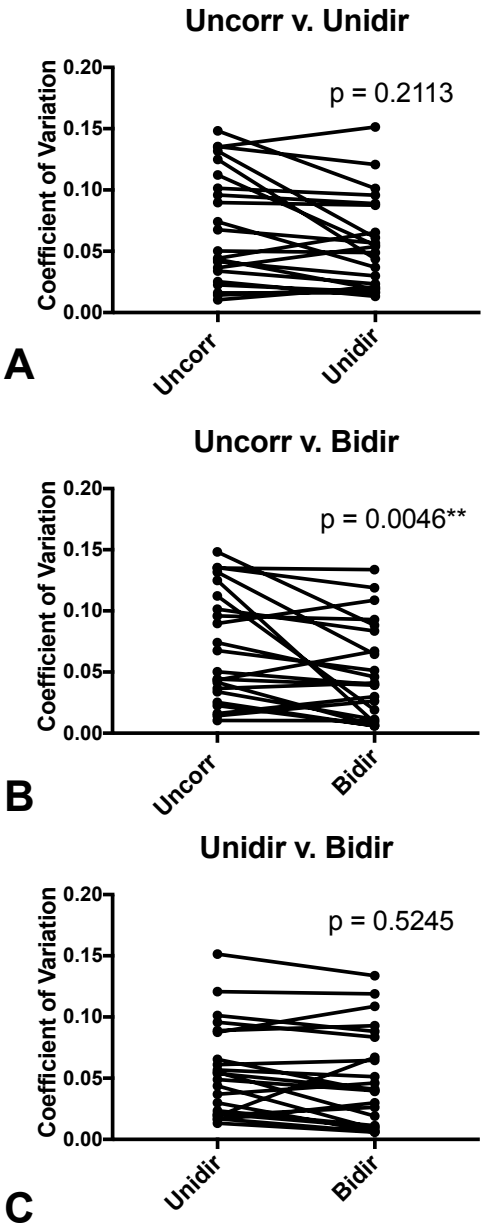

Fig 3.6. Reproducibility comparisons of the coefficient of variation between the leakage correction models: A) uncorrected versus *Unidir-model*, B) uncorrected versus *Bidir-model*, and C) *Unidir-model* and *Bidir-model*. The *Unidir-model* was not found to have superior performance than the uncorrected rCBV (p = 0.2113), whereas the *Bidir*-model did (p = 0.0046).

iv. Verifying Improvement in Estimated rCBV via Intra-scan Reproducibility

Instead of examining the reproducibility of rCBV between scans, we study the rCBV reproducibility between echoes of the same multi-echo sequence. The technique by which we can simultaneously acquire two gradient echo DSC-MRI scans is introduced in **Fig. 3.7**. In brief, this multi-echo DSC-MRI sequence allows us to simultaneously acquire two different gradient echo DSC-MRI scans (echo 1 and echo 2) that are different impacted by leakage (**Figure 3.8**). More specifically, the echo with a TE = 14 ms has a much more T_1-weighted leakage artifact than the echo with a TE = 34 ms in every voxel. Given that the curves acquired were from the same patient at the same time, we would expect the rCBV to be virtually identical. In this study, we hypothesize that the bidirectional leakage correction will produce more similar rCBV between the two different echo times than the unidirectional or uncorrected rCBV.

All thirty-eight patients with varying grades (seven grade II, ten grade III, and twenty-one grade IV) provided informed consent to be included in this research study. Perfusion-weighted imaging data were acquired on 3.0T MRI systems (Siemens) using a quadruple echo spin-and-gradient echo sequence.

Standard anatomic imaging consisted of an axial T_1-weighted fast spin-echo and a T_2-weighted fluid attenuated inversion recovery (FLAIR). Perfusion-weighted imaging was obtained via a quadruple-echo combined spin-and-gradient echo echoplanar sequence, consisting of two gradient echoes, an asymmetric spin echo, and a spin echo. Flip angle was 90°, echo times (TE) were 14.1/34.0 ms, repetition time (TR) was 2 s, with matrix size 128 x 128, slice thickness 5 mm with no interslice gap, and total voxel size 1.875 x 1.875 x 5 mm. A total of 120 time points were acquired. Prior to the start of

DSC-MR imaging, a quarter dose of contrast agent (gadopentate dimeglumine) was injected as preload. A second bolus of contrast agent (three-quarter dose) was injected after 30 s of baseline scanning. The total injection dosage was 0.1 mM/kg. A post-contrast axial T1-weighted fast spin echo that was acquired following the DSC-MRI scan.

Tumor ROIs were defined by abnormal hyperintensity on T_1-weighted post-contrast images and T_2-weighted FLAIR images using semi-automated segmentation techniques, followed by manual inspection and adjustment of the resulting contour as described previously[66]. All DSC-MRI studies completely covered the spatial extent of contrast enhancing tumor. DSC-MRI images were motion-corrected on the scanner and processed via in-house custom scripts in MATLAB (Natick, MA).

Relative cerebral blood volumes were calculated using the *Unidir-model* and *Bidir-model* for the two gradient echoes using the whole brain average from the second echo because the first echo yielded negative values, a physical impossibility. Coefficient of variation (CV), standard deviation divided by the mean (σ/μ), was computed for each voxel between the two echoes. The smaller CV between the *Unidir-model* and *Bidir-model* was considered to be superior, and the percentage of voxels in which the *Bidir-model* outperformed the *Unidir-model* was recorded in each T_1-weighted post-contrast and T_2-weighted lesion.

Fig. 3.9 shows an example plot of two curves from the same voxel. The higher-valued curve comes from the second echo (TE = 34.0 ms) and the lower-valued curve comes from the first echo. **Fig. 3.10** demonstrates the parametric relative cerebral blood volume maps for the uncorrected, *Unidir-model*, and *Bidir-model*. The uncorrected

rCBV yields negative values within tumor for both echoes of this grade IV tumor, a physical impossibility. Echo 1 even yields negative values for much of the normal appearing white matter; thus, normalization with the white matter causes the rCBV values to be artificially high. The *Unidir-model* yields negative rCBV values for the tumor in echo 1, but not in echo 2. Finally, the *Bidir-model* yielded positive values for rCBV. The *Bidir-model* outperformed the *Unidir-model* in 75.4% of the voxels within the T_1-weighted post-contrast lesion (**Fig. 3.10**). For all tumors, the percentage of voxels within the T_1-weighted and T_2-weighted lesions where the bidirectional had a lower CV than the unidirectional was calculated for each tumor and is plotted in **Fig. 3.11.**

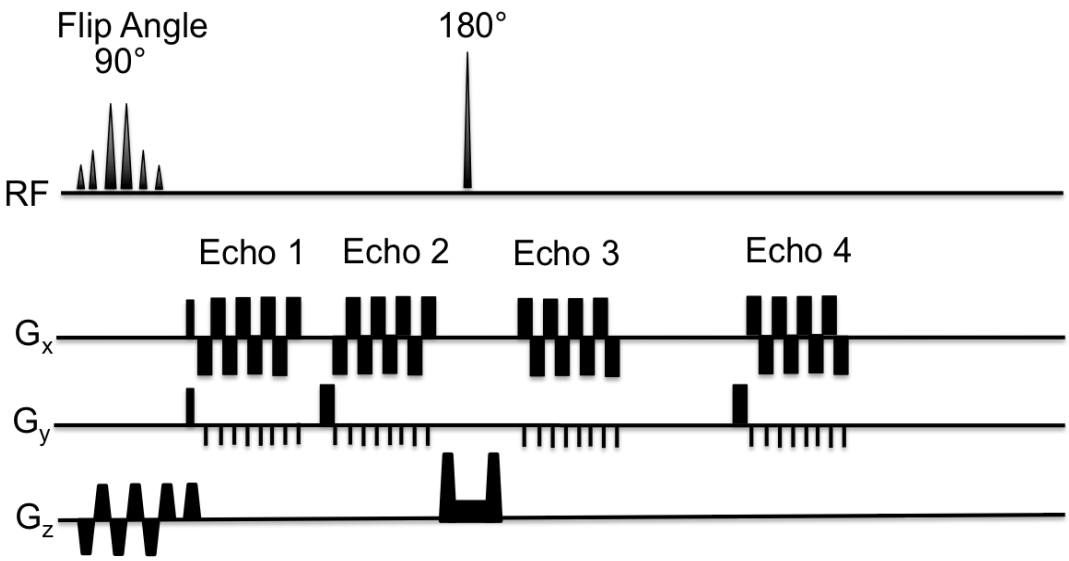

Fig. 3.8. Example of the DSC-MRI curves from two echoes in the same voxel. The 14 ms echo has more T_1-weighting due to contrast agent leakage than the 34 ms echo. In theory, the rCBV derived from both echoes should be the same since the echoes are from the same scan acquisition.

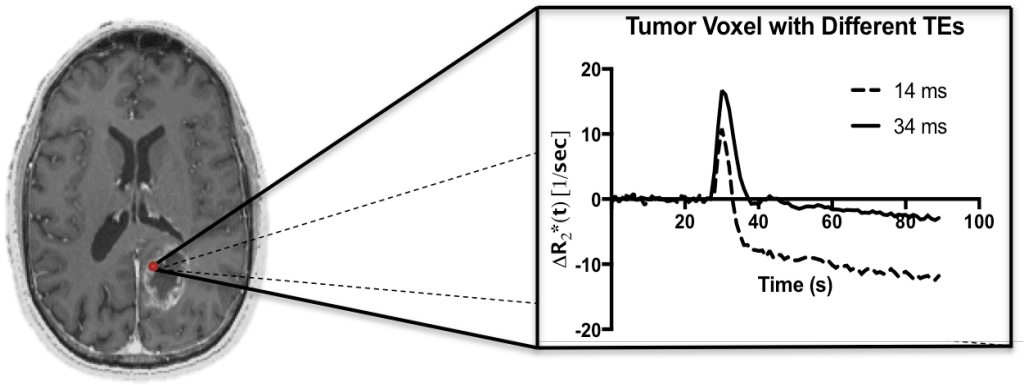

Fig. 3.7. Quadruple echo, spin-and-gradient echo pulse sequence diagram. Modified from a spin echo pulse sequence, this sequence features an excitation pulse, a refocusing pulse, and four EPI trains. The echo times (TE) used are 14.1, 34.0, 58.0, and 92.4 ms, respectively, and the repetition time (TR) was 2.0s.

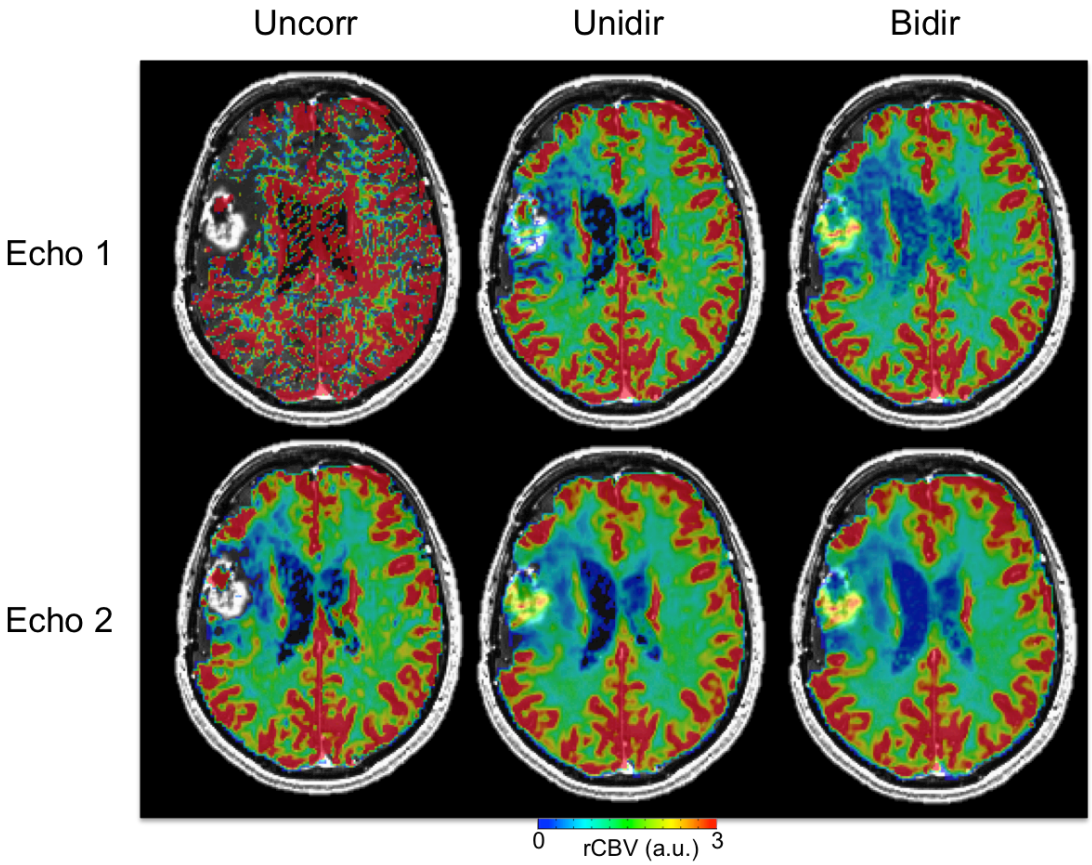

Fig. 3.9. Parametric rCBV maps from the two different echoes of a multiecho sequence, normalized to the normal appearing white matter. (*Left Column)* The uncorrected maps have negative rCBV within tumor for both echoes. (*Center Column)* The unidirectional rCBV parametric map still contains many negative rCBV values within tumor (white voxels) for echo 1, as compared to the rCBV in echo 2. (*Right Column)* The rCBV using the bidirectional method are positive and appear to be much closer in value to each other as compared to the *Unidir* rCBV.

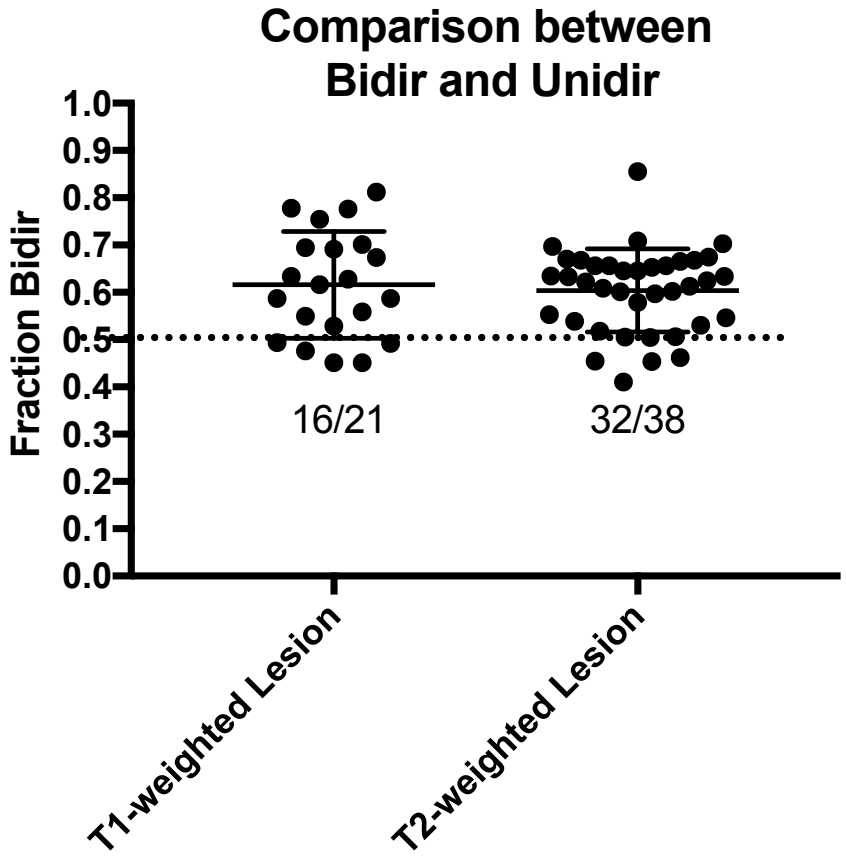

Fig. 3.10. Comparison of coefficient of variation (CV) between *Bidir* and *Unidir* between two echoes from the same sequence within T_1-weighted and T_2-weighted lesions. Points above 0.5 indicate that in greater than 50% of the voxels within the tumor lesion, the *Bidir* had a lower CV between the two echoes than the *Unidir*. Among the 21 tumors that had post-contrast enhancing T_1-weighted lesions, the *Bidir* model performed better in 16 (>50% of the voxels had smaller CV). Among all 38 tumors, contoured using the T_2-weighted image, 32 favored the *Bidir* model.

v. Discussion

By incorporating the Tofts model into the single-echo DSC-MRI relaxation rate equation, we developed an improved post-processing leakage correction method accounting for bidirectional contrast agent transport between the intravascular and interstitial spaces that commonly occurs in angiogenic high-grade gliomas. Our results demonstrate the importance of considering the interstitial washout term, even when modeling the relaxation rate changes during short image acquisitions. For instance, in the simulation, we observed differences between the *Bidir-model* and *Unidir-model* model fits to relaxation rate data in high-grade gliomas in the first-pass curve (as early as 10-20 seconds after injection). Furthermore, by including a washout term, the *Bidir-model* alleviates the error in relaxation rate estimates for arteries and normal brain introduced by conventional models constrained to increasing contrast agent concentration over time in all tissues.

Our results suggest that the conventional *Unidir-model* undercorrects rCBV, with insufficiently increased and decreased rCBV compared to uncorrected rCBV in T_1-dominant and T_2*-dominant leakage scenarios, respectively. Furthermore, since the low flip angle DSC-MRI protocol was largely T_2*-dominant, and the largest discrepancies between *Bidir-model* and *Unidir-model* estimates of rCBV existed for T_2* dominant voxels, our results suggest that the *Bidir-model* may be particularly advantageous over the *Unidir-model* for correcting the residual T_2* effects frequently encountered in dual-echo gradient-echo acquisitions.

Results also suggest that the comparative undercorrection of rCBV by the *Unidir-model*, also made the *Unidir-model's* performance weaker than that of the *Bidir-model*

with respect to the rCBV reproducibility experiments. In the interscan replication study, the *Unidir-model* was not significantly better than the uncorrected rCBV while the bidirectional was. Furthermore, the *Unidir-model* was not able to adequately correct for the heavily T_1-weighted echo of the intrascan experiment, corroborating the simulation findings that the *Unidir-model* was influenced more heavily by scan acquisition protocol than the *Bidir-model*. On the other hand, the *Bidir-model* outperformed the uncorrected rCBV in the interscan study, and significantly outperformed the *Unidir-model* when comparing rCBV similarity within the voxels of the intrascan study.

Overall, it is important to note that this algorithm can be performed without a substantial increase in post-processing computation time over the unidirectional model; therefore, the bidirectional model can simply replace the previous model in routine clinical work as well as for evaluating tumor grade, distinguishing pseudoprogression from true progression, and evaluating treatment response.

Several post-processing leakage correction techniques have previously been proposed.[41, 69] The method by Weisskoff and Boxerman[29-31] (*Unidir-model*), which linearly fits measured $\Delta\hat{R}_2^*(t)$ to two constant functions derived from average relaxation rate in non-enhancing tissue, can be applied quickly to conventional single-echo (spin echo or gradient echo) acquisitions and contrast agent injection schemes. Improved correlation of rCBV with glioma grade compared to uncorrected rCBV[31] provides anecdotal evidence of the benefit of the *Unidir-model*, which has also been shown to improve correlation of gadolinium-based rCBV measures to those obtained using intravascular MION agent as a gold standard.[49]

Bjornerud *et al.*[52] proposed a method that reduces the sensitivity of rCBV correction to mean transit time that could be combined with the *Bidir-model* scheme. Interestingly, Schmiedeskamp *et al.*[41] employed a multi-echo gradient echo and spin echo acquisition scheme to correct for T_1 and T_2* leakage using a backflow term; however, results were highly dependent on literature values for $r_{2,E}^*$ and $r_{2,P}^*$, the T_2* relaxation effects of gadolinium in the extravascular space and plasma, respectively, which can vary quite substantially depending on the literature source. Additionally, Quarles *et al.*[25] suggested these values could vary from tumor to tumor, depending on physiologic factors such as interstitial, vascular, and cell volume fractions and vessel and cell size. An advantage of the *Bidir-model* correction method is the lack of assumptions for $r_{2,E}^*$ and $r_{2,P}^*$. It is also important to note that all of these leakage correction algorithms aim to isolate the relaxation rate due to the residual intravascular contrast agent by eliminating the T_1- and T_2*-related contributions to relaxation rate from the extravasated contrast agent. They do not "add back" T_2* relaxation that would have been realized had the extravasated contrast agent not left the plasma space, and so "corrected rCBV" may still differ from that computed for a tumor with no vascular permeability, all other parameters (including true blood volume) being equal.

One potential limitation to this study is its retrospective design, which may have yielded a selection bias in the sample. Specifically, all patients were chosen because they failed standard therapy. Another potential limitation is the lack of correlation with a gold standard, such as histology or with CBV estimates using intravascular agents such as iron oxide contrast agents. Moreover, AIC is a unitless quantity that can compare relative goodness of fit between models, but does not have a direct test to determine if one model

is significantly better than the other. For interscan reproducibility, one limitation is that the true cerebral blood volume may have changed in the few days between the scans, though care was taken to eliminate the tumors that grew substantially. For intrascan reproducibility, the whole brain average was derived from only the second echo since the first echo had negative blood volume, even in the white matter, owing to its extremely T_1-weighted nature.

In summary, the results suggest that the *Bidir-model* more accurately corrects for the T_1 or T_2* enhancement arising from contrast agent extravasation due to blood-brain barrier disruption in high-grade gliomas by incorporating interstitial washout rates into the DSC-MRI relaxation rate model. This, in turn, allows for better rCBV reproducibility between scans and between echoes of the same scan. To this end, the *Bidir-model* may potentially improve patient diagnosis and evaluation of treatment response by more accurately estimating rCBV in DSC-MRI.

Chapter IV. Clinical Validation of Improved rCBV Estimation in Human Gliomas

Preface

Section iv of this chapter, "Survival Analysis in Bevacizumab-Treated Patients" was based on the following publication:

Leu K, Boxerman JL, Lai A, Nghiemphu PL, Pope WB, Cloughesy TF, Ellingson BM. Bidirectional Contrast Agent Leakage Correction of DSC-MRI Improves Cerebral Blood Volume Estimation and Survival Prediction in Recurrent Glioblastoma Treated with Bevacizumab. *J Magn Reson Imaging*. 2016; 44:1229-1237.

i. Introduction

In this chapter, we extend the bidirectional and unidirectional leakage correction algorithm comparison to correlation with clinical biomarkers. More specifically, we correlate tumor grade with rCBV, correlate rCBV with a histological assessment of angiogenesis, and perform a survival analysis in patients treated with bevacizumab to examine the potential use of the bidirectional-corrected rCBV as a clinical imaging biomarker in gliomas.

ii. Correlation with Tumor Grade

The unidirectional leakage correction algorithm results have previously been correlated with tumor grade[31], where it was demonstrated that the uncorrected rCBV was not correlated with tumor grade, but the unidirectional was. Owing to the highly T_1-weighted protocol used, i.e. high flip angle, short TE, and short TR, several of the tumors

had a negative rCBV when uncorrected. In this study, we use a T_2*-weighted protocol, i.e. one that has a low flip angle that would theoretically minimize rCBV errors according to the results Chapter II. We examine the performance of the uncorrected, unidirectional, and bidirectional algorithms with respect to tumor grade and hypothesize that accounting for the backflow of contrast agent would yield the highest tumor grade correlation.

In this study, perfusion-weighted imaging was performed on a single-echo gradient echo echoplanar sequence (TR/TE = 1650/25 ms, flip angle = 35°, matrix size = 128 x 128, slice thickness = 5 mm, slice gap = 0 mm, a total of 90 time points were acquired, 1.5 Tesla, Siemens). For DSC-MRI, a total of 0.1 mmol/kg dose of gadopentate dimeglumine (Gd-DTPA; Magnevist, Bayer Schering Pharma, Leverkusen, Germany) was administered, one-quarter for pre-load dosage to reduce T_1-based leakage contamination[70] and the remaining three-quarters for dynamic bolus administration. A two-minute gap was placed between the pre-load dose and the start of baseline imaging of the DSC-MRI. Standard anatomic imaging consisted of a post-contrast T_1-weighted image. All twenty-three patients with varying grades (seven grade II, eight grade III, and eight grade IV) provided informed consent to be included in this study.

As grade II gliomas typically do not enhance, tumor ROIs were defined by abnormal hyperintensity on T_2-weighted post-contrast images using semi-automated segmentation techniques, followed by manual inspection and adjustment of the resulting contour as described previously[66]. All DSC-MRI studies completely covered the spatial extent of contrast enhancing tumor. DSC-MRI images were motion-corrected on the scanner and processed via in-house custom scripts in MATLAB (Natick, MA). A Spearman correlation was performed between rCBV and tumor grades.

In **Fig. 4.1**, we show the box-and-whisker plots for rCBV within each tumor grade. For the uncorrected rCBV, there is very little correlation (r = 0.06, p = 0.7811). Both the *Unidir* and *Bidir* rCBV significantly correlate with tumor grade (r = 0.55/p = 0.0063 and r = 0.56/p = 0.0056, respectively) and have approximately the same level of correlation. All rCBV measures are positive due to the low flip angle used.

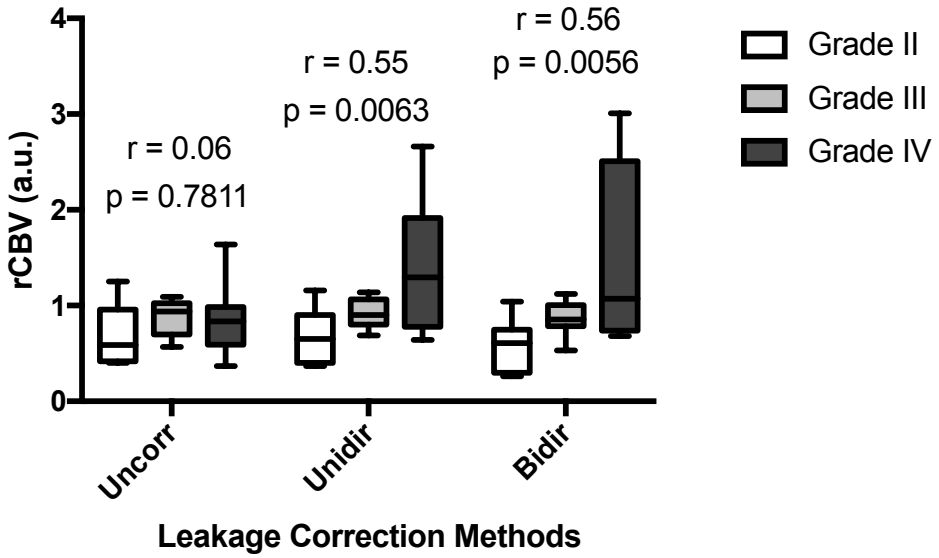

Fig 4.1. Correlation between tumor grade and rCBV for a low-flip angle (35°**)** MRI protocol. Note that for the uncorrected rCBV, the grade III gliomas have, on average, higher rCBV than the grade IV gliomas. Across the spectrum of grade II to grade IV tumors, the *Unidir-model* and *Bidir-model* had similar performances.

iii. Correlation with CD-31 Chalkley Score

Instead of looking at the median rCBV scores from entire tumors, we examine the relationship between rCBV and the CD-31 Chalkley scores from stereotactic biopsy. rCBV has previously been correlated with glucose uptake and tumor angiogenesis in human gliomas[71]. Meanwhile, CD-31 stains endothelial cells and can be marker of angiogenesis in tumors[72]. The Chalkley score, which consists of counting the number of dots on an eyepiece graticule that stain vessels, measures the degree of proliferation of blood vessel endothelium. Even though the CD-31 Chalkley score is not a direct measurement of blood volume, it has been shown to be significantly correlated with vessel luminal area and microvessel number[72], two factors that could comprise blood volume. We therefore hypothesized that rCBV and the CD-31 Chalkley scores would be correlated better in bidirectional rCBV than the unidirectional or uncorrected rCBV.

Stereotactic biopsies were performed in 7 glioma patients (two grade II, four grade III, and one grade IV glioma) with a total of 19 biopsies. Each patient's post-processed perfusion-weighted images were overlaid on the post-contrast T_1-weighted image for localizing of targets. When no contrast-enhancing lesion was present, T_2/FLAIR images were used for target localization. The median of the MRI biomarker was calculated within each target and correlated with the histological score.

To evaluate angiogenesis on histology, the Chalkley method was employed, where an eyepiece graticule with 25 randomly positioned dots are rotated until the maximum number of points hits vessels[73]. The Chalkley count is the number of points that are on stained vessels, where the three highest values are used for each tumor section. Two independent scores were given over each histological section, and the

average of the two was used as the Chalkley score. Given the relatively small number of ROIs, a non-parametric Spearman correlation was performed between the MRI imaging biomarker in each biopsy ROI and its corresponding average Chalkley score so that outliers would not disproportionately affect the correlations.

In **Fig. 4.2**, we show the correlation between CD-31 and the three different rCBV calculations. The area with low rCBV corresponds with a histologic specimen with a small amount of CD-31 staining (Chalkley score: 2.67). In this example, the uncorrected rCBV (1.13) was higher than either the *Unidir* (0.93) or *Bidir* rCBV (0.83). On the other hand, the area of negative uncorrected rCBV (-0.14), but high *Unidir* (2.12) and high *Bidir* (2.15) rCBV corresponds with the endothelial hyperplasia observed on CD-31 (Chalkley score: 18.17). Overall, the uncorrected rCBV had little correlation with CD-31 Chalkley score ($r = 0.11$, $p = 0.62$). Both the *Unidir* and *Bidir* rCBV significantly correlate with tumor grade ($r = 0.47/p = 0.04$ and $r = 0.48/p = 0.03$, respectively) and have approximately the same level of correlation (**Fig 4.3)**.

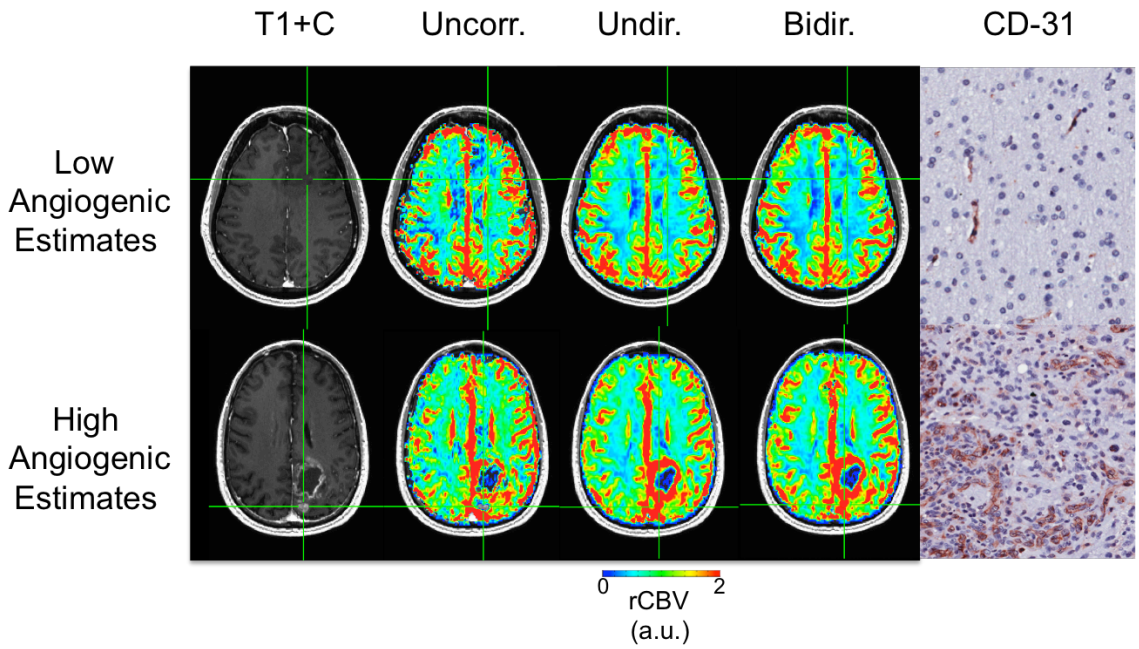

Fig. 4.2. Example of low and high angiogenic estimates on MRI with the three methods of rCBV calculation and the corresponding CD-31 stained histological specimens. (Top) The uncorrected rCBV is 1.13, as compared to lower estimates with the *Unidir* (0.93) and *Bidir* (0.83) estimates, which correspond with a CD-31 Chalkley score of 2.67 . (Bottom) A negative uncorrected rCBV estimate (-0.14), but high *Unidir* rCBV (2.12) and *Bidir* rCBV (2.15) estimates correspond with a high CD-31 Chalkley score (18.17).

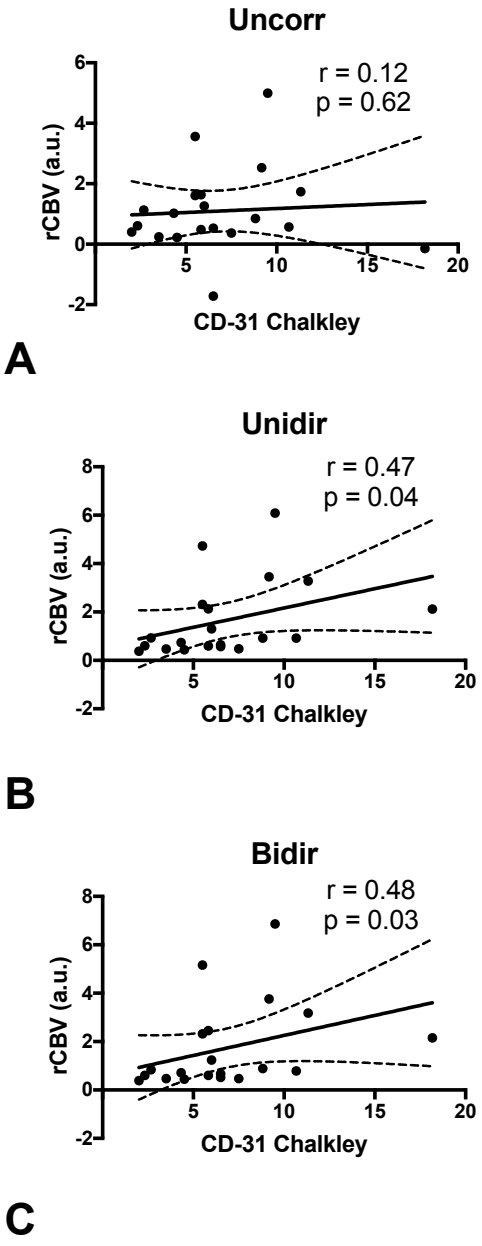

Fig. 4.3. Spearman correlation performed between median rCBV in the region of interest and the CD-31 Chalkley score with trendlines (solid line) and 95% confidence intervals (dotted lines). The uncorrected rCBV did not achieve statistically significant correlation, while the *Unidir* and *Bidir* did. The *Unidir* and *Bidir* had approximately the same performance.

iv. Survival Analysis in Bevacizumab-Treated Patients

As described in Chapter I, the conventional biomarker for measuring the volume of contrast-enhancing lesions was not able to reliably reflect the true tumor burden in the setting of anti-angiogenic drugs. The patients in this cohort were treated with bevacizumab, the only FDA-approved anti-angiogenic therapy for gliomas. Here, we examine if using the change in rCBV after treatment can allow us to stratify bevacizumab-treated glioblastoma patients according to short-term and long-term survival. The imaging biomarker used was rCBV, with the varying leakage corrections and the endpoint used was overall survival (OS). If the rCBV decreased after treatment, we expect that those patients would survive longer than those patients whose rCBV increased after treatment.

More specifically, we aimed to determine the impact of accounting for bidirectional contrast agent exchange on rCBV estimates, as compared to unidirectional model-based rCBV estimates, and whether the association between early post-bevacizumab changes in rCBV compared to pre-treatment baseline and OS significantly differed using the two models. We hypothesized that changes in post-treatment rCBV using the bidirectional leakage correction algorithm will better stratify GBM patients treated with bevacizumab therapy according to overall survival when compared with the unidirectional model.

Patients

All patients provided informed written consent to have their information stored in an IRB-approved neuro-oncology database for use in future investigations. Forty-seven

sequential recurrent GBM (WHO grade IV) patients treated with bevacizumab who had DSC-MRI and outcome data available were retrospectively enrolled (35 men; mean age 57 years, range 28-75). Anatomic and DSC-MRI were acquired within 1 month before (4.1 ± 7.0 days) (mean ± standard deviation) and two months (28.2 ± 11.0 days) after the start of bevacizumab therapy (10 mg/kg IV every 2 weeks).

Magnetic Resonance Imaging

Studies were performed at either 1.5T (Siemens Avanto or Sonata, Erlangen, Germany) or 3T (Siemens Trio, Verio, or Skyra, Erlangen, Germany). Pre-contrast standard anatomical images were acquired, including T_1-weighted, T_2-weighted, and FLAIR images. For DSC-MRI, a total of 0.1 mmol/kg dose of gadopentate dimeglumine (Gd-DTPA; Magnevist, Bayer Schering Pharma, Leverkusen, Germany) was administered, 0.025 mmol/kg for pre-load dosage to mitigate T_1-based leakage contamination[70] and the remaining 0.075 mmol/kg for dynamic bolus administration. A two-minute gap was placed between the pre-load dose and the start of baseline imaging of the DSC-MRI. The range of DSC-MRI acquisition parameters included: TE/TR = 23–41/1250–1400 ms, flip angle = 35°, matrix size = 80x96–128x128, slice thickness = 4–6 mm with an interslice gap of 0–1 mm, number of slices = 6–25, number of baseline acquisitions before contrast agent injection = 10-25, and number of time points = 40-120. Conventional post-contrast T_1-weighted images (T_1+C) were subsequently acquired.

Image Analysis

Tumor ROIs were defined by abnormal hyperintensity on T_1-weighted post-contrast images using semi-automated segmentation techniques, followed by manual inspection and adjustment of the resulting contour as described previously[66]. All DSC-MRI studies completely covered the spatial extent of contrast enhancing tumor. DSC-MRI images were motion-corrected on the scanner and processed via in-house custom scripts in MATLAB (Natick, MA). All simulations and calculations were performed in MATLAB using custom scripts. Uncorrected rCBV was calculated using trapezoidal integration of the original DSC-MRI relaxivity-time curve, $\Delta\hat{R}_2^*(t)$. The whole-brain average relaxivity, derived from the non-enhancing voxels, was used for both the original unidirectional "Boxerman-Weisskoff" model[31] (*Unidir-model*) and the proposed bidirectional exchange model (*Bidir-model*). (Details regarding the *Bidir-model* are described in the "Bidirectional Leakage Correction Theory" section in Chapter I). Linear least squares optimization was used to determine the free parameters for both the *Bidir-model* and the *Unidir-model* algorithms. The rCBV maps were manually registered to the corresponding post-treatment T_1+C images using *tkregister2* (Freesurfer, surfer.nmr.mgh.harvard.edu; Massachusetts General Hospital, Harvard Medical School).

Statistical Analysis

Median rCBV was calculated from segmented tumor at baseline (pre-treatment) and 6-week post-treatment time-points for all patients. All rCBV values were normalized to median rCBV within a circular ROI drawn in the contralateral normal-appearing white matter. Histograms of rCBV were generated via Graphpad Prism 6 (La Jolla, CA) with a bin width of 0.5. We used the absolute value of percentage difference to compare the

leakage correction methods because rCBV tends to increase in the presence of T_1 leakage (between correction methods) and decrease in the presence of T_2* leakage. The absolute difference between the two techniques was calculated as the absolute value of the difference between the two methods divided by the average of the two methods for each patient and each MRI scan.

A multivariate Cox regression model was used to determine whether pre-treatment rCBV, post-treatment rCBV, change in rCBV between pre- and post-treatment time points, age at time of diagnosis, tumor volume, KPS, and MR field strength stratified patients according to OS. Nineteen of the 94 total pre- and post-treatment scans were acquired at 3.0T, and the remaining 75 were acquired at 1.5T, with 10 in the pre-treatment group, and 9 in the post-treatment group. No significant difference, using an unpaired two-tailed t-test, was found between the rCBV values computed using the 3.0T scanner data and the 1.5T scanner data in either the pre-treatment group ($P = 0.63$) or the post-treatment group ($P = 0.14$). Nevertheless, to guard against potential biases with regard to field strength, the pre- and post-treatment field strength as separate covariates.

Results

Fig. 4.4 illustrates a case where the mean tumor rCBV increased following bevacizumab therapy. Individual tumor rCBV values notably increased when employing more accurate leakage correction strategies, exemplified by the progressive rightward shift of the uncorrected, *Unidir-model* and *Bidir-model* rCBV histograms. The uncorrected rCBV map contained a high percentage of negative rCBV values within tumor, averaging -0.09 pre-treatment and 0.29 post-treatment, highlighting the

inaccuracies of uncorrected rCBV estimates. Mean tumor rCBV substantially increased when using the *Unidir-model* (1.72 pre-treatment and 2.33 post-treatment) and increased further when using the *Bidir-model* (2.24 pre-treatment and 2.69 post-treatment).

Next, we evaluated whether change in rCBV from baseline to two months measured using the various leakage correction strategies could stratify the 47 recurrent GBM patients treated with bevacizumab according to OS. In particular, we tested whether patients with decreased rCBV following bevacizumab (ΔrCBV < 0) had significantly longer OS compared to patients with increased rCBV (ΔrCBV > 0) after accounting for age, KPS, enhancing tumor size, and MRI field strength. **Fig. 4.5** demonstrates that both uncorrected ΔrCBV and *Unidir-model* ΔrCBV did not stratify patients according to OS (Cox regression; $P = 0.28$ and 0.43, respectively) in a statistically significant manner, whereas the *Bidir-model* ΔrCBV significantly stratified patients into long and short OS based on the change in rCBV ($P = 0.01$). Median OS for the patients whose rCBV estimated with the *Bidir-model* decreased following bevacizumab treatment was 358 days, versus 183 days for those with increasing rCBV. **Table 4.1** illustrates detailed results from the Cox proportional hazards model, including effects of age, change in tumor volume, field strength at the pre-treatment and post-treatment time points, and KPS.

The mean rCBV with the *Bidir-model* had a 13.9±10.3% absolute difference from the *Unidir-model* prior to therapy and a 16.0±17.6% absolute difference in rCBV after treatment over all 47 patients. Over all 94 scan sessions, there was a 14.9±14.4% difference between mean leakage-corrected whole-tumor rCBV computed with the *Bidir-model* and *Unidir-model*. Interestingly, when ΔrCBV was used to characterize

"responders" (ΔrCBV < 0) and "non-responders" (ΔrCBV > 0), 11 of the 47 cases (23%) had different classifications using the two leakage correction algorithms. We then characterize the "responders" and "non-responders" according to whether they had a survival time less than the median (222 days), "short-term survival", or greater than the median, "long-term survival". We considered a "correct classification" to be either a non-responder with short-term survival or a responder with long-term survival. Among the 4 "non-responders" classified by the *Bidir-model*, 3 had "short-term survival" (75%), and among the 7 "responders", 5 had long-term survival (71%). **Fig. 4.6** illustrates one case where the bidirectional leakage correction algorithm demonstrated a decrease in rCBV in a long-term survivor, whereas the unidirectional and uncorrected rCBV did not. Post-treatment rCBV based on the uncorrected model more than doubles from pre-treatment baseline, with equivalent pre- and post-treatment rCBV using the *Unidir-model*. However, the *Bidir-model* yields a substantial decrease from pre-treatment to post-treatment rCBV, which is concordant with the long OS in this patient (1,149 days). The rightward shifts of the rCBV histograms illustrate that differences in mean tumor rCBV are not merely reflecting a large change for few voxels, but rather a global change over the entire tumor.

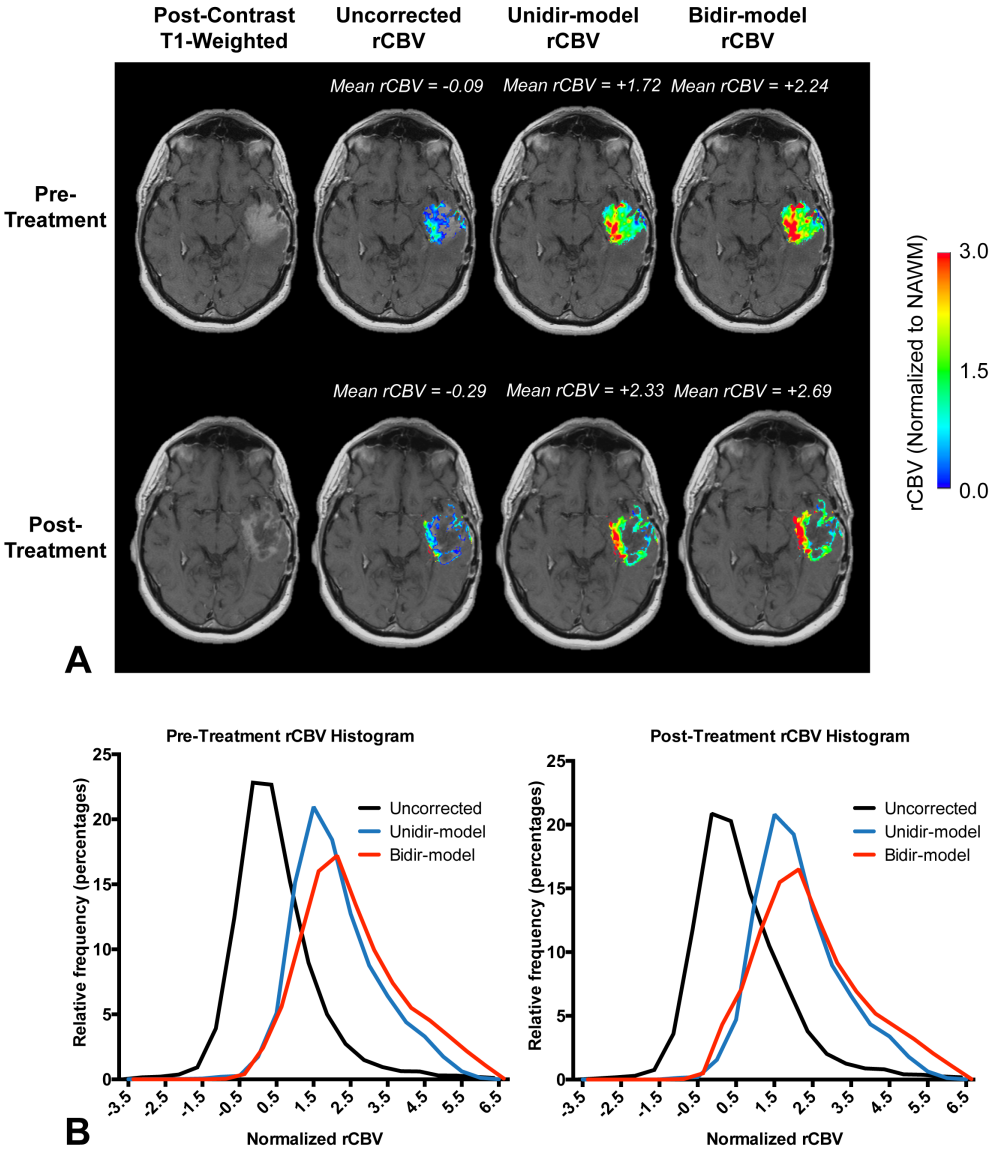

Figure 4.4. (A) Sample rCBV maps for a recurrent GBM, both pre- and post-bevacizumab treatment. Mean pre- and post-treatment tumor rCBV progressively increase when using the uncorrected, *Unidir-model* and *Bidir-model* post-processing strategies. (B) There is a progressive rightward shift of the uncorrected, *Unidir-model* and *Bidir-model* rCBV histograms, demonstrating that the increase in mean rCBV is due to increased rCBV in the entire population of voxels, not just a few, as expected in a T_1-leakage scenario.

Variable	*Hazard Ratio*	*Standard Error*	*p-value*	*95% C.I.*
ΔrCBV > 0 (*Uncorrected*)	0.64	0.41	0.28	0.29, 1.42
Age at recurrence	1.02	0.02	0.25	0.98, 1.06
Change in tumor volume	1.00	0.01	0.98	0.97, 1.03
Field Strength (Pre-tx)	0.65	0.33	0.19	0.34, 1.24
Field Strength (Post-tx)	1.97	0.57	0.24	0.64, 3.02
KPS	0.99	0.02	0.41	0.95, 1.02
ΔrCBV > 0 (*Unidirectional*)	1.33	0.36	0.43	0.66, 2.67
Age at recurrence	1.02	0.02	0.28	0.98, 1.06
Change in tumor volume	1.00	0.01	0.79	0.98, 1.03
Field Strength (Pre-tx)	0.68	0.34	0.25	0.35, 1.31
Field Strength (Post-tx)	1.66	0.36	0.16	0.82, 3.34
KPS	0.99	0.02	0.55	0.95, 1.03
ΔrCBV > 0 (*Bidirectional*)	3.12	0.42	**0.01***	1.37, 7.10
Age at recurrence	1.01	0.02	0.65	0.97, 1.05
Change in tumor volume	0.99	0.01	0.64	0.97, 1.02
Field Strength (Pre-tx)	0.67	0.34	0.36	0.35, 1.30
Field Strength (Post-tx)	2.43	0.38	0.02	1.14, 5.18
KPS	0.98	0.02	0.36	0.95, 1.02

Table 4.1. Cox regression model results with the following variables: ΔrCBV > 0 (binary classification), age at recurrence, change in tumor volume, field strength (pre-tx), field strength (post-tx), and KPS.

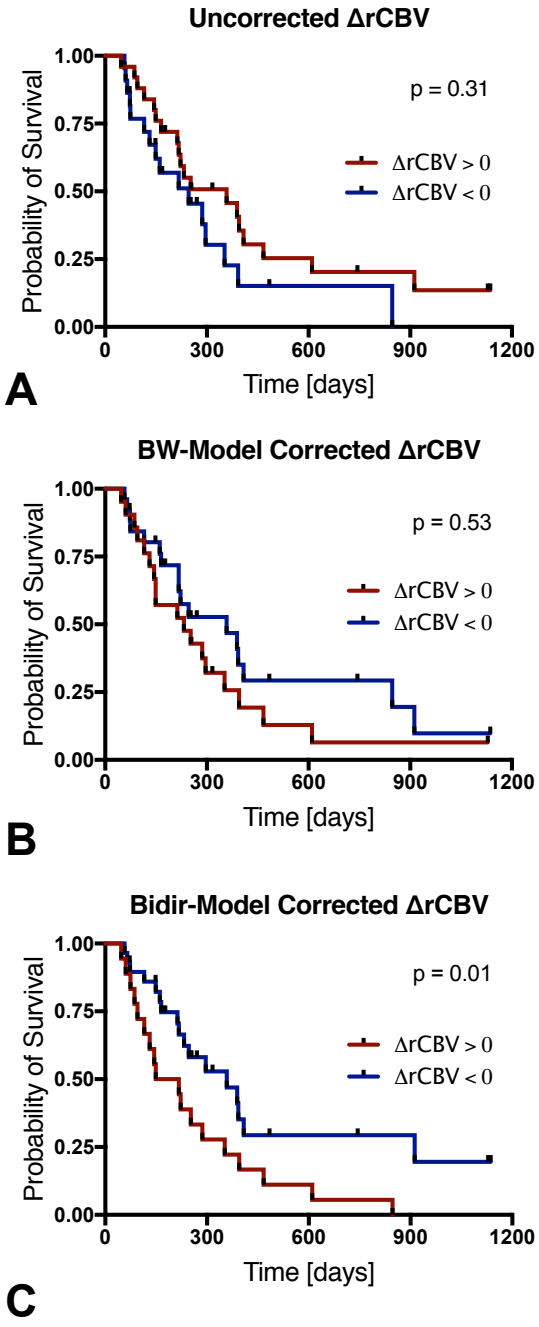

Fig. 4.5. Kaplan-Meier survival plots for ΔrCBV, with patients stratified according to whether rCBV increased or decreased using (A) uncorrected rCBV, (B) *Unidir-model* rCBV, and (C) *Bidir-model* rCBV.

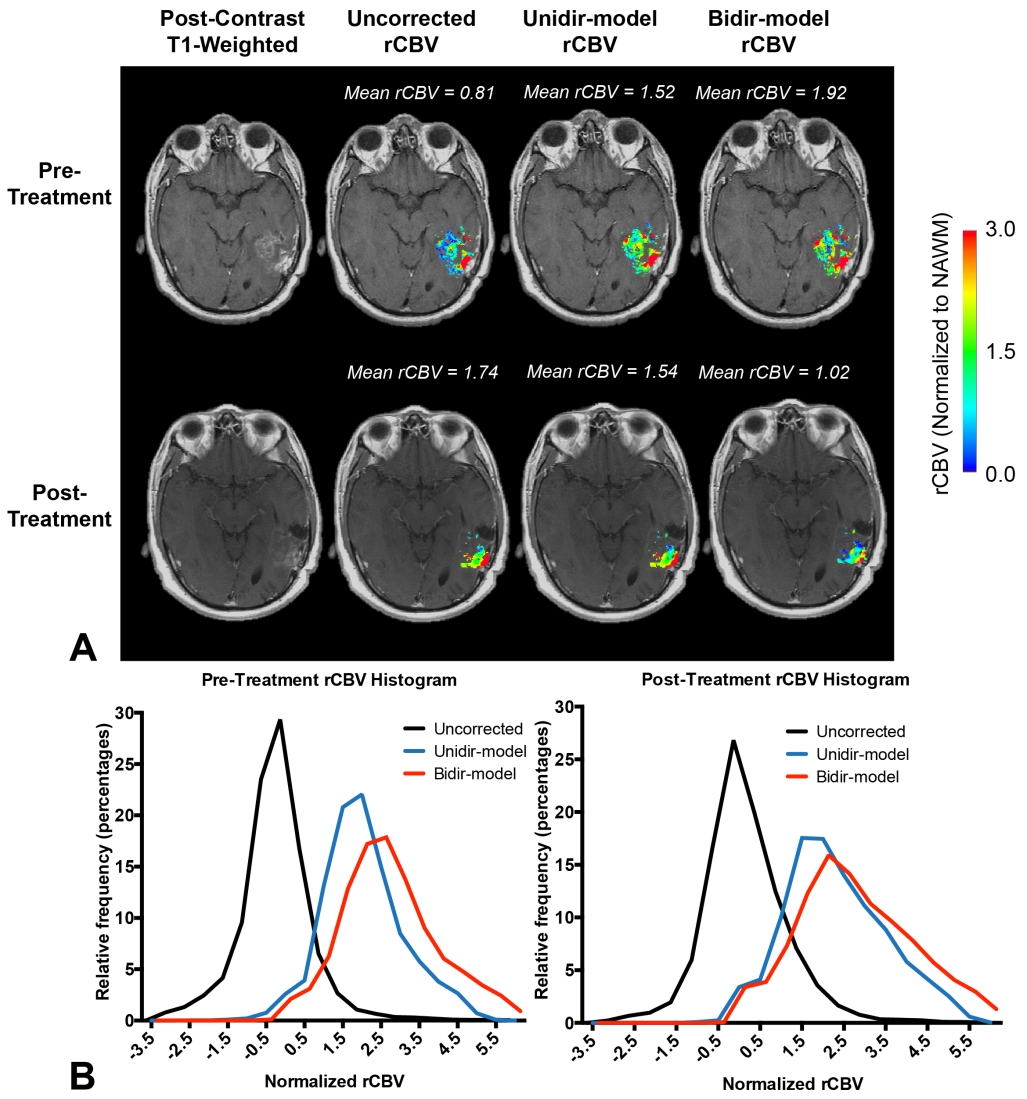

Fig. 4.6. (A) Comparison of rCBV maps of recurrent GBM based on uncorrected, *Unidir-model*, and *Bidir-model* methodologies in a patient with long-term survival (1,149 days). Whereas the *Bidir-model* demonstrates a substantial decrease in rCBV post-treatment, in accordance with favorable OS, the uncorrected and *Unidir-model* estimates of increasing or stable rCBV misclassify the patient as having poor prognosis. (B) There is a leftward shift for the *Bidir-model* histogram, but rightward shifts for the uncorrected and *Unidir-model*.

v. Discussion

Results from the studies in this section support the hypothesis that DSC-MRI leakage correction accounting for bidirectional contrast agent exchange may yield significantly different estimates of tumor rCBV compared with the standard "Boxerman-Weisskoff" unidirectional model and the uncorrected model. Furthermore, in clinical settings, the bidirectional will perform at least as well as the unidirectional in the various clinical applications presented. With respect to the tumor grade and CD-31 Chalkley score correlations, the performance between the unidirectional and bidirectional leakage corrections were similar. As several of the tumors in these cohorts had no contrast-enhancing lesion and thus no noticeable vascular permeability, it would be expected that the rCBV differences in the non-contrast enhancing tumors would be smaller than that observed in contrast-enhancing tumors. On the other hand, in the survival analysis, where only grade IV tumors were studied, we found that early changes in rCBV estimated using the *Bidir-model* better stratify bevacizumab-treated recurrent GBM patients according to OS as compared to estimates using the *Unidir-model*. In accordance with the notion that efficacious therapy works by reducing tumor vascularity, this supports the hypothesis that bidirectional contrast agent exchange using a two-compartment model similar to DCE-MRI more accurately represents the contrast agent pharmacokinetics within the tumor vasculature.

When introduced, the standard *Unidir-model* significantly improved rCBV estimates compared to those made without leakage correction[31]. Addition of a preload or incubation dose to *Unidir-model* post-processing leakage correction further reduced T_1-leakage effects by increasing EES contrast agent concentration prior to dynamic bolus

injection, yielding greater improvement in rCBV measurements obtained without leakage correction[45, 74]. However, the lack of a contrast agent backflow term may lead to an incomplete elimination of the T_1 or T_2* leakage artifact, especially in the presence of a preload because the total contrast agent concentration in the EES is no longer negligible (which ensures the concentration gradient is purely unidirectional), even with short DSC-MRI acquisition times. This is likely a factor contributing to the observed 14.9% difference in rCBV in the survival analysis cohort between the different leakage correction algorithms since we used a preload in the current study. It is important to note that this magnitude of difference in rCBV between the *Bidir-model* and *Unidir-model* may be clinically meaningful and could potentially impact clinical decision-making.

This study has certain notable limitations. First, the correlation with histology was not between two blood volume measurements, but rather a surrogate histological marker of angiogenesis that correlates with luminal area and vessel numbers. Also, with respect to tumor grade, gliomas have a substantial amount of rCBV intragrade variability and are assigned according to a multitude of factors outside of simple blood volume.[75] For the survival study, the DSC-MRI protocols had variable TEs and TRs, with a varying number of slices, slice thicknesses, and field strengths. Although this permitted generalization of our results across a variety of acquisition schemes and MRI platforms, it is unclear whether the same magnitude of differences between the leakage correction algorithms would be maintained in a trial with a single standardized acquisition protocol. Additionally, the time between the MR scans and treatments varied slightly between patients, which may have reduced our ability to assess treatment response. In a clinical trial, these would ideally be more standardized throughout the patient cohort. Given the

relatively small sample size and retrospective nature, which includes biases inherent to such retrospective studies, this investigation was exploratory and larger studies are needed to evaluate the potential impact of the leakage correction algorithms on clinical decision-making. Furthermore, a scanning protocol might be useful to develop in order to provide a more standardized approach for DSC-MRI, even for clinical use in the future.

These studies assume the use of a gadolinium-based contrast agent, which often leaks into the extravascular space when vascular permeability is disrupted. Currently, pure intravascular contrast agents, such as ferumoxytol, are not approved for central nervous system (CNS) imaging, though it is approved for MR angiography. The main advantage of using intravascular contrast agents for perfusion imaging is the lack of extravasation into the extravascular space, eliminating the need for leakage correction algorithms or preload injection [76]. On the other hand, because it is a blood pool agent, the enhancement pattern of biological tissues may differ as compared with gadolinium-based contrast agents, with the possibility of susceptibility artifacts arising [77]. Moreover, there is potentially a requirement of two consecutive days of imaging to obtain relatively intracellular-weighted or interstitial-weighted images, the scans that would be more analogous to the gadolinium-based anatomical scans [78].

The use of a bidirectional leakage correction model changed the estimated rCBV values in grade IV gliomas significantly compared to both the standard unidirectional leakage correction model and rCBV measured without leakage correction, despite relatively short DSC-MRI acquisition times. Smaller changes are seen with tumors that are non-contrast enhancing, leading the tumor grade and CD-31 Chalkley score

correlations to be similar between the *Unidir* and *Bidir* models. However, the large changes in grade IV allow for superior rCBV reproducibility and prediction of survival based on MRI findings.

Chapter V. Conclusion

One of the standards for evaluating glioma therapies has been using MRI to monitor contrast-enhancing tumor volume over time. However, with certain therapies, this has been shown to be insufficient for determining true tumor response. Given that angiogenesis is one of the key features of gliomas, an MRI technique that gives insights into tissue perfusion would aid with the diagnosis and monitoring of treatment in patients, provided that such a biomarker can be shown to accurately reflect the true tumor burden.

To this end, this work addresses some of the challenges presented by contrast agent leakage in DSC-MRI. In Chapter II, we used a simulation method to demonstrate that the bidirectional correction is more robust to scan acquisition protocol than the unidirectional and determined that balancing the T_1- and T_2*-weighted leakage effects helps minimize errors in rCBV. We also present results from an external, independent study in which the bidirectional leakage correction has been shown to be more robust to the scan acquisition protocol than the unidirectional leakage correction, which is important because different institutions employ different DSC-MRI scan acquisition protocols.

In Chapter III, we demonstrate that the bidirectional model outperforms the unidirectional with respect to the modeling of vascular permeability. The bidirectional leakage algorithm has a superior model fit to DSC-MRI data according to the Akaike Information Criterion. The permeability curves generated by the bidirectional model have better correspondence with independently acquired DCE-MRI signal-time curves than the unidirectional model. With respect to rCBV, the unidirectional leakage correction under-corrects the T_1- or T_2*- weighted leakage effects compared to the

bidirectional model by a substantial amount in grade IV tumors. The bidirectional model reduces the intra-patient variability of rCBV between scans and echoes of the same multi-echo sequence for the bidirectional model, yielding more accurate rCBV estimates.

In Chapter IV, we also demonstrate the clinical utility of this technique. The bidirectional leakage correction better stratifies bevacizumab-treated patients according to short-term or long-term survival. More specifically, an increase in rCBV after treatment corresponded with shorter survival, while a decrease after treatment corresponded with longer survival. This potentially foreshadows one use of the bidirectional rCBV measurements clinically as a potential replacement for contrast-enhancing volume when evaluating anti-angiogenic therapies.

In total, we have demonstrated a new leakage correction that unifies the two contrast-based perfusion-weighted MRI modalities. This is an important development as it indicates that no matter whether the weighting is T_1 or T_2/T_{2*}, the bidirectional model/extended Tofts model can be used to compute the traditional perfusion imaging biomarkers. This makes intuitive sense since we are monitoring the same contrast agent behavior, except with different types of MRI contrast. The main difference, though, is that the focus of DSC-MRI is to calculate blood volume, with permeability-surface area serving as the correction factor, while the focus of the DCE-MRI is to calculate permeability-surface area, with blood volume serving as the correction factor.

The goal of this study is to improve relative cerebral blood volume measurements for use in the clinic. While further verification is still needed in larger trials, the difference in rCBV computed from the bidirectional leakage correction before and after treatment could potentially serve as a marker of angiogenesis in glioma treatment. If this

could be used in lieu of the endpoint overall survival (OS) for glioma monitoring, this would make the clinical trial periods potentially shorter for future drug development. Furthermore, the fact that the bidirectional leakage correction is more resistant to differences in DSC-MRI protocols may help improve multi-center trials in the future since, to the best of our knowledge, there is little agreement in the literature as to which DSC-MRI protocol best minimizes errors in rCBV measurements.

Significant hurdles to estimating rCBV accurately in DSC-MRI remain. The most significant challenge is the determination of the arterial input function (AIF) and whole brain average (WBA). Differences between the global AIF/WBA and the local input would cause errors in blood volume calculations, and currently, no standards exist as to how to calculate either the global or local AIFs. Furthermore, a fundamental assumption behind the gradient echo DSC-MRI is that the relaxation rate is linearly proportional to the intravascular concentration of contrast agent. However, the gradient echo signal is a non-linear sum of magnetic field gradients arising from the differences in concentration of contrast agent between compartments. Technically, the non-proportionality between the relaxation-time curve and concentration would be a violation of the indicator dilution theory, where concentration is integrated to calculate blood volume.

Both of these problems could potentially be addressed using the multi-echo spin-and-gradient echo technique described in Chapter III, section iv, "Verifying Improvement in Estimated rCBV via Intra-scan Reproducibility". The spin-and-gradient echo technique allows us to acquire four differently weighted signals. In particular, we expect the blood volume to be the same between the first two echoes, the two gradient echoes, but with a different amount of leakage. Therefore, we can separate the T_1 and T_2*-

weighted effects from both the bolus and the extravasation of contrast agent. Using the last two echoes, we can also extract the T_1 and T_2-weighted effects using similar reasoning. The T_1 and T_2 relaxivity of contrast agent are known from the literature and we therefore can compute the concentration of contrast agent in the plasma and the extravascular space. The former would obviate the need for a global AIF or whole brain average, solving the first problem. Furthermore, the units of the signal-time curve in the plasma would be in terms of concentration of contrast agent. Thus, the integration of this curve would be a direct application of the indicator dilution theory, solving the second problem.

Nevertheless, this work has demonstrated that the bidirectional leakage correction allows for better estimation of relative cerebral blood volume. The bidirectional leakage correction unifies the two perfusion-weighted MRI modalities, implying that the same model can be used to take into account both the bolus of contrast agent in the vasculature and vascular permeability, regardless of the MRI signal contrast. It is also more robust to scan acquisition protocols, which is important for clinical trials in which different institutions may be using different acquisition protocols, and it has given insight into how change in rCBV can potentially be applied to the evaluation of glioma treatment efficacy. In total, our studies in this work have allowed us to gain a deeper understanding of the complexities of DSC-MRI with the objective of routinely using perfusion imaging in neuro-oncology clinics.

References

1. Ostrom QT, Gittleman H, Fulop J, et al. CBTRUS Statistical Report: Primary Brain and Central Nervous System Tumors Diagnosed in the United States in 2008-2012. *Neuro Oncol* 2015;17 Suppl 4:iv1-iv62

2. Stupp R, Mason WP, van den Bent MJ, et al. Radiotherapy plus concomitant and adjuvant temozolomide for glioblastoma. *N Engl J Med* 2005;352:987-996

3. Johnson DR, O'Neill BP. Glioblastoma survival in the United States before and during the temozolomide era. *Journal of neuro-oncology* 2012;107:359-364

4. Venur VA, Peereboom DM, Ahluwalia MS. Current medical treatment of glioblastoma. *Cancer Treat Res* 2015;163:103-115

5. Fischer I, Gagner JP, Law M, et al. Angiogenesis in gliomas: biology and molecular pathophysiology. *Brain Pathol* 2005;15:297-310

6. Onishi M, Ichikawa T, Kurozumi K, et al. Angiogenesis and invasion in glioma. *Brain Tumor Pathol* 2011;28:13-24

7. Goel S, Duda DG, Xu L, et al. Normalization of the vasculature for treatment of cancer and other diseases. *Physiol Rev* 2011;91:1071-1121

8. Leon SP, Folkerth RD, Black PM. Microvessel density is a prognostic indicator for patients with astroglial brain tumors. *Cancer* 1996;77:362-372

9. Wen PY, Macdonald DR, Reardon DA, et al. Updated response assessment criteria for high-grade gliomas: response assessment in neuro-oncology working group. *J Clin Oncol* 2010;28:1963-1972

10. de Wit MC, de Bruin HG, Eijkenboom W, et al. Immediate post-radiotherapy changes in malignant glioma can mimic tumor progression. *Neurology* 2004;63:535-537

11. Hygino da Cruz LC, Jr., Rodriguez I, Domingues RC, et al. Pseudoprogression and pseudoresponse: imaging challenges in the assessment of posttreatment glioma. *AJNR American journal of neuroradiology* 2011;32:1978-1985

12. Brandsma D, Stalpers L, Taal W, et al. Clinical features, mechanisms, and management of pseudoprogression in malignant gliomas. *Lancet Oncol* 2008;9:453-461

13. Batchelor TT, Sorensen AG, di Tomaso E, et al. AZD2171, a pan-VEGF receptor tyrosine kinase inhibitor, normalizes tumor vasculature and alleviates edema in glioblastoma patients. *Cancer Cell* 2007;11:83-95

14. Kamoun WS, Ley CD, Farrar CT, et al. Edema control by cediranib, a vascular endothelial growth factor receptor-targeted kinase inhibitor, prolongs survival despite persistent brain tumor growth in mice. *J Clin Oncol* 2009;27:2542-2552

15. Essig M, Shiroishi MS, Nguyen TB, et al. Perfusion MRI: the five most frequently asked technical questions. *AJR American journal of roentgenology* 2013;200:24-34

16. Meier P, Zierler KL. On the theory of the indicator-dilution method for measurement of blood flow and volume. *J Appl Physiol* 1954;6:731-744

17. Ostergaard L, Weisskoff RM, Chesler DA, et al. High resolution measurement of cerebral blood flow using intravascular tracer bolus passages. Part I: Mathematical approach and statistical analysis. *Magn Reson Med* 1996;36:715-725

18. Axel L. Cerebral blood flow determination by rapid-sequence computed tomography: theoretical analysis. *Radiology* 1980;137:679-686

19. Mouridsen K, Christensen S, Gyldensted L, et al. Automatic selection of arterial input function using cluster analysis. *Magnetic resonance in medicine* 2006;55:524-531

20. Bleeker EJ, Webb AG, van Walderveen MA, et al. Evaluation of signal formation in local arterial input function measurements of dynamic susceptibility contrast MRI. *Magnetic resonance in medicine* 2012;67:1324-1331

21. Bleeker EJ, van Osch MJ, Connelly A, et al. New criterion to aid manual and automatic selection of the arterial input function in dynamic susceptibility contrast MRI. *Magnetic resonance in medicine* 2011;65:448-456

22. van Osch MJ, Vonken EJ, Viergever MA, et al. Measuring the arterial input function with gradient echo sequences. *Magn Reson Med* 2003;49:1067-1076

23. Calamante F. Arterial input function in perfusion MRI: a comprehensive review. *Prog Nucl Magn Reson Spectrosc* 2013;74:1-32

24. Rosen BR, Belliveau JW, Vevea JM, et al. Perfusion imaging with NMR contrast agents. *Magn Reson Med* 1990;14:249-265

25. Quarles CC, Gochberg DF, Gore JC, et al. A theoretical framework to model DSC-MRI data acquired in the presence of contrast agent extravasation. *Phys Med Biol* 2009;54:5749-5766

26. Hu LS, Baxter LC, Pinnaduwage DS, et al. Optimized preload leakage-correction methods to improve the diagnostic accuracy of dynamic susceptibility-weighted contrast-enhanced perfusion MR imaging in posttreatment gliomas. *AJNR American journal of neuroradiology* 2010;31:40-48

27. Knopp EA, Cha S, Johnson G, et al. Glial neoplasms: dynamic contrast-enhanced T2*-weighted MR imaging. *Radiology* 1999;211:791-798

28. Cha S, Knopp EA, Johnson G, et al. Dynamic contrast-enhanced T2-weighted MR imaging of recurrent malignant gliomas treated with thalidomide and carboplatin. *AJNR American journal of neuroradiology* 2000;21:881-890

29. Aronen HJ, Gazit IE, Louis DN, et al. Cerebral blood volume maps of gliomas: comparison with tumor grade and histologic findings. *Radiology* 1994;191:41-51

30. Donahue KM, Krouwer HG, Rand SD, et al. Utility of simultaneously acquired gradient-echo and spin-echo cerebral blood volume and morphology maps in brain tumor patients. *Magn Reson Med* 2000;43:845-853

31. Boxerman JL, Schmainda KM, Weisskoff RM. Relative cerebral blood volume maps corrected for contrast agent extravasation significantly correlate with glioma tumor grade, whereas uncorrected maps do not. *AJNR American journal of neuroradiology* 2006;27:859-867

32. Cha S, Knopp EA, Johnson G, et al. Intracranial mass lesions: dynamic contrast-enhanced susceptibility-weighted echo-planar perfusion MR imaging. *Radiology* 2002;223:11-29

33. Law M, Yang S, Wang H, et al. Glioma grading: sensitivity, specificity, and predictive values of perfusion MR imaging and proton MR spectroscopic imaging compared with conventional MR imaging. *AJNR Am J Neuroradiol* 2003;24:1989-1998

34. Law M, Oh S, Babb JS, et al. Low-grade gliomas: dynamic susceptibility-weighted contrast-enhanced perfusion MR imaging--prediction of patient clinical response. *Radiology* 2006;238:658-667

35. Danchaivijitr N, Waldman AD, Tozer DJ, et al. Low-grade gliomas: do changes in rCBV measurements at longitudinal perfusion-weighted MR imaging predict malignant transformation? *Radiology* 2008;247:170-178

36. Boxerman JL, Ellingson BM, Jeyapalan S, et al. Longitudinal DSC-MRI for Distinguishing Tumor Recurrence From Pseudoprogression in Patients With a High-grade Glioma. *Am J Clin Oncol* 2014

37. Gahramanov S, Varallyay C, Tyson RM, et al. Diagnosis of pseudoprogression using MRI perfusion in patients with glioblastoma multiforme may predict improved survival. *CNS Oncol* 2014;3:389-400

38. Schmainda KM, Zhang Z, Prah M, et al. Dynamic susceptibility contrast MRI measures of relative cerebral blood volume as a prognostic marker for overall survival in

recurrent glioblastoma: results from the ACRIN 6677/RTOG 0625 multicenter trial. *Neuro Oncol* 2015

39. Leu K, Enzmann, D.R., Woodworth, D.C., Harris, R.J., Tran, A.N., Lai, A., Nghiemphu, P.L., Pope, W.B., Cloughesy, T.F., and Ellingson, B.M. Hypervascular tumor volume estimated by comparison to a large-scale cerebral blood volume radiographic atlas predicts survival in recurrent glioblastoma treated with bevacizumab. *Cancer Imaging* 2014;14:31

40. LaViolette PS, Cohen AD, Prah MA, et al. Vascular change measured with independent component analysis of dynamic susceptibility contrast MRI predicts bevacizumab response in high-grade glioma. *Neuro Oncol* 2013;15:442-450

41. Schmiedeskamp H, Andre JB, Straka M, et al. Simultaneous perfusion and permeability measurements using combined spin- and gradient-echo MRI. *J Cereb Blood Flow Metab* 2013;33:732-743

42. Tofts PS, Kermode AG. Measurement of the blood-brain barrier permeability and leakage space using dynamic MR imaging. 1. Fundamental concepts. *Magn Reson Med* 1991;17:357-367

43. Murase K. Efficient method for calculating kinetic parameters using T-1-weighted dynamic contrast-enhanced magnetic resonance imaging. *Magnet Reson Med* 2004;51:858-862

44. Sourbron SP, Buckley DL. On the scope and interpretation of the Tofts models for DCE-MRI. *Magnetic resonance in medicine* 2011;66:735-745

45. Paulson ES, Schmainda KM. Comparison of dynamic susceptibility-weighted contrast-enhanced MR methods: recommendations for measuring relative cerebral blood volume in brain tumors. *Radiology* 2008;249:601-613

46. Vonken EJ, van Osch MJ, Bakker CJ, et al. Measurement of cerebral perfusion with dual-echo multi-slice quantitative dynamic susceptibility contrast MRI. *J Magn Reson Imaging* 1999;10:109-117

47. Schmiedeskamp H, Straka M, Newbould RD, et al. Combined spin- and gradient-echo perfusion-weighted imaging. *Magn Reson Med* 2012;68:30-40

48. Skinner JT, Robison RK, Elder CP, et al. Evaluation of a multiple spin- and gradient-echo (SAGE) EPI acquisition with SENSE acceleration: applications for perfusion imaging in and outside the brain. *Magnetic resonance imaging* 2014;32:1171-1180

49. Boxerman JL, Prah DE, Paulson ES, et al. The Role of preload and leakage correction in gadolinium-based cerebral blood volume estimation determined by

comparison with MION as a criterion standard. *AJNR Am J Neuroradiol* 2012;33:1081-1087

50. Leu K, Boxerman JL, Cloughesy TF, et al. Improved Leakage Correction for Single-Echo Dynamic Susceptibility Contrast Perfusion MRI Estimates of Relative Cerebral Blood Volume in High-Grade Gliomas by Accounting for Bidirectional Contrast Agent Exchange. *AJNR Am J Neuroradiol* 2016; 37:1440-6

51. Leu K, Boxerman JL, Lai A, et al. Bidirectional Contrast agent leakage correction of dynamic susceptibility contrast (DSC)-MRI improves cerebral blood volume estimation and survival prediction in recurrent glioblastoma treated with bevacizumab. *J Magn Reson Imaging* 2016; 44:1229-1237

52. Bjornerud A, Sorensen AG, Mouridsen K, et al. T1- and T2*-dominant extravasation correction in DSC-MRI: part I--theoretical considerations and implications for assessment of tumor hemodynamic properties. *J Cereb Blood Flow Metab* 2011;31:2041-2053

53. Simpson NE, He Z, Evelhoch JL. Deuterium NMR tissue perfusion measurements using the tracer uptake approach: I. Optimization of methods. *Magn Reson Med* 1999;42:42-52

54. Pintaske J, Martirosian P, Graf H, et al. Relaxivity of Gadopentetate Dimeglumine (Magnevist), Gadobutrol (Gadovist), and Gadobenate Dimeglumine (MultiHance) in human blood plasma at 0.2, 1.5, and 3 Tesla. *Invest Radiol* 2006;41:213-221

55. Kjolby BF, Ostergaard L, Kiselev VG. Theoretical model of intravascular paramagnetic tracers effect on tissue relaxation. *Magn Reson Med* 2006;56:187-197

56. Wansapura JP, Holland SK, Dunn RS, et al. NMR relaxation times in the human brain at 3.0 tesla. *J Magn Reson Imaging* 1999;9:531-538

57. Zhang N, Zhang L, Qiu B, et al. Correlation of volume transfer coefficient Ktrans with histopathologic grades of gliomas. *J Magn Reson Imaging* 2012;36:355-363

58. Wu O, Ostergaard L, Koroshetz WJ, et al. Effects of tracer arrival time on flow estimates in MR perfusion-weighted imaging. *Magn Reson Med* 2003;50:856-864

59. Vonken EP, van Osch MJ, Bakker CJ, et al. Simultaneous quantitative cerebral perfusion and Gd-DTPA extravasation measurement with dual-echo dynamic susceptibility contrast MRI. *Magnetic resonance in medicine : official journal of the Society of Magnetic Resonance in Medicine / Society of Magnetic Resonance in Medicine* 2000;43:820-827

60. Welker K, Boxerman J, Kalnin A, et al. ASFNR recommendations for clinical performance of MR dynamic susceptibility contrast perfusion imaging of the brain. *AJNR Am J Neuroradiol* 2015;36:E41-51

61. Englund E, Brun A, Gyorffy-Wagner Z, et al. Relaxation Times in Relation to Grade of Malignancy and Tissue Necrosis in Astrocytic Gliomas. *Magnetic Resonance Imaging* 1986;4:425-429

62. Liu HL, Wu YY, Yang WS, et al. Is Weisskoff model valid for the correction of contrast agent extravasation with combined T1 and T2* effects in dynamic susceptibility contrast MRI? *Medical physics* 2011;38:802-809

63. Kassner A, Annesley DJ, Zhu XP, et al. Abnormalities of the contrast re-circulation phase in cerebral tumors demonstrated using dynamic susceptibility contrast-enhanced imaging: a possible marker of vascular tortuosity. *J Magn Reson Imaging* 2000;11:103-113

64. Pathak AP, Ward BD, Schmainda KM. A novel technique for modeling susceptibility-based contrast mechanisms for arbitrary microvascular geometries: the finite perturber method. *Neuroimage* 2008;40:1130-1143

65. Semmineh NB, Xu J, Boxerman JL, et al. An efficient computational approach to characterize DSC-MRI signals arising from three-dimensional heterogeneous tissue structures. *PLoS One* 2014;9:e84764

66. Ellingson BM, Cloughesy TF, Lai A, et al. Quantitative volumetric analysis of conventional MRI response in recurrent glioblastoma treated with bevacizumab. *Neuro Oncol* 2011;13:401-409

67. Burnham KP, Anderson DR. *Model Selection and Inference*. NY: Springer-Verlag; 1998

68. Ellingson BM, Kim HJ, Woodworth DC, et al. Recurrent glioblastoma treated with bevacizumab: contrast-enhanced T1-weighted subtraction maps improve tumor delineation and aid prediction of survival in a multicenter clinical trial. *Radiology* 2014;271:200-210

69. Quarles CC, Ward BD, Schmainda KM. Improving the reliability of obtaining tumor hemodynamic parameters in the presence of contrast agent extravasation. *Magn Reson Med* 2005;53:1307-1316

70. Schmainda KM, Rand SD, Joseph AM, et al. Characterization of a first-pass gradient-echo spin-echo method to predict brain tumor grade and angiogenesis. *AJNR Am J Neuroradiol* 2004;25:1524-1532

71. Aronen HJ, Pardo FS, Kennedy DN, et al. High microvascular blood volume is associated with high glucose uptake and tumor angiogenesis in human gliomas. *Clinical*

cancer research : an official journal of the American Association for Cancer Research 2000;6:2189-2200

72. Fox SB, Leek RD, Weekes MP, et al. Quantitation and prognostic value of breast cancer angiogenesis: comparison of microvessel density, Chalkley count, and computer image analysis. *J Pathol* 1995;177:275-283

73. Dickinson AJ, Fox SB, Persad RA, et al. Quantification of angiogenesis as an independent predictor of prognosis in invasive bladder carcinomas. *Br J Urol* 1994;74:762-766

74. Ouyang M, Huang H, Shaner NC, et al. Simultaneous visualization of protumorigenic Src and MT1-MMP activities with fluorescence resonance energy transfer. *Cancer Res* 2010;70:2204-2212

75. Law M, Yang S, Babb JS, et al. Comparison of cerebral blood volume and vascular permeability from dynamic susceptibility contrast-enhanced perfusion MR imaging with glioma grade. *AJNR American journal of neuroradiology* 2004;25:746-755

76. Gahramanov S, Muldoon LL, Li X, et al. Improved perfusion MR imaging assessment of intracerebral tumor blood volume and antiangiogenic therapy efficacy in a rat model with ferumoxytol. *Radiology* 2011;261:796-804

77. Fananapazir G, Marin D, Suhocki PV, et al. Vascular artifact mimicking thrombosis on MR imaging using ferumoxytol as a contrast agent in abdominal vascular assessment. *J Vasc Interv Radiol* 2014;25:969-976

78. Farrell BT, Hamilton BE, Dosa E, et al. Using iron oxide nanoparticles to diagnose CNS inflammatory diseases and PCNSL. *Neurology* 2013;81:256-263